Chalcogen Polymers for Completely Solution-Processed Inorganic Photovoltaics

Trevor R Martin

A dissertation
submitted in partial fulfillment of the
requirements for the degree of

Doctor of Philosophy

University of Washington
2017

Reading Committee:
Christine Luscombe, Chair
Hugh Hillhouse
Brandi Cossairt
Fumio Ohuchi

Program Authorized to Offer Degree:
Materials Science and Engineering

University of Washington

Abstract

Chalcogen Polymers for Completely Solution-Processed Inorganic Photovoltaics

Trevor R Martin

Chair of the Supervisory Committee:
Professor Christine Luscombe
Materials Science and Engineering

Chalcopyrite materials such as $CuInS_xSe_{2-x}$ (CISSe), the gallium alloy variant $CuIn_xGa_{1-x}S_ySe_{2-y}$ (CIGSSe), and the earth-abundant kesterite material $Cu_2ZnSnS_xSe_{4-x}$ (CZTSSe) possess a range of properties that are ideally suited for thin-film photovoltaics (PV) applications. Although these materials are beginning to see some commercial success, they are manufactured using complicated and expensive techniques such as high temperature processing, vacuum deposition methods, and vapor-phase reactions. These production methods require an exorbitantly large capital investment to create new manufacturing facilities, which severely hampers the widespread and rapid deployment of these emerging solar energy technologies. This work has focused on developing novel chalcogen polymers to synthesize nanoparticles and produce thin-films for printed photovoltaics applications. This new method provides a pathway towards using chalcogen copolymers to produce these materials via a completely solution-processed, low-temperature fabrication procedure. This technique constitutes one of the first viable means to produce low-bandgap chalcogenides without additional vapor-phase or high-temperature reactions. Therefore, this process can potentially be implemented to rapidly and cheaply manufacture printed chalcopyrite and kesterite photovoltaics.

Acknowledgments

There are many people without whom this thesis would not have been possible. I would like to thank Katherine for all of her support over the years. I would like to also thank my parents Russell and Susie for instilling in me a sense of wonder for the natural world, which has remained with me and has become a driving force behind my desire to become a scientist. I would also like to thank my father for taking the time to show me how to accomplish many hands-on activities, which in the end has given me a solid foundation for laboratory work. I would also like to thank Ed Jaramillo and Amy Wyss for all of their support.

I would also like to thank all of my work colleagues and mentors. Thanks to Professor Luscombe for all of her guidance and for her sincere commitment to education. Thanks to Professor Hillhouse for all of his help during the course of this project. Working with both of these research groups has enabled me to do more impactful work than would otherwise be possible and has pushed me to become a better scientist. I would also like to thank Jeff Elam and Alex Martinson, who helped me tremendously as I began in this field.

Finally, I would like to thank all of the friends, family members, and peers that have helped me in a myriad of ways. This work would not have been possible without all of your contributions.

Table of Contents

List of Figures

List of Schemes

List of Tables

Chapter 1. Introduction and Background

1.1 Photovoltaics as a Clean Energy Technology

A steadily increasing world population, rapid economic growth in developing countries and high levels of economic consumption in industrialized nations have all combined to create an unprecedented level of energy demand and concomitant environmental degradation in the 21st century.[1–4] These issues have accelerated the depletion of fossil fuel resources to the extent that many conventional sources of energy will be gone within the next few decades.[5] Consequently, the need for alternative, environmentally sustainable sources of energy has never been greater. Of all the various renewable energy technologies available to date, solar energy has the largest potential for producing energy by a substantial margin.[6]

Specifically, the potential for using photovoltaic (PV) technologies is particularly enormous as outlined in **Figure 1.1,** which compares the maximum amount of energy that can be potentially produced using various renewable energy technologies in realistic scenarios. The data in Figure 1.1 show that PV technologies have the potential to produce approximately 284,000 Terrawatt hours (TWh) of energy.[6] Therefore, all of the energy needs of the United States could easily be met with the widespread implementation of PV technologies, since we consume roughly

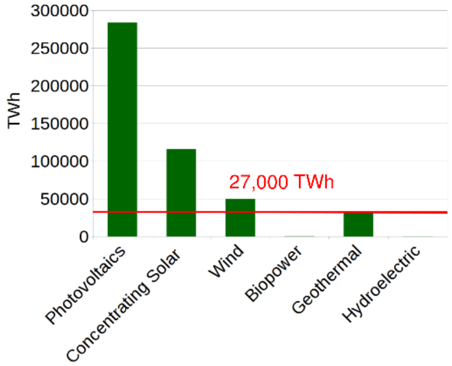

Figure 1.1: Relative amount of energy that can be potentially produced in the United States from various renewable energy technologies annually. Horizontal line represents the current energy use. Produced using data from the National Renewable Energy Laboratory (NREL).[6] Note that the relative potential contributions of some technologies are extremely small, so they cannot be clearly seen in the chart.

27,000 TWh of energy each year.[6] Moreover, the energy needs of the United States could be met with PV while using less land in comparison to other technologies. Although growing steadily, renewable energy production accounts for only a small fraction of overall energy production.[6] The development of cheap, scalable and environmentally friendly PV technologies will accelerate the implementation of PV technology as an energy source.[2,3,7]

PV technologies can meet our energy demands due to the large amount of solar energy that strikes the earth's surface every day. **Figure 1.2** illustrates the amount of land that would be required in order to meet the energy requirements of each state, assuming a 13.5% efficient device.[8]

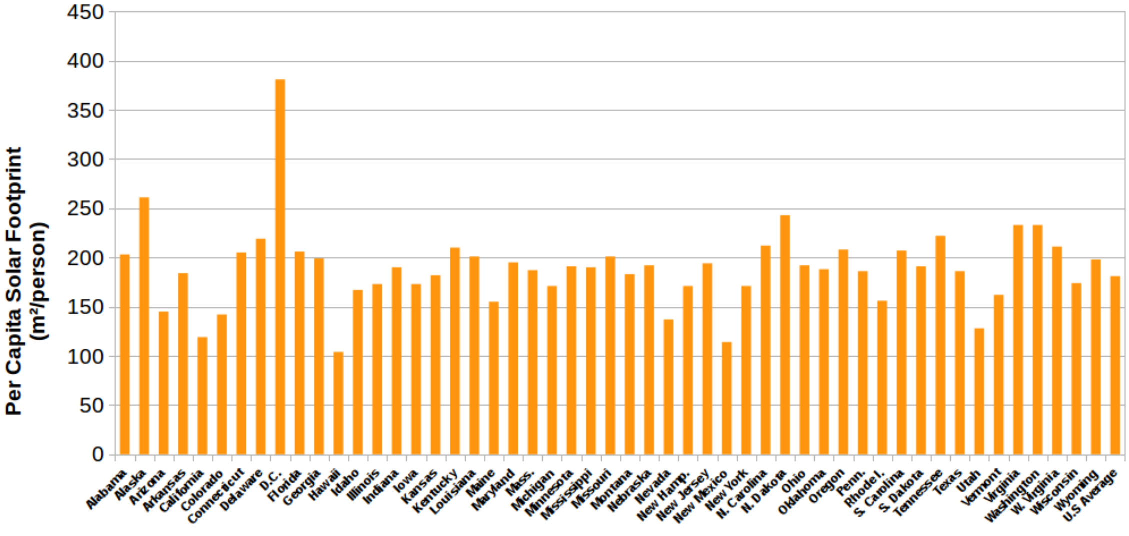

Figure 1.2: Amount of land required per state (per capita) in order to provide all energy from photovoltaics (13.5% efficiency). The data are calculated by using the per capita energy use for each state relative to the amount of geographic solar irradiance. Produced using data from the National Renewable Energy Laboratory (NREL).[8]

Therefore, although the energy needs of the United States can be completely met with PV, the amount of PV panels that must be manufactured in order to meet this need is staggeringly large. A good benchmark to use is that in order to make rapid progress towards producing a substantial amount of energy from PV in the near future, global production of new solar panels must reach the order of 1 gigawatt per day (1 GW/day).[9] With 1000 factories producing 10% efficient devices around the world in locations with an average insolation of 1000 W/m^2, this would amount to each factory producing 10,000 m^2 of PV area per day.[9] Although this value seems daunting, this level of production can be readily achieved by implementing low-cost printing techniques to manufacture PV materials and is comparable to the production levels for other printed materials.[10–12] For example, it is possible for organic PV modules to be printed at roughly 1 m^2/min using a roll-to-roll printer, so a factory with 10 such machines could easily approach 10,000 m^2 of daily PV production.[9]

1.2 General Photovoltaics Operation and Device Physics

The basic operation of a PV device consists of a semiconducting material with a bandgap (E_g) that is suitable to absorb the solar spectrum at the earth's surface. Generally, the photovoltaic process occurs when an incident photon is absorbed by this semiconducting material, thereby exciting an electron from the valence band (VB) to the conduction band (CB) of the material. In inorganic materials, the coulombic force that binds this electron and hole pair is sufficiently low due to the relatively large dielectric constant of the material, such that both the electron and hole can be treated as free charge carriers within their respective bands and can be effectively separated (charge separation). The excited state electrons and holes are subsequently collected at the cathode and anode of the device respectively (charge transfer). **Figure 1.3** illustrates this process

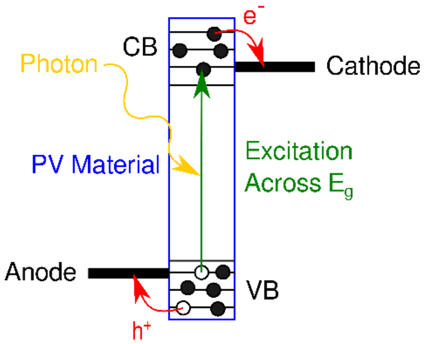

Figure 1.3: Schematic illustration of the photovoltaic process, where electrons (e^-) and holes (h^+) are excited across the bandgap (E_g) of a semiconducting material via an incident photon and are subsequently collected at the cathode and anode of the PV device respectively.

schematically.

Incident photons with sufficient energy will excite electrons from the VB to the CB depending on the bandgap of the material, thereby producing an electric current. However, this value is diminished by intrinsic loss mechanisms within the device. The efficiency of this current collection with respect to an incident photon wavelength is referred to as the external quantum efficiency (EQE) of a PV device. The EQE of a device is dependent upon several factors, as presented in **Equation 1.1**:

$$EQE(\lambda) = \eta_{abs}(\lambda) \times \eta_{cs}(\lambda) \times \eta_{ct}(\lambda) \qquad \textbf{(1.1)}$$

where $\eta_{abs}(\lambda)$ represents the efficiency of light absorbance, $\eta_{cs}(\lambda)$ represents the efficiency of charge separation, $\eta_{ct}(\lambda)$ represents the efficiency of charge transfer, and λ represents the wavelength.[13] Each of these components contribute to produce an EQE value at given wavelength. The upper bounds of these efficiencies are governed by the fact that excited state electrons will also necessarily recombine with holes to produce radiative recombination at a rate in accordance with the principle of detailed balance.[13] This detailed balance limit restricts the maximum power conversion efficiency of a PV device to be 33.7% for a material with an ideal bandgap of 1.34 eV and a single p-n junction (Shockley-Queisser limit).[13] **Figure 1.4** shows the standard AM1.5 solar spectrum overlaid with the EQE values of a theoretical PV device as an example. The representative device shown in Figure 1.4 has a relatively large bandgap that is unable to absorb much of the solar spectrum in the visible, near infrared and infrared regions. Moreover, the maximum EQE value of 60% is hampered by loss mechanisms within the device, such as low absorption, charge recombination, and inefficient charge transfer (Equation 1.1).

The voltage of a PV device is also dependent upon the bandgap of the semiconducting material, but is influenced by a number of other factors. In a perfect semiconducting material at

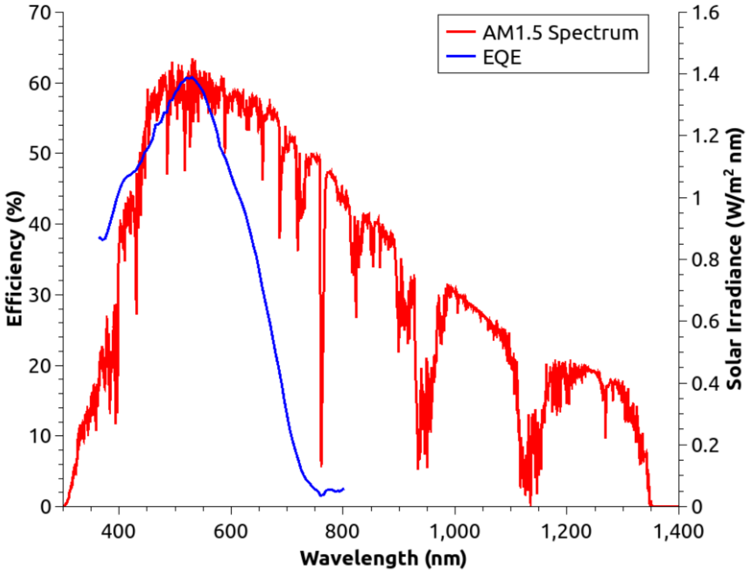

Figure 1.4: EQE data for a theoretical PV device that has a peak efficiency of around 60% located near the bandgap of the material (530 nm, 2.3 eV). The standard AM1.5 spectrum is overlaid for comparison.

thermodynamic equilibrium, the only available energy states within the material are located within the CB and VB, and the Fermi-level (μ) is probabilistically determined to be the energy at which there is a 50% chance of occupation. As such, μ typically falls between the CB and VB, as presented in **Figure 1.5a**. When the material is no longer at equilibrium, as is the case when it is irradiated for PV applications, the Fermi levels for electrons and holes must be considered separately. The quasi Fermi-level splitting (Δμ) denotes the difference in potential between electrons and holes in a non-equilibrium state, as illustrated in **Figure 1.5b**.[14] In addition, in an

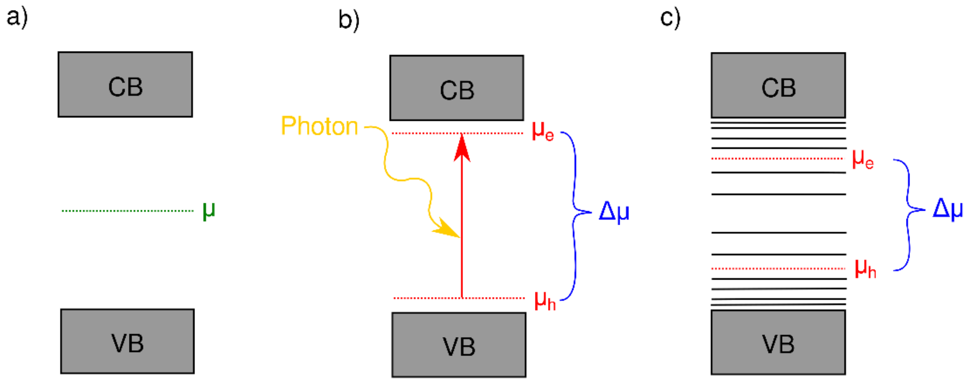

Figure 1.5: a) Ideal semiconducting material at equilibrium. b) Ideal semiconducting material in a non-equilibrium state after absorbing photons. c) Semiconducting material with sub-bandgap defect states in non-equilibrium.

imperfect semiconducting material, as is usually the case with printed PV, there is usually a population of surface-mediated sub-bandgap defect states that introduce new energy levels in the intraband region and shift the density of available energy states at the band edge, thereby causing band bending.[14] This phenomenon can lead to issues such as interfacial quasi Fermi-level pinning, which will further reduce the $\Delta\mu$ value and will lead to interfacial charge recombination and trapping. Moreover, imperfect materials can exhibit intrinsic defect states, which will introduce intraband energy states that will reduce $\Delta\mu$, can cause carrier trapping, and lead to recombination. This process is depicted graphically in **Figure 1.5c**.

The operating voltage of a PV device is dependent upon the quasi Fermi-level splitting, but is further reduced by losses in potential due to issues such as interfacial contact resistance and work function energy level alignments within a complete PV device. Therefore, the $\Delta\mu$ value can be considered a theoretical operating voltage of the device prior to other contributing factors. The current produced by a PV device is related to the EQE curve discussed previously (Figure 1.4) and can be thought of as the cumulative current produced across the solar spectrum. This value can be expressed using the integral presented in **Equation 1.2**:

$$J = \int EQE(\lambda)\Phi_{ss}(\lambda)d\lambda \qquad \mathbf{(1.2)}$$

Where Φ_{ss} represents the incident solar spectrum photon flux. This integral can be considered visually as the amount of area under the two curves relative to each other, as depicted in Figure 1.4. The power conversion efficiency (η_{pce}) of a PV device is determined by scanning the current output of a solar cell across a potential bias range within which the device operates (JV curve). A representative curve for a typical PV device is presented in **Figure 1.6**.

The η_{pce} of the device is calculated by determining the point along the curve that produces

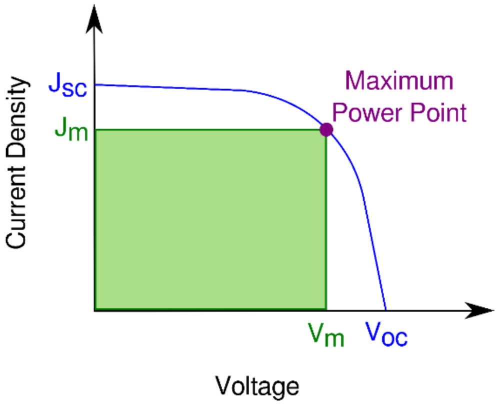

Figure 1.6: Current density vs. voltage curve for a PV device. J_m and V_m represent the current and voltage at the maximum power point respectively. J_{sc} represents the short circuit current density and V_{oc} represents the open circuit voltage. The green area represents the power output of the device at the maximum power point.

the maximum power output (maximum power point) as illustrated in Figure 1.6. The maximum power output of the device is equal to the product of the voltage and the current at the maximum power point, which are denoted by V_m and J_m respectively and can be visually represented as the area of the green rectangle in Figure 1.6. Accordingly, the power output of the device is maximized when the area of this rectangle is largest. The power conversion efficiency of the device can then be computed by dividing the power output of the cell with respect to the total incident power flux that strikes the surface of the solar cell (Φ_p), as presented in **Equation 1.3**:

$$\eta_{pce} = \frac{J_m V_m}{\Phi_p} = \frac{J_{sc} V_{oc} (FF)}{\Phi_p} \qquad \textbf{(1.3)}$$

Where (FF) represents the fill factor of the device, which is determined using **Equation 1.4**:

$$FF = \frac{J_m V_m}{J_{sc} V_{oc}} \qquad \textbf{(1.4)}$$

1.3 Cost of Conventional Photovoltaics

Although the cost of PV has diminished rapidly in recent years, the median price for installing PV systems remains above the cost for conventional energy sources (**Figure 1.7**).[15,16] In order for renewable energy sources to become cost competitive with fossil fuels, they must cost

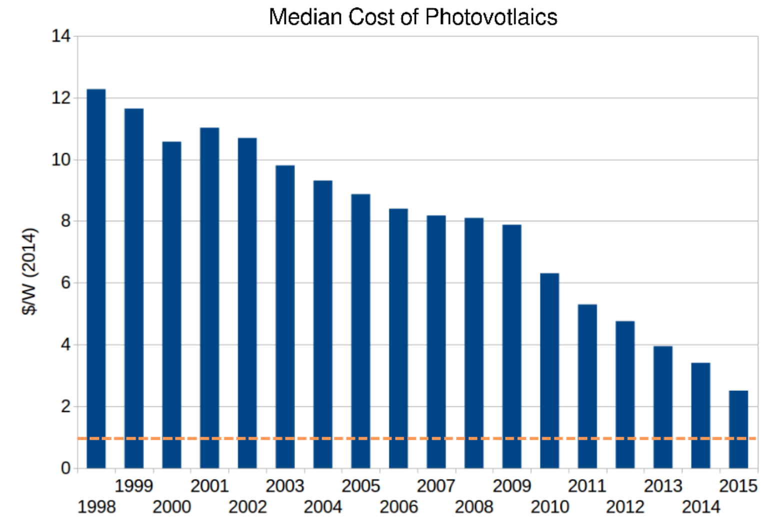

Figure 1.7: Historical median cost of PV systems. The yellow line represents the 1 $/W threshold for cost-competitiveness with fossil fuel energy sources. Produced using data from NREL and the U.S. Department of Energy.[15,16] Normalized for inflation relative to 2014 levels.

roughly one dollar per Watt ($1/W) of energy produced.[17–19] Although it is extremely encouraging that in some schemes the cost of PV systems has approached and in some instances even dropped below this $1/W value within the last several years, the cumulative amount of energy produced from PV remains low.[20] In fact, despite rapid growth of the industry, the total installed PV capacity within the United States remains orders of magnitude below the terawatt (TW) range that is required to meet a significant fraction of energy demand from PV (**Figure 1.8**). For comparison; 27,000 TWh of total annual energy consumption in the United States equates to approximately 3 TW of installed capacity. The widespread production of PV systems remains hampered by the exorbitantly large capital expenditures (CAPEX) that are required to build new PV production factories.[21,22] This high initial CAPEX cost can be attributed to several factors. First, conventional monocrystalline silicon requires very high temperature processing for high purity.[7,22,23] Next, since silicon is not a direct-gap semiconductor, these PV cells require a relatively thick layer of material, which further increases the cost. [7,22,23] Many steps of the process require expensive and complicated vacuum or chemical vapor deposition steps.[21] In addition, some technologies rely on

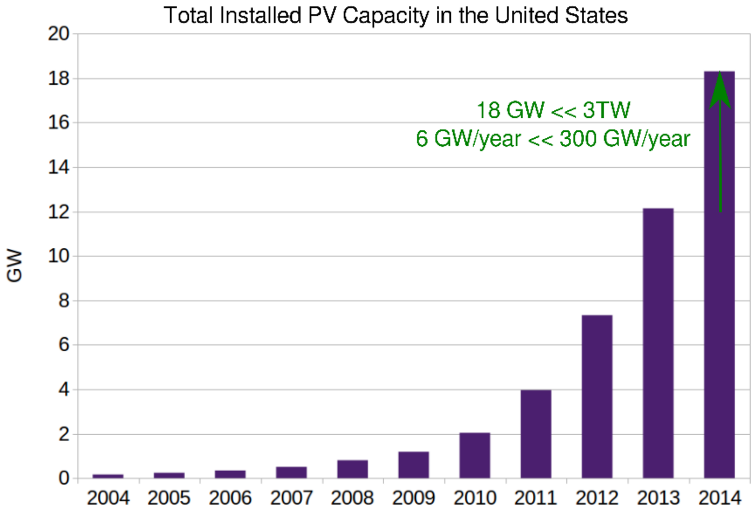

Figure 1.8: Annual PV capacity growth in the United States. Produced using data from NREL.[20]

rare metals that are extremely expensive.[24,25] Finally, these conventional technologies often require specially engineered substrates, such as coated glass, that can add to the overall cost of the PV module considerably.[26]

1.4 Chalcopyrite and Kesterite Photovoltaics

Although challenging, there are several routes that can be used to make progress towards the widespread production of cheap photovoltaics. Notably, if metal-sulfide materials can be manufactured using simple solution-processable techniques and low-temperature self-assembled materials, then this will reduce the cost of production and the related capital investments significantly.[27–31] These solution-processable materials offer a low-cost alternative to silicon based PV, where devices can be easily and rapidly printed in a high throughput fashion.[32–35] In particular, the chalcopyrite (**Figure 1.9a**) and kesterite (**Figure 1.9b**) class of materials such as the chalcopyrite $CuInS_xSe_{2-x}$ (CISSe), the gallium alloy variant $CuIn_xGa_{1-x}S_ySe_{2-y}$ (CIGSSe), and the earth-abundant kesterite variant $Cu_2ZnSnS_xSe_{4-x}$ (CZTSSe) have attracted considerable interest as alternative PV materials.[32–35] These materials have well-suited bandgaps within the approximate range of 1.5-1.0 eV that can be tuned by varying the relative ratios of selenium and sulfur, possess

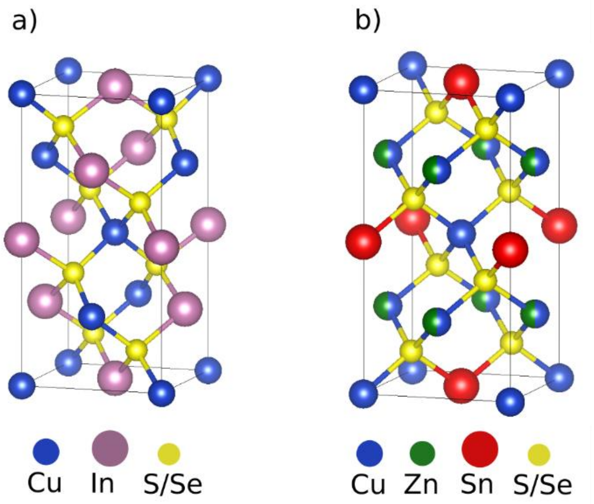

Figure 1.9: a) Chalcopyrite crystal structure of CISSe. b) Kesterite crystal structure of CZTSSe.

direct bandgaps for high absorbance coefficients thereby allowing them to be used in thin film applications, and can be synthesized using self-assembled nanoparticle growth techniques.[32–38]

1.5 Printed Photovoltaics from Conventional Nanoparticle Inks

Most conventional metal-sulfide nanoparticle synthesis methods employ some variation of a hot injection procedure, where metal salt precursors are dissolved in an aliphatic high boiling point solvent such as oleylamine (OLA). The solution is purged with an inert gas and is heated to a reaction temperature around 200 °C. A mixture of sulfur precursor and an aliphatic ligand is then injected into the heated solution through a septum, which acts as a reducing agent that triggers nanoparticle nucleation and growth, resulting in metal sulfide nanoparticles.[28,29,31,39] The hot injection method facilitates the rapid nucleation of seed crystallites, which is followed by a slower growth process that is governed by diffusion and various intermediary precursor reaction steps.[39–42] In the first regime, the rapid addition of the sulfur precursor saturates the mixture with reaction monomers and the energy barrier for nucleation is overcome, the formation of small seed crystallites is energetically favorable, and the critical nucleus size is reduced. In the following regime, as subsequent reaction monomers are consumed, the critical nucleus size increases, smaller nanoparticles become unstable, and the nanoparticle growth proceeds via a diffusion process.[43] This bimodal growth process is depicted in **Figure 1.10**, where an initially rapid nucleation phase followed by a slower growth phase, allows for the creation of crystalline, monodisperse nanoparticles.[43–46] The typical procedure for a hot injection nanoparticle synthesis is presented in **Figure 1.11**.

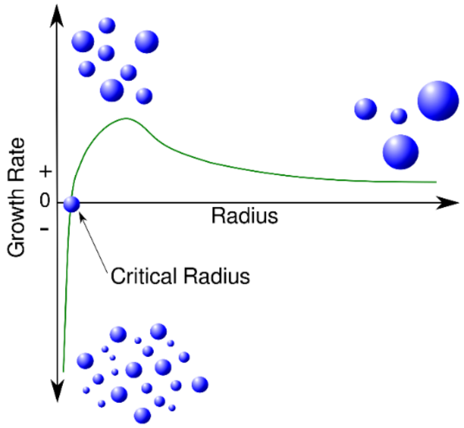

Figure 1.10: Illustration of a standard nanoparticle growth scheme. First, a large population of initial seed crystallites forms. Next, some of these crystallites are above the critical radius and continue to grow, while some disappear. Finally, the particles undergo a diffusion mediated growth process, where some smaller particles are consumed.

The aliphatic ligand plays several important roles in this process. First, it acts as the high boiling point solvent for the reaction, so that the diffusion mediated nanoparticle nucleation and growth processes can take place. Next, it has been shown that organic ligands can play a crucial role in activating precursors via intermediary reaction steps.[41] Finally, the aliphatic ligands form a

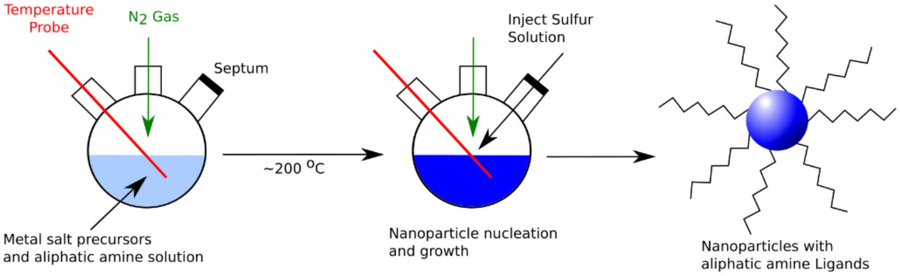

Figure 1.11: Typical hot injection procedure for producing metal-sulfide nanoparticles, where metal salt precursors are dissolved in a high boiling point solvent such as oleylamine. The solution is then heated and the sulfur precursor solution is injected into the mixture, which initiates nanoparticle nucleation and growth. This produces nanoparticles that have coordinating aliphatic amine ligands.

coordination bond with the nanoparticle surface, thereby forming a ligand that stabilizes the nanoparticles, prevents agglomeration via steric repulsion and solubilizes the nanoparticles.[43]

Stabilized metal-sulfide nanoparticles can be concentrated into an ink and printed onto a substrate using simple printing techniques.[28,29,31] The printed nanocrystal layer is then annealed in a Se rich atmosphere to promote grain growth and the sintering of nanoparticles, as well as the formation of the selenized photovoltaic absorber layer via a vapor-phase substitution reaction.[28,29,31,36] The general procedure for producing a photovoltaic absorber layer via this method is outlined in **Figure 1.12**. Although this process allows for the fabrication of printed metal-chalcogenide films, it still requires high-temperature processing and vapor-phase reactions, both of which add to the complexity and cost of implementing these methods on a large scale. Moreover, the presence of conventional aliphatic ligands leads to the formation of carbon impurities than can drastically influence device performance.[47]

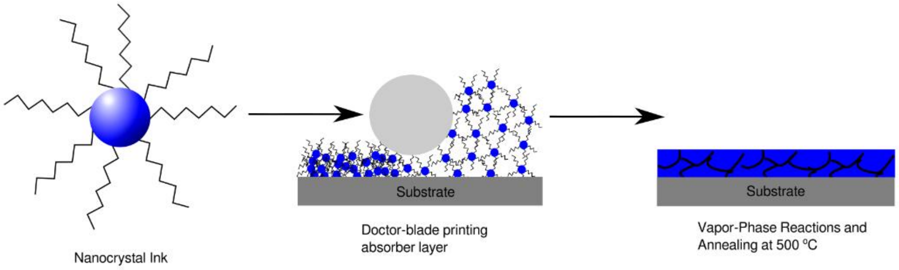

Figure 1.12: A colloidal metal-sulfide nanoparticle ink is printed onto a substrate using a doctor-blade technique and is subsequently annealed at 500 °C in the presence of Se vapor, which sinters the nanoparticles together, promotes crystallization, and causes a vapor-phase reaction to occur.

1.6 A New Nanoparticle Synthesis Paradigm

Although proven useful for synthesis, conventional aliphatic ligands present a number of challenges for the implementation of nanoparticles in photonic and electrochemical devices. Aliphatic ligands are highly insulating, hydrophobic, and constitute a significant barrier to electrochemical surface reactions.[48] Accordingly, several studies have developed ligand exchange and ligand stripping protocols that replace these aliphatic ligands with functional moieties or that strip away the ligands to reveal a bare nanoparticle surface.[48–50] These reactions, however, pose several intrinsic problems. They significantly add to the complexity of the synthetic process, do not always go to completion, and can deteriorate the surface of the nanoparticles, which can in turn impose significant problems during device fabrication when using these techniques (**Figure 1.13**).[51,52] In addition, these procedures often do not work for chalcopyrite or kesterite materials, which have much more complicated crystal structures and surface chemistries than binary chalcogenide particles.[52]

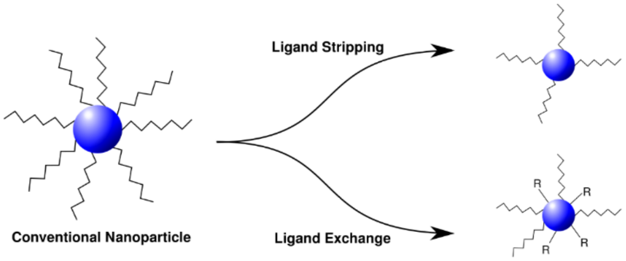

Figure 1.13: Ligand stripping and ligand exchange procedures do not always go to completion and can be challenging for chalcopyrite and kesterite materials.

If chalcogenide particles can be synthesized without conventional aliphatic ligands and without the need for complicated surface chemistry reactions, then this would provide a means for rapidly functionalizing one batch of nanoparticles with a spectrum of molecules (**Figure 1.14**).[49,50,53] For example, it has been shown that sodium can help passivate surface defects within these devices, however this can be difficult to achieve using conventional nanoparticle ligand chemistry.[54–56]

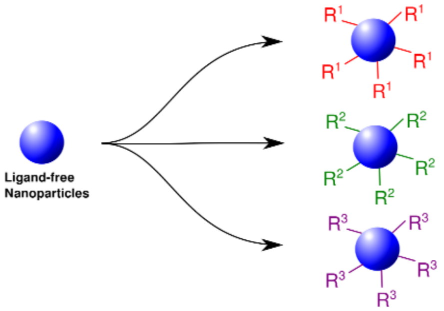

Figure 1.14: Nanoparticles synthesized without conventional ligands can be functionalized with a spectrum of molecules aimed at improving device performance and passivating surface defects.

In addition, nanoparticles that do not have conventional aliphatic ligands would eliminate the source of carbon impurities that can detrimentally affect device performance (**Figure 1.15**).[47] Moreover, a ligand-free nanoparticle ink provides unique opportunities to print PV absorber layers using low-temperature annealing procedures without vapor-phase reactions (Figure 1.15).

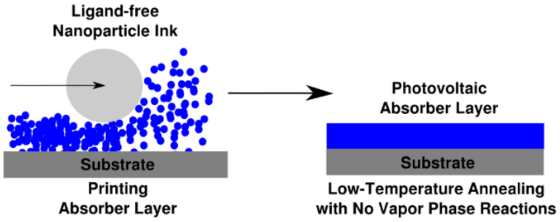

Figure 1.15: Nanoparticles synthesized without conventional ligands via a chalcogenide polymer can be used to print PV devices that do not have carbon impurities and that can be processed at low temperatures without complicated vapor-phase reactions.

1.7 Conclusions and Research Goals

The first goal of this work was to investigate the role of conventional aliphatic ligands in printed nanoparticle-based devices. Using this knowledge as a starting point, the next goal of this work was to develop a method to utilize chalcogen polymers to synthesize chalcopyrite and kesterite nanoparticles that do not have conventional aliphatic coordinating ligands. These nanoparticle inks can then be used to print photovoltaic absorber layers without the pyrolized graphitic carbon that forms from these ligands, that can drastically influence the final absorber layer morphology, and that can detrimentally impact device performance.[47] In addition, nanoparticles with chalcogenide surface species and no aliphatic ligands can be processed at low temperatures to produce a material with excellent bulk properties.[57–59] Furthermore, incorporating both sulfur and selenium into the polymer backbone provides a way to incorporate both chalcogens simultaneously, without the vapor-phase reactions that are otherwise needed.[28,29,31,36] Accordingly, the second goal of this work is to use these chalcogen polymer and nanoparticle inks to fabricate low cost, completely solution-processed PV devices that are annealed at a low temperature.

Chapter 2. Conventional Nanoparticle Ligands and Pyrolized Carbon in Printed CZTSSe devices

2.1 Introduction

Although a solution-processable solar cell can be fabricated from a conventional nanocrystal ink using the methods outlined in the previous chapter, the presence of coordinating organic ligands results in residual carbon in the final device absorber layer after the nanocrystals are annealed and sintered.[34,35,47,60–62] The work within this chapter was motivated by the relatively poorly understood nature of carbon in annealed nanocrystal-based photovoltaic devices. Despite the fact that similar synthesis techniques are utilized for a range of nanocrystalline-based photonic devices, prior to this work very little was known about how these ligands can potentially become chemically incorporated into a device.[28,34,35,60,61,63,64]

CZTSSe PV devices were fabricated using CZTS nanoparticles that were synthesized using two different coordinating aliphatic ligands: oleylamine (OLA), which is a commonly used ligand that contains one double bond along the aliphatic chain and dodecylamine (DDA), which is a shorter molecule that contains no double bonds.[47] Next, these colloidal nanocrystal inks were doctor bladed onto a molybdenum coated soda lime glass (SLG) substrate, and the resulting film was placed into a furnace with selenium vapor and argon gas to sinter the nanoparticles into a dense thin film with large crystalline domains of the sulfoselenide. This annealed film was then coated with a CdS n-type layer, a ZnO passivation layer, a transparent conducting ITO layer and aluminum top contacts to form a complete device.[31] Two different ligands were used in order to examine how they influence the properties of the thin-film material. Although both ligands produce nanoparticle inks with comparable properties, the PV devices that were made using the two different nanoparticle inks exhibited drastically different device performances.

In order to investigate the nature of the ligand's influence on device performance, the sintered CZTSSe layers (without the top-layers necessary for PV devices) were examined using several spectroscopic techniques including Raman, Fourier transform infrared (FTIR), X-ray photoelectron (XPS), photoluminescence (PL), and energy dispersive x-ray (EDS) measurements. X-Ray diffraction (XRD) was also performed to examine the crystal structure of the absorber layers and scanning electron microscopy (SEM) was performed to examine grain size and morphology of the films.

One study by Kim *et al.* showed that OLA will undergo a crosslinking reaction with elemental sulfur during the nanoparticle synthesis, thereby producing a high molecular weight network copolymer.[65] In addition, it has been shown that elemental sulfur will be reduced by the aliphatic amine ligands at the alpha carbon site prior to reacting with the metal precursors.[41] Therefore, this work also examined how the chalcogens affect the structure of carbon residues in the absence of the metal precursors. Specifically, this work investigated the carbon films that are produced when the ligand molecules alone are reacted with elemental sulfur in solution, drop-cast onto a substrate and then annealed/selenized in an argon atmosphere (in the absence of the metal precursors to form CZTS).

2.2 Methods

2.2.1 Substrate Preparation

Every substrate used in the study was cleaned by sonicating in a solution of Micro 90 detergent and deionized water, in clean deionized water, in acetone and then in isopropanol, each for ten minutes. The substrates were finally cleaned with an air plasma for 10 minutes.

2.2.2 Conventional CZTS Nanocrystal Synthesis

Two different ligands were used to synthesize CZTS nanocrystals using a method developed by Guo *et. al*.[31] Specifically, copper (II) acetylacetonate (Cu(acac), 1.5 mmol, 99.99%, Aldrich), zinc acetylacetonate (Zn(acac), 0.75 mmol, 99.995%, Aldrich), and tin(IV) bis(acetylacetonate) dibromide (Sn(acac), 0.75 mmol, 98%, Aldrich), and the two ligands (10 mL) were added into a 100 mL three-neck flask connected to a Schlenk line. The mixture was heated to 130 °C under vacuum and degassed for 30 min and purged with nitrogen several times. The temperature was then raised to 225 °C, and 3 mL of a 1 M solution of sulfur dissolved in the corresponding ligands was injected via syringe through a septum (Figure 11). For DDA the temperature of this 1 M solution was raised to 40 °C to facilitate the dissolution of elemental sulfur prior to injection. After injection, the temperature was held at 225 °C for 30 min. The mixture was then cooled to 80 °C by lifting the flask off of the heating mantle. The nanoparticles were dispersed in a mixture of toluene and isopropanol, and were subsequently collected by centrifuging for 10 min at 10,000 rpm.

2.2.3 Conventional CZTS Nanocrystal Thin Films

Nanoparticle thin films were prepared by using previously established doctor-blade printing techniques.[31] Specifically, the CZTS nanoparticles were diluted (200 mg) in toluene (1 mL). This slurry was then pipetted onto a cleaned Mo coated SLG substrate in 7 µL increments. The slurry was printed onto the substrate using a doctor-blade printing technique with a 125 µm thick spacer and rapidly dried on a hot plate set at 300 °C in a fume hood for 10 s.

2.2.4 Thin Film Annealing and Concurrent Selenization

The films were placed in a graphite box and then were placed in a controlled atmosphere tube connected to a tube furnace. The tube was purged with vacuum and argon several times to remove air and residual water vapor. The furnace was heated to 500 °C while the sample remained outside of the furnace. Once the furnace reached a stabilized temperature, the sample was then placed into the furnace using a sealed pushrod. All samples used in this study were annealed for 20 minutes. For studies where selenium vapor was used during annealing, approximately 400 mg of selenium was placed in the graphite box next to the samples (six selenium pellets).

2.2.5 Photovoltaic Device Fabrication from Conventional Nanoparticle Ink

Complete photovoltaic devices were fabricated using previously reported methods.[31] Briefly, nanoparticle thin films were printed using the doctor-blade techniques outlined in section 3.3. The films were then briefly dried on a hot plate and subsequently annealed and selenized according to the procedure outlined in Section 3.4. The selenized films were then treated by a chemical bath deposition of CdS, RF sputtering of ZnO and ITO top layers and thermal deposition of aluminum top contacts to form a complete device. Six samples were prepared on 2.5 cm by 2.5 cm substrates (three for each ligand), each patterned with 35 individual devices, where each device had an area of 0.116 cm^2. Each device was electrically isolated by scribing away the thin film material between adjacent devices at a fixed distance interval. This scribing process also yields a consistent device area.

2.2.6 Photovoltaic Device Characterization

The efficiency of each device was calculated by examining the current versus voltage (IV) curves using a Keithley digital multimeter while the devices were illuminated using a simulated AM1.5 solar spectrum from a xenon source lamp at an intensity of 100 mW/cm^2. 5-8 of the best performing devices from each substrate were selected to calculate the device performance data, for a total of 15-20 devices for each device performance value that is presented.

2.2.7 Photoluminescence and Raman Spectroscopy Measurements

A modified Horiba Labram HR instrument was used to collect both photoluminescence (PL) and Raman spectra through a confocal objective lens. Raman data were collected with 532 nm excitation. A 5 s exposure was repeated and accumulated 50 times to produce the spectra. A 10× Olympus achromat dry objective lens with a confocal aperture hole of 200 µm and a grating with 1800 lines/mm (blazed at 750 nm) were used along with a Si CCD detector to collect the data. The laser excitation power was 0.6 mW.

The PL data were collected with 785 nm excitation using an InGaAs array detector to collect the NIR emission. A 3 s exposure was repeated and accumulated 4 times to produce the spectra. A 10× Olympus achromat dry objective lens, an aperture hole of 800 µm and a grating with 150 lines/mm (blazed at 1200 nm) were used. The laser intensity was adjusted to give an incident power density of approximately 10 suns-equivalent (after focusing from the objective). PL measurements were analyzed using a previously reported method, where the PL emission peak yields the bandgap and the quasi-Fermi level splitting of the devices through the implementation of a curve fitting algorithm.[66] 5-8 of the best performing devices (the same devices that were used for device characterizations) from each substrate were analyzed, for a total of 15-20 devices for each value.

2.2.8 Attenuated Total Internal Reflectance Fourier Transform Infrared Spectroscopy

Attenuated Total Internal Reflectance (ATR) Fourier Transform Infrared Spectroscopy (FTIR) measurements were conducted with a Perkin Elmer FTIR spectroscope using an ATR crystal. The thin film samples were analyzed by physically pressing the surface of the thin films into contact with the ATR crystal and data was collected in the wavenumber range of 200 cm^{-1} to 3000 cm^{-1}.

2.2.9 Transmission Electron Microscopy

The nanoparticle solutions were imaged by drop casting diluted ink solutions (1 mg/ mL) directly onto a sample holding grid with a holey carbon support film and a 400 mesh copper TEM grid (Ted Pella, Inc.). This TEM grid was placed in a vial and held under vacuum overnight, to remove any residual solvent from the sample. The nanoparticles were imaged on an FEI Tecnai G2 F-20 TEM with a 200 kV accelerating voltage and a spot size of 3. Some samples were also examined with an attached Energy Dispersive X-ray Spectroscopy (EDS) detector or a Selected Area Electron diffraction detector (SAED).

2.2.10 X-ray Diffraction

X-ray diffraction patterns (XRD) were collected for both pre-annealed and annealed nanoparticle films using 7000 data points at a scan rate of 1 data point per second with a Bruker F8 Focus. A Cu-Kα X-ray source with an incident wavelength of 1.54059 Å was used. A single crystal silicon wafer was used to determine the instrument broadening, where the FWHM was calculated to be approximately 0.115 2ϴ.

2.2.11 X-ray Photoelectron Spectroscopy

X-ray photoelectron spectroscopy (XPS) was performed using a custom-built instrument that contains a Leybold Heraeus emission regulation X-ray source (865920) and an EA-11 150 mm hemispherical analyzer. A collimated Mg Kα x-ray source (1253.6 eV) illuminated a large area of the sample and the position was adjusted to coincide with the analyzer focal point. Mg Kα was chosen to avoid interference between photoemission peaks of interest and the abundant Se Auger spectrum on the binding energy scale, which overlaps significantly when using Al Kα (1486.7 eV). All data were taken at a 90° takeoff angle. To account for uniform sample charging, all data have been shifted so that C 1s appears at 284.8 eV.

2.2.12 Energy Dispersive X-ray Spectroscopy and Scanning Electron Microscopy

Scanning Electron Microscopy (SEM) and a concurrent Energy Dispersive X-ray Spectroscopy (EDS) measurement were performed on both the pre-annealed and annealed thin films with an FEI Sirion XL30 microscope and an attached Oxford EDS detector. The data were collected without a sputtered conductive layer, in order to minimize the background signals present in the EDS spectra and obtain a qualitative measurement for the amount of carbon present in each sample. The bulk EDS data were obtained by gathering data sets at 5-7 different locations on the substrate in order to examine the stoichiometric range of the material. The images were collected using a spot size of 3 and an accelerating voltage of 10 kV. For EDS measurements, the spot size and accelerating voltage were increased to 5 and 20 kV respectively.

2.3 Results and Discussion

The PV devices that were made using the two different nanoparticle inks exhibited drastically different device performances, despite the analogous properties of the starting nanoparticle inks. Complete photovoltaic devices were made using annealed/sintered CZTSSe nanocrystal films and were characterized to determine device power conversion efficiency (PCE), open circuit voltage (V_{OC}), short circuit current density (J_{SC}) and fill factor (*FF*). The photoluminescence (PL) spectra were collected, and peak fitting algorithms were used to extract the bandgap energy (E_g) and the quasi-Fermi level splitting values ($\Delta\mu$) from the PL data.[56,66,67] Representative *JV* curves and PL spectra are presented as **Figure 2.1** and **Figure 2.2** respectively.[47] Because the illumination intensity used in PL testing is higher than the AM1.5 illumination intensity used in device efficiency testing (roughly 10 suns-equivalent), the V_{OC} and $\Delta\mu$ cannot be directly compared. However, the $\Delta\mu$ indicates the relative amount of defects present in a PL material, since a higher level of mid bandgap defect states will diminish the $\Delta\mu$ value.[66] The data

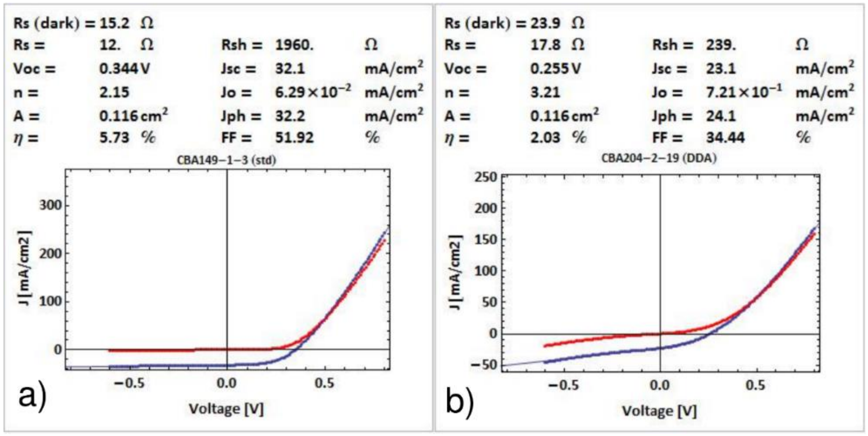

Figure 2.1: Representative device JV data for a) OLA and b) DDA based devices.[47]

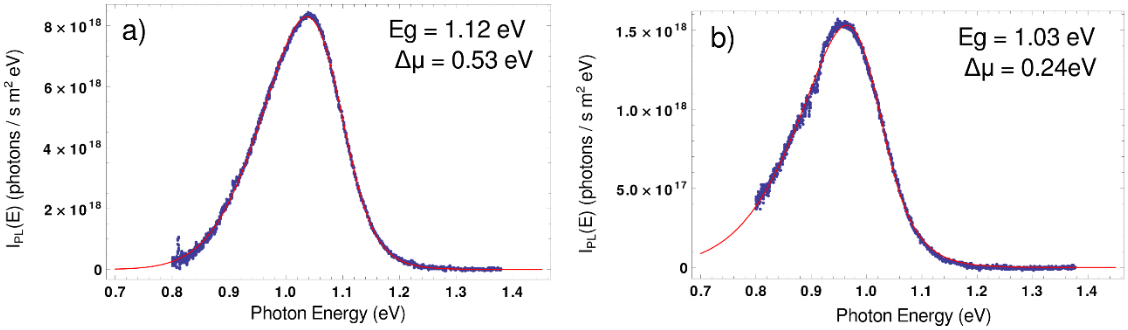

Figure 2.2: Representative device PL data for a) OLA and b) DDA based devices.[47]

for the devices is presented in **Table 2.1**, along with the corresponding standard deviation to show the reproducibility of device performance. The OLA and DDA based photovoltaic devices

Table 2.1: Performance Characteristics of CZTS Photovoltaic Devices

Ligands	**OLA**	**DDA**
Δμ (eV)	0.52 ± 0.02	0.20 ± 0.04
E_g (eV)	1.11 ± 0.02	1.02 ± 0.02
PCE (%)	4.7 ± 0.7	1.1 ± 0.7
V_{OC} (V)	0.36 ± 0.03	0.21 ± 0.04
J_{SC} (mA/cm^2)	32.2 ± 6.4	15.4 ± 4.8
FF	42.5 ± 10.0	29.9 ± 3.9

exhibited significantly different performance characteristics, where the DDA based devices have a significantly lower PCE and Δμ, which is indicative of presence of comparatively more sub band defect states.

Despite a significant variation in device performance, the properties of the CZTS nanoparticles are remarkably similar before the annealing/selenization step. XRD and TEM revealed nanoparticles with comparable sizes and crystal structures, as presented in **Figures 2.3 and 2.4**.[47] Using the Scherrer equation and the (112) peak presented in Figure 2.3, the crystallite size of the OLA based nanoparticles was estimated to be 36 ± 10 nm, while the crystallite size of the DDA based nanoparticles was estimated to be 34 ± 13 nm. The pre-annealed films were also examined with ATR FTIR, which revealed the presence of aliphatic ligands prior to the annealing step.[47] Next, CZTS nanoparticle films were annealed in an inert atmosphere and in the presence of selenium vapor, to produce CZTSSe films in a manner commensurate with device fabrication methods. These annealed films were examined with XRD, Raman, XPS, SEM and EDS techniques. The XRD spectra presented in **Figure 2.5**[47] show that both OLA and DDA based films produce diffraction patterns situated between that of fully sulfurized CZTS and fully selenized CZTSe.[29] There is a linear relationship between the lattice constant and the relative amount of S/Se

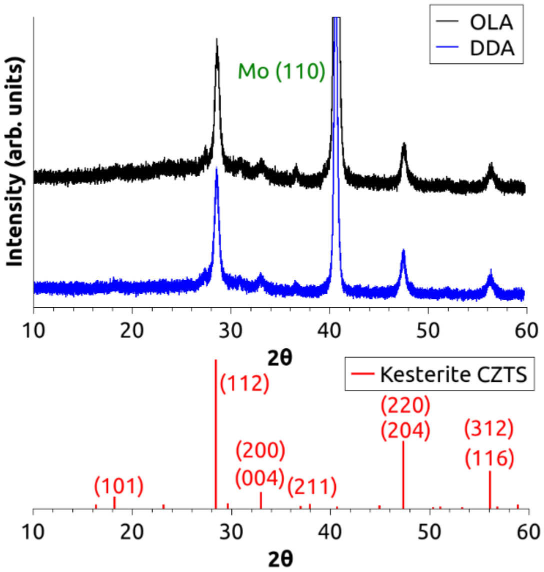

Figure 2.3: XRD spectra with reference diffraction pattern for pre-annealed CZTS nanoparticle films synthesized using OLA and DDA ligands on a Mo coated substrate. The data have been offset for clarity.[47]

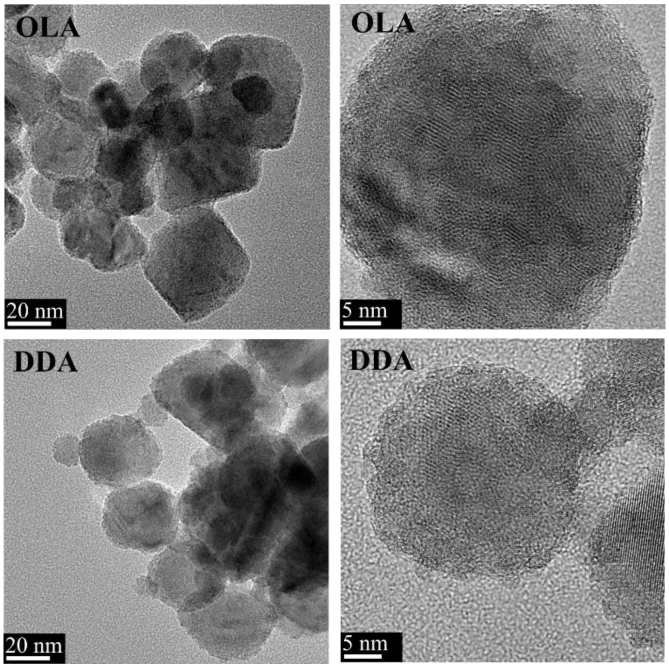

Figure 2.4: TEM images of CZTS nanoparticle inks synthesized using OLA and DDA ligands.[47]

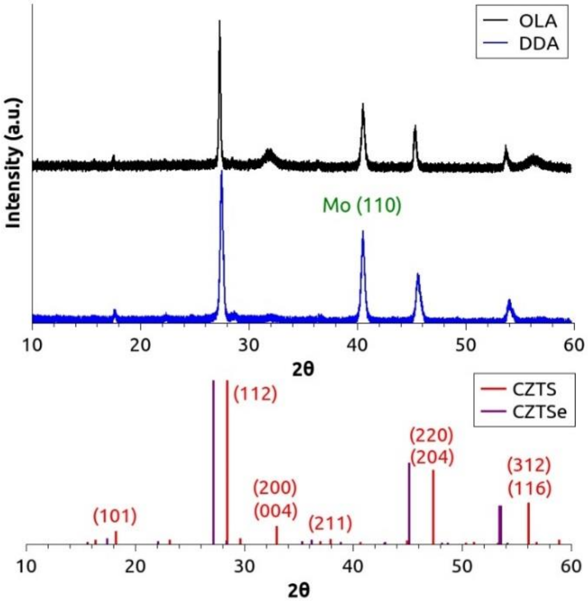

Figure 2.5: XRD spectra with reference diffraction patterns for an-nealed CZTSSe nanoparticle films synthesized using OLA and DDA ligands on a Mo coated substrate. The data have been offset for clarity.[47]

substitution.[29] Accordingly, the lateral shift in the XRD spectra relative to the CZTS and CZTSe standards can be used to calculate that the OLA based material is approximately 93% selenized and that the DDA based material is approximately 81% selenized. As the amount of selenium substitution increases, the bandgap of the material will decrease from 1.48 eV to 0.96 eV.[37,68,69] Although the XRD data indicate that the OLA based material has more selenium incorporation, the OLA based material bandgap presented in Table 2.1 is larger than the bandgap of the DDA based material. This can be explained by the fact that the DDA based material has a larger population of sub-bandgap defect states, which will cause the PL measurement to yield a lower bandgap value.[70,71]

The Scherrer equation can be used to show that the OLA based material has crystallite sizes of 95 ± 15 nm and the DDA based material has crystallite sizes of 58 ± 8 nm. For the OLA based material, the FWHM measurement is dominated by instrument broadening and so this measurement is at the upper limit of the crystallite size range that can be measured using this technique. In addition, the Raman data presented in **Figure 2.6**[47] show peaks consistent with the formation of kesterite CZTS and CZTSe.[72–74] Moreover, the peaks associated with CZTSe are more intense in the OLA based sample, which further confirms the presence of larger crystallites with fewer grain boundary defects. The spectra also show that the DDA based sample exhibits a more prominent CZTS peak at 234 cm^{-1}, which is consistent with the slightly lower extent of

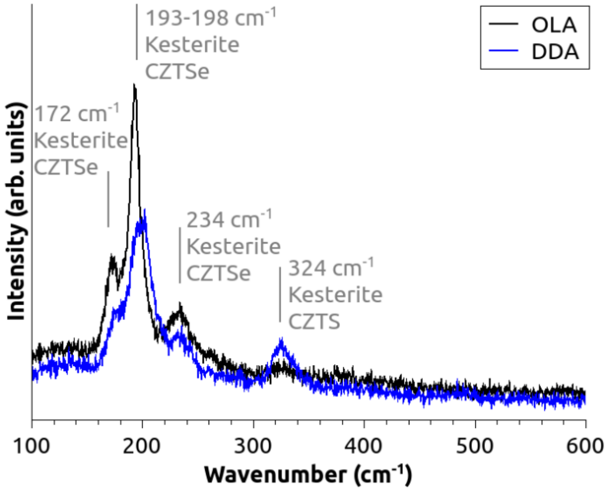

Figure 2.6: Raman spectroscopy for the annealed CZTS/Se nanoparticle films.[47]

selenization seen in the XRD data.

Raman spectroscopy was also conducted in the higher wavenumber region. **Figure 2.7**[47] shows a bimodal set of peaks that is characteristic of graphitic carbon. The presence of the graphene peak (G), as well as a relatively prominent disorder peak (D), and the absence of the sp^3 bond peak at 1180 cm^{-1} indicates that the carbon is composed of disordered sp^2 bonded graphitic carbon.[75–77]

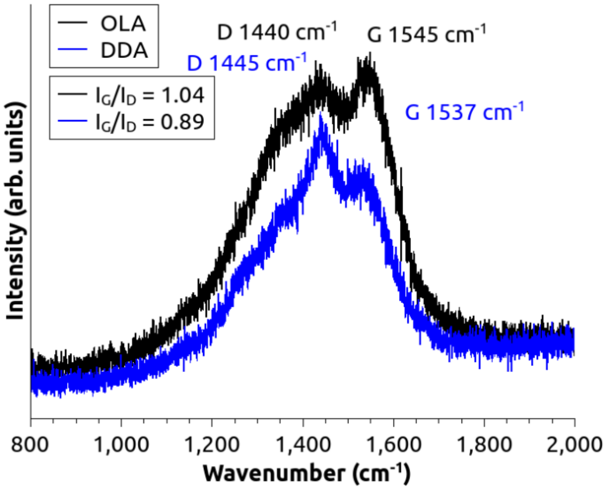

Figure 2.7: Raman spectroscopy for graphitic carbon within the annealed CZTS/Se nanoparticle films. The locations of the D and G peaks are shown, along with the ratios between the intensities of the two peaks.[47]

Furthermore, the ratios between the D and G peaks can be calculated to produce a comparative estimate of the amount of disorder present in the carbon. This peak ratio can be combined with empirically derived trends to roughly estimate the crystallite size as being approximately 4.6 nm for OLA and 3.8 nm for DDA using **Equation 2.1**, where L_a is the estimated size of the graphitic crystallite and C(λ) represents an empirically derived constant equal to 4.4 nm for an incident laser wavelength of 515 nm.[78,79]

$$\frac{I_D}{I_G} = \frac{C(\lambda)}{L_a} \qquad \textbf{(2.1)}$$

Therefore, the data indicate that the carbon derived from the ligands is composed of disordered graphitic carbon with an approximate crystallite size of 3-5 nm, where the OLA ligands produce a more ordered graphitic carbon with larger crystallites. It is important to note that the peak locations in Figure 2.7 are shifted slightly relative to typical graphitic carbon (where the D peak is located at 1360 cm^{-1} and the G is located at 1580 cm^{-1}) due to changes in bonding resonances with the introduction of CZTS crystals. This result is expected, since it has been shown that imposing new stresses on a graphitic lattice, such as those stresses that are introduced with the addition of sintered CZTS crystals, will shift the D and G resonance modes.[75]

XPS data were also collected on the films, in order to compare stoichiometry and oxidation states. The survey spectra presented in **Figure 2.8** are very similar, except for the C 1s peak, where the OLA based film produces a significantly more intense peak.[47] This can be attributed to the fact that OLA is a larger molecule than DDA and contains more carbon atoms per ligand. Moreover, the similarities in the spectra indicate similar oxidation states and stoichiometries.

In order to compare the morphological and stoichiometric differences between the annealed absorber layers, SEM and EDS were performed on both the pre-annealed and annealed CZTS/CZTSSe films. **Table 2.2** shows the EDS data for the 4 different types of films that were

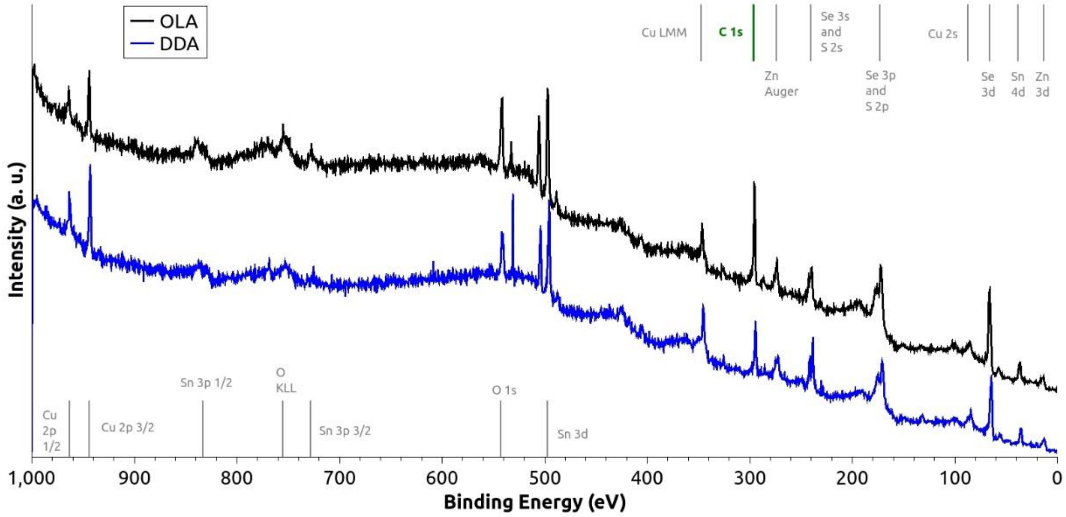

Figure 2.8: XPS survey of the annealed CZTSSe absorber layer films. The films show analogous spectra, indicating similar oxidation states and stoichiometries. However, the OLA based film shows a larger C 1s peak, which can be attributed to the presence of more carbon in the films due to the large OLA ligand. The data have been offset for clarity.[47]

Table 2.2: Stoichiometric ratios for pre-annealed and annealed CZTS/CZTSSe films

Thin Film	Cu/(Zn+Sn)	Zn/Sn
OLA Pre-annealed	1.19 ± 0.44	0.92 ± 0.28
DDA Pre-annealed	1.10 ± 0.09	0.90 ± 0.06
OLA Annealed	1.09 ± 0.20	0.78 ± 0.12
DDA Annealed	1.04 ± 0.45	0.83 ± 0.29

analyzed, where the error in the measurements is due to the slight stoichiometric variation that occurs in the films at the millimeter length scale.[47] It has been previously reported that CZTSSe stoichiometry will vary within this range and that this plays a role in determining final device performance.[56,80,81] From the EDS data presented in Table 2.2 and the XPS data presented in Figure 2.8, it can be concluded that the OLA and DDA based thin films exhibit similar stoichiometries, however the final device performance of the films is not equivalent. It has been shown that despite compositional inhomogeneity in CZTS particles, the resulting annealed CZTSSe film will have a much more uniform stoichiometry.[82] Therefore, these data indicate that the variations in device performance presented in Table 2.1 are due to other factors beyond stoichiometric variation. In addition, since it has been shown that the ligands play a role in the synthetic pathway of nanoparticle formation, these data in conjunction with the XRD spectra presented in Figure 2.3 and the TEM images presented in Figure 2.4 indicate that the OLA and DDA based ligands have similar reaction pathways.[41,82] Both methods produce nanoparticles with similar stoichiometries, crystallite sizes, crystal structures and particle sizes.

In order to examine the grain size and morphology of the annealed films, the films were examined with SEM and a concurrent EDS line-scan measurement. The SEM images in **Figure 2.9** show that after annealing, the OLA based films produce an absorber layer with larger grains and less surface roughness, while the DDA based films produce smaller grains that are more

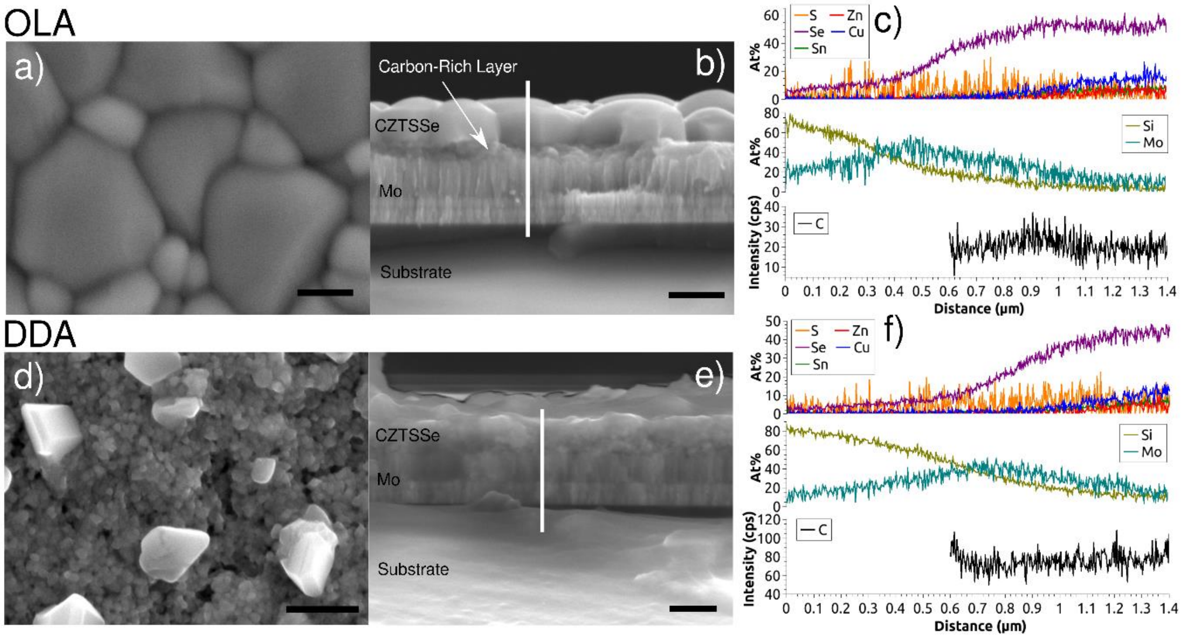

Figure 2.9: a) and d) show the top-down SEM images for the OLA and DDA based films respectively. b) and e) show the cross-sectional SEM images for the OLA and DDA based films respectively, where the white line represents the EDS line-scan region for each. The black scale bars present in the SEM images are 500 nm. c) and f) show the EDS line-scan data for the OLA and DDA based films respectively.[47]

disjointed. In addition, the SEM images show that the OLA based film in exhibits a distinct layer beneath the CZTSSe grains and at the substrate interface, whereas the DDA based film does not have this distinct layer. The existence of this "carbon-rich fine-grain" layer has been reported in the literature, although it has not been widely studied.[63,64,82,83]

It is important to note that the spatial resolution of EDS is on the order of the film thickness, so the EDS line-scan data presented in Figures 2.9c and 2.8f should be considered qualitatively only. In addition, the carbon signal can be influenced by the presence of carbon within the microscope chamber as well as the presence of the conductive carbon tape that is used to mount the samples into the sample holder. Despite these limitations however, the EDS line-scan data is consistent with what is presented in Table 2.2 and a small increase in the carbon signal is seen in Figure 2.9c at the fine-grain layer at approximately 0.9 µm, thereby indicating that this layer is in fact carbon-rich. The DDA based sample however, shows a constant carbon signal. The carbon data have been truncated due to an increasing background signal from the conductive carbon tape that is affixed to the substrates.

In comparison to the DDA-based devices, the OLA-based devices have larger CZTSSe crystals, a higher $\Delta\mu$, better power conversion efficiency and exhibit a more ordered graphitic carbon within the absorber layer. However, both sets of nanoparticles have nearly identical sizes, crystal structures and stoichiometries prior to annealing. In addition, the annealed absorber layers have nearly identical stoichiometries after annealing, indicating that the variation in device performance between the OLA and DDA based films cannot be entirely attributed to stoichiometric variations. Further FTIR, Raman, SEM, and annealing experiments showed that this graphitic carbon is composed of pyrolized aliphatic ligands, which produce a disordered graphitic carbon material that is electrically conductive and that reacts with the chalcogens to produce moieteies doped with thiophenes and selenophenes.[47] The FTIR data shown in **Figure 2.10** shows a clear graphitic resonance mode as well as thiophene and selenophene resonances.[47]

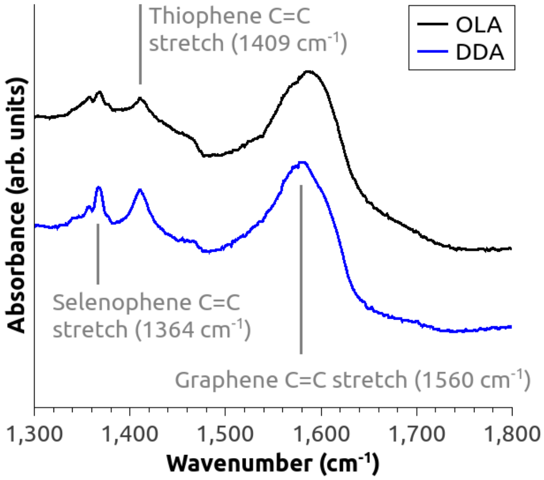

Figure 2.10: FTIR spectroscopy for the graphitic carbon produced using only the ligands and chalcogens and obtained using the ATR technique.[47] The spectra show graphene resonance modes as well as resonance modes from heterocyclic moieties.[47]

2.4 Conclusions and Theorization

Therefore, it can be concluded that the graphitic carbon plays an important role in influencing grain growth during the annealing/selenization step, which explains the differences in device performance and morphology. Specifically, since it has been shown that OLA molecules will react with chalcogens at the double bond to produce a high molecular weight network copolymer, it is likely that the OLA molecules can potentially undergo a cross-linking reaction during the nanoparticle synthesis procedure and during the initial portion of the annealing/selenization step, prior to the final pyrolization process.[65] It has been shown that when nanoparticles are combined with a high molecular weight polymer, the nanoparticles can aggregate together and can self-assemble into clusters.[84–88] Accordingly, the double bond present in the OLA ligands could potentially play a role in directing the aggregation and coalescence of the CZTSSe nanoparticles via the formation of an intermediary network polymer, which would lead to the formation of larger crystallites and grains.

In addition, since the OLA ligands produce a more ordered material, then this graphitic carbon may phase-separate more readily from the CZTSSe crystals, due to a minimization of interfacial surface energy. In addition, this process can also possibly be attributed to the minimization of the Gibbs free energy, where producing graphitic carbon from OLA ligands (which possess a more reactive double bond) is more energetically favorable than producing graphitic carbon from DDA ligands. This mechanism could also potentially serve to explain the larger CZTSSe crystals in the OLA based system; where phase separation drives nanoparticle aggregation, coalescence and grain growth.[82,89] The formation of graphitic carbon that phase separates from the nanocrystals is supported by reports in the literature and by the data and images presented in Figure 2.9, where the OLA based sample produces a distinct carbon-chalcogen rich layer that separates from the larger CZTSSe grains, while the DDA based sample does not produce this layer.[63,64,82]

Accordingly, this work shows that the OLA molecule leads to the formation of a more ordered graphitic carbon that will readily phase separate from the CZTSSe grains, which facilitates grain growth during annealing, leads to the bilayer structure seen in Figure 4.9b, and that reduces the amount of surface-mediated sub bandgap defect states. The DDA based films however, undergo much less phase separation during annealing, have smaller grains with a more disjointed morphology, and a lower $\Delta\mu$ value.

This work demonstrated that aliphatic nanoparticle ligands produce pyrolized graphitic carbon when annealed in an inert atmosphere. When nanoparticles are printed onto a substrate and annealed to produce a sintered photovoltaic material, this graphitic carbon becomes incorporated into the device absorber layer. This graphitic carbon is electrically conductive and also reacts with chalcogens to produce heterocyclic moieties. Furthermore, the molecular structure of the ligand molecules can influence the morphological evolution of the films during annealing via a phase separation mechanism that occurs between the graphitic carbon and the CZTSSe grains. Consequently, this work has helped to elucidate the role of carbon in these devices as has contributed to the foundational knowledge of these materials; where the nature of this graphitic carbon plays a much more important role in determining device active layer morphology and photovoltaic performance than previously thought. This work illustrates how sintered-nanocrystal based devices are actually composed of a morphologically complex hybrid organic-inorganic material that likely forms in part via an intermediary cross-linked network polymer consisting of ligands linked at the double bond by chalcogen atoms. In regards to the broader context of this work and in reference to the other components of the research described herein, it has also helped establish a theoretical framework where nanoparticles can be combined with a polymer during annealing to produce printed chalcogenide materials.

Chapter 3. Developing a New Nanoparticle Synthesis Method With a Unique Sulfur Copolymer

3.1 Introduction

Based on the knowledge gained from the results of Chapter 2, the next phase of this work focused on developing a novel method for synthesizing metal-sulfide nanoparticles without conventional aliphatic ligands by implementing a unique sulfur copolymer. It was previously discovered that the increased reactivity of the OLA double bond leads to improved device performance. This is perhaps due to the formation of an intermediary network polymer that helps drive nanoparticle aggregation and coalescence, where the OLA double bonds are cross-linked with chalcogen atoms. The unique nanoparticle synthesis method described in this chapter was developed in order to mirror some of the advantages of the OLA ligands within the context of a new synthesis paradigm; where the presence of a chalcogen polymer can also potentially lead to improved device performances without the additional detrimental effects of the conventional ligands. These nanoparticles can then be subsequently used to circumvent some of the issues that were discovered in Chapter 2 while concurrently inventing a new method to mirror some of the advantages of the OLA system.

Some initial studies showed that sulfur polymers can be synthesized by cross-linking elemental sulfur chains with divinylic molecules, which can then be used to produce electrochemical devices.[90,91] These studies have subsequently helped establish a new field of sulfur polymer research. However, prior to the work described in this chapter, these types of polymers had not been used to directly synthesize semiconductor nanoparticles, nor had these materials been widely studied for photonic applications. This work resulted in the development of a novel sulfur copolymer that operates concurrently as the sulfur source and high boiling point solvent in a CdS nanoparticle synthesis.

3.2 Sulfur Polymer Background

Elemental sulfur is produced in vast quantities as a byproduct of petroleum refining, since many fossil fuels are rich in sulfur, which must be removed to produce various fuel sources.[92] Although elemental sulfur is used in a myriad of different chemical processes, the supply greatly outpaces the demand, so large quantities of elemental sulfur are stored at various processing sites around the world.[92] In **Figure 3.1**, an exposed deposit of elemental sulfur is seen stockpiled at a petroleum refining site near Vancouver, BC. Stockpiling elemental sulfur poses a number of environmental risks, including ecosystem destabilization via bioaccumulation and contributions to acid rain issues if the sulfur is not properly sequestered.[92,93] Therefore, developing new ways to use elemental sulfur leverages a cheap and readily abundant waste material, and also helps mitigate the environmental impacts associated with its accumulation.

Elemental sulfur has a number of properties that can be utilized as starting points for the development of new materials. One interesting feature is that as elemental sulfur is heated to around 150 ºC, it transitions from an S_8 structured ring to a liquid linearly structured sulfur

Figure 3.1: Excess waste sulfur at a petroleum refining site. Photograph taken by Lauren Kang in Vancouver, BC on 10/17/2015.

diradical, as outlined in **Figure 3.2a**.[94] If the liquid sulfur is heated further, the sulfur diradicals will react with each other and polymerize, producing a solid material.[94] **Figure 3.2b** further illustrates this polymerization process, where an inverted vial containing heated sulfur shows that the polymer has solidified and as the polymer cools, it transitions back to the liquid state. This process is reversible, where the solid sulfur polymer can be cooled to induce depolymerization and the formation of a liquid, which can be further cooled to form S_8 rings.

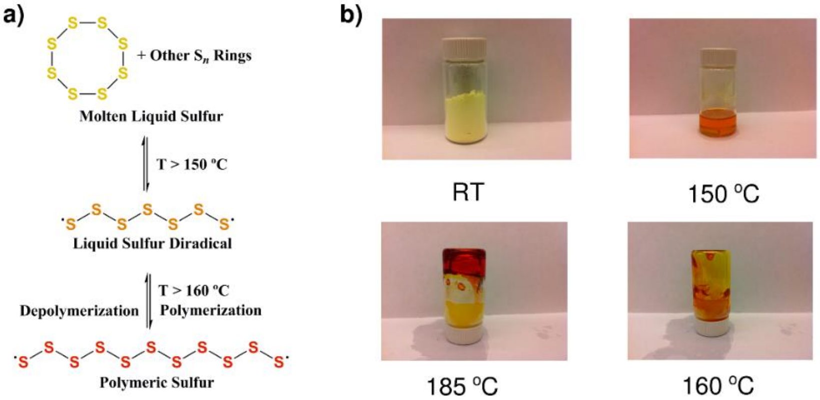

Figure 3.2: a) Elemental sulfur transitions to a liquid diradical state once heated to around 150 °C. Further heating beyond 160 °C will cause the sulfur diradical chains to polymerize, producing a solid polymeric material. b) Images of sulfur diradical polymerization process, where the sulfur is heated from room temperature (RT) and cooled.

Using this free radical polymerization of sulfur as a starting point, Chung *et al*. showed that divinylic monomers such as 1,3-diisopropenylbenzene (DIB) can be added to the sulfur radical solution to produce a copolymer.[94] Specifically, the vinyl group of the monomer reacts with the sulfur radicals to produce a cross-linked, high molecular weight network copolymer.[94] The reaction scheme for the DIB based copolymer is presented in **Scheme 3.1**. This copolymer can be used to produce microstructured materials as well as electrochemical devices.[90,94] A separate study by Chung *et al*. showed that elemental sulfur can be heated and combined with a metal precursor to produce gold nanoparticles. They found that a similar cross-linking organic monomer, 1,4-divinylbenzene (DVB), can be added afterwards to produce a polymeric sulfur and gold nanoparticle composite.[95] Kim *et al*. examined how OLA will undergo a cross-linking reaction

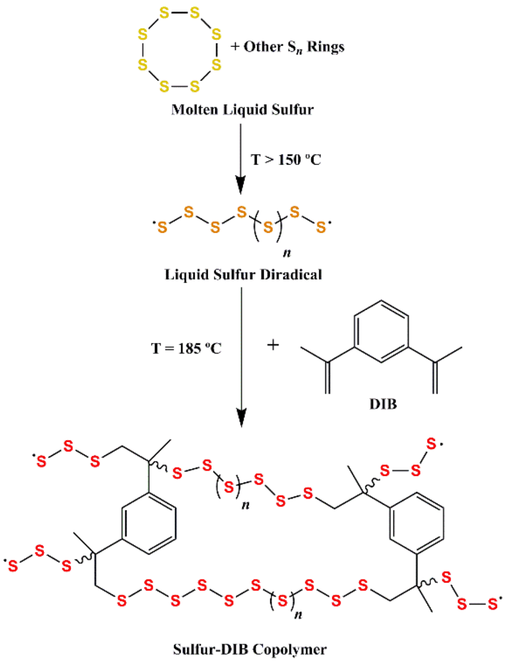

Scheme 3.1: Reaction scheme for producing sulfur and DIB copolymer, where the DIB monomer is injected into the liquid sulfur and the mixture is heated to 185 °C, producing a network copolymer.[94]

with elemental sulfur to produce a copolymer and composite material.[65] However, this study is based upon conventional nanoparticle synthesis methods, and consequently uses organic coordinating ligands and organic solvents. Related studies have examined polymeric sulfur as a high refractive index material,[96] potential nanostructured photocatalyst,[97] and as a medium for lithium sulfur batteries.[90,98] Moreover, recent studies have utilized π-conjugated moieties to create an electrically conductive sulfur copolymer.[99] Although these studies have provided a promising foundation for using elemental sulfur to produce polymeric and nanostructured materials, sulfur copolymers have not been previously used to directly synthesize semiconducting nanoparticles, nor have these polymers been previously used for photovoltaics applications.

3.3 Methods

3.3.1 Sulfur Co-polymer Synthesis

All chemicals were purchased from Sigma Aldrich and used as received. The procedure for synthesizing the methylstyrene based sulfur copolymer is outlined in **Figure 3.3** and the reaction scheme is present in **Scheme 3.2**[100]. Specifically, elemental sulfur (4 g, 124.8 mmol, S8, 99.5%), was placed in a 20 mL glass vial with a stir bar. The glass vial was capped with a septum and suspended in an oil bath. A needle connected to a Schlenk line was inserted through the septum to provide a nitrogen atmosphere for the synthesis. The mixture was then heated to 150 ºC with stirring, and once all of the sulfur reached the liquid state, α-methylstyrene (330 μL, 2.5 mmol, 99%, 50:1 molar ratio of Sulfur atoms to monomer molecules) was injected into the solution through the septum. After injection, the solution was heated to 185 ºC for 10 min. At this stage, the liquid polymer underwent a color change as the polymerization process occurred. The polymer was then cooled to room temperature (RT), producing a solid material.

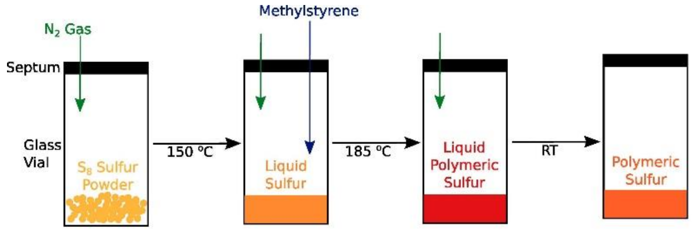

Figure 3.3: Procedure for synthesizing the sulfur copolymer. Oligomeric liquid sulfur diradicals are reacted with a methylstyrene monomer to produce the sulfur copolymer.[100]

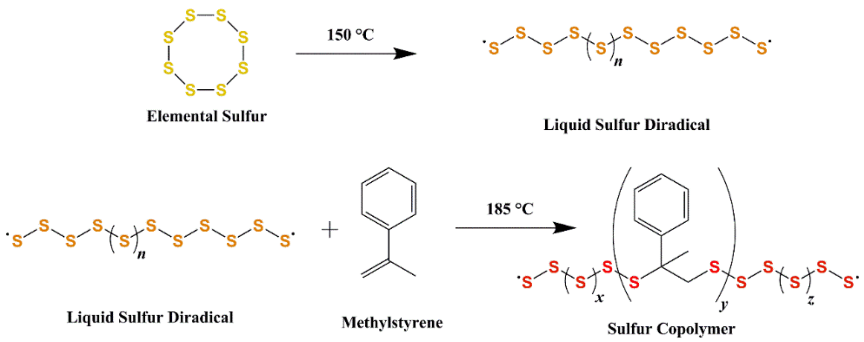

Scheme 3.2: Reaction scheme for producing sulfur copolymer.[100]

3.3.2 CdS Nanoparticle Synthesis Using Sulfur Copolymer

The procedure for synthesizing the CdS nanoparticles using the methylstyrene based sulfur copolymer is outlined in **Figure 3.4**.[100] Specifically, sulfur copolymer (4.0 g, 116 mmol) was combined with cadmium acetylacetonate (Cd(acac), 900 mg, 2.9 mmol 99.9%), in a three neck flask. The flask was subjected to several vacuum and nitrogen pump purge cycles. The flask was then filled with nitrogen and heated to 200 ºC for 30 min with stirring after which the reaction mixture was cooled to RT. This synthesis technique produces a nanocomposite where the CdS nanoparticles are suspended within the excess sulfur copolymer.

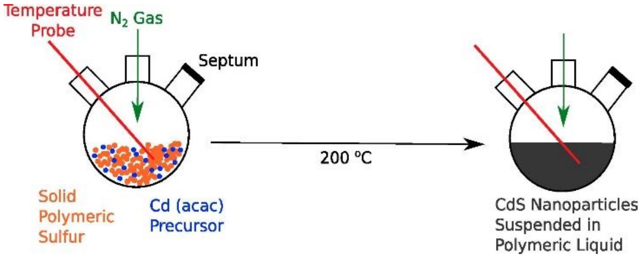

Figure 3.4: Prodecure for synthesizing CdS nanoparticles using a sulfur copolymer.[100]

3.3.3 Removing the Sulfur Copolymer

The nanocomposite powder (200 mg) was dissolved in chloroform (20 mL) and ultrasonicated for 1 h. Chloroform (20 mL) was added to the solution, which was then separated into two 20 mL centrifuge tubes and centrifuged at 10k rpm for 15 min. The sulfur copolymer was then decanted from the settled nanoparticles. The nanoparticles were dispersed in chloroform and sonicated for 15 min, followed by another centrifugation step. This process was repeated until all of the orange colored sulfur copolymer was removed (4-5 repeats) (**Figure 3.5**).[100] The final CdS nanoparticles were placed under high vacuum to remove all of the residual solvent (12.9 mg, 75% yield).

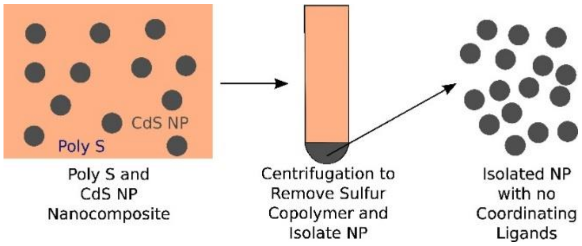

Figure 3.5: Procedure for removing sulfur copolymer and isolating CdS nanoparticles.

3.3.4 Proton Nuclear Magnetic Resonance Spectroscopy

Each spectrum was collected using 99.8% deuterated chloroform as a solvent. The ^1H NMR data were collected using a Bruker AV300 system operating at a frequency of 300.13 MHz with a Bruker BBI probe.

3.3.5 Standard Ligated CdS Nanoparticle Synthesis

Cadmium oxide (CdO, 99.5%), oleic acid (90%), octadecylamine (ODA, 95%), and elemental sulfur (S_8, 99.5%), and 1-octadecene (ODE, 95%, GC) were purchased from Sigma-Aldrich. All chemicals and reagents were used as received. Briefly, CdS nanocrystals were synthesized according to a modified version of the CdO/amine synthesis of Yu and Peng.[101] In a typical reaction, CdO (0.077 g, 600 μmol) was heated with oleic acid (1.696 g, 6 mmol) in ODE (2 g, 7.92 mmol) in a N_2 purged three neck flask to 200 °C until the solution turned clear, indicating the formation of Cd-Oleate. The solution was then allowed to cool to room temperature and ODA (0.75 g, 2.78 mmol) was added before increasing the temperature to 280 °C, and a solution of S_8 (0.0096 g, 300 μmol) in ODE (0.5 g, 1.98 mmol) was swiftly injected into the reaction mixture and the nanocrystals were grown at 260 °C for 10 min before removing from heat and allowing to cool to room temperature. The CdS nanocrystals were then extracted in hexanes and washed with methanol three times before being dried by rotary evaporation. The dry CdS was then washed three times with acetone to remove any remaining impurities, followed by drying under vacuum. Samples were stored in the dark in a glovebox with an N_2 atmosphere.

3.3.6 Absorbance Spectroscopy (UV-Vis-NIR)

The nanoparticles were dispersed in chloroform or formamide and placed in a sealed quartz cuvette. An analogous cuvette filled with chloroform or formamide was used as a reference sample. Optical absorbance measurements were conducted using a Perkin Elmer Lambda 1050 UV-Vis-

NIR spectrometer.

3.3.7 Liquid Photoluminescence Spectroscopy (PL)

The nanoparticles were dispersed in chloroform or formamide and placed in a sealed quartz cuvette. PL measurements were conducted using a Horiba FL3-21tau fluorescence spectrophotometer with an excitation wavelength of 330 nm.

3.3.8 Powder Fourier Transform Infrared Spectroscopy (FTIR)

FTIR spectroscopy for the nanoparticles was conducted using a Bruker Vector 33 instrument. Samples were prepared by mixing 200 mg of KBr with 1 mg of sample powder. The resulting mixture was pressed into a pellet and analyzed by averaging 32 cumulative scans. The data was normalized using the spectrum from a blank KBr pellet.

3.4 Results and Discussion

Using the information and techniques discussed previously as a starting point, this phase of the work focused on proving the utility of this method with a simplified CdS nanoparticle synthesis scheme, before attempting to make more complicated chalcopyrite and kesterite materials. **Figure 3.6a** shows an image of the sulfur copolymer synthesized using the steps outlined in section 3.2.1. Next, this sulfur copolymer was used to grow CdS nanoparticles in solution according to the steps outlined in section 3.3.2. Once cooled, the liquid solidified into a black nanocomposite powder that is easily processed, as depicted in **Figure 3.6b**. In order to

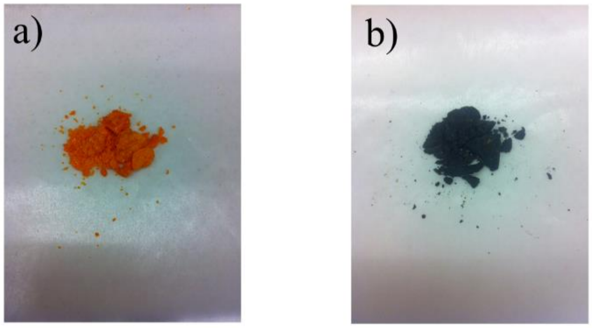

Figure 3.6: a) Image of sulfur copolymer. b) Image of sulfur copolymer and CdS nanoparticle composite powder.[100]

examine the growth of the nanoparticles over time and to determine the extent to which nanoparticle size can be tuned by changing the reaction time, aliquots of the reaction solution were examined using TEM and UV Vis (**Figures 3.7 and 3.8**). The diameters of a population of nanoparticles for each aliquot were measured using the TEM images and were collected to produce

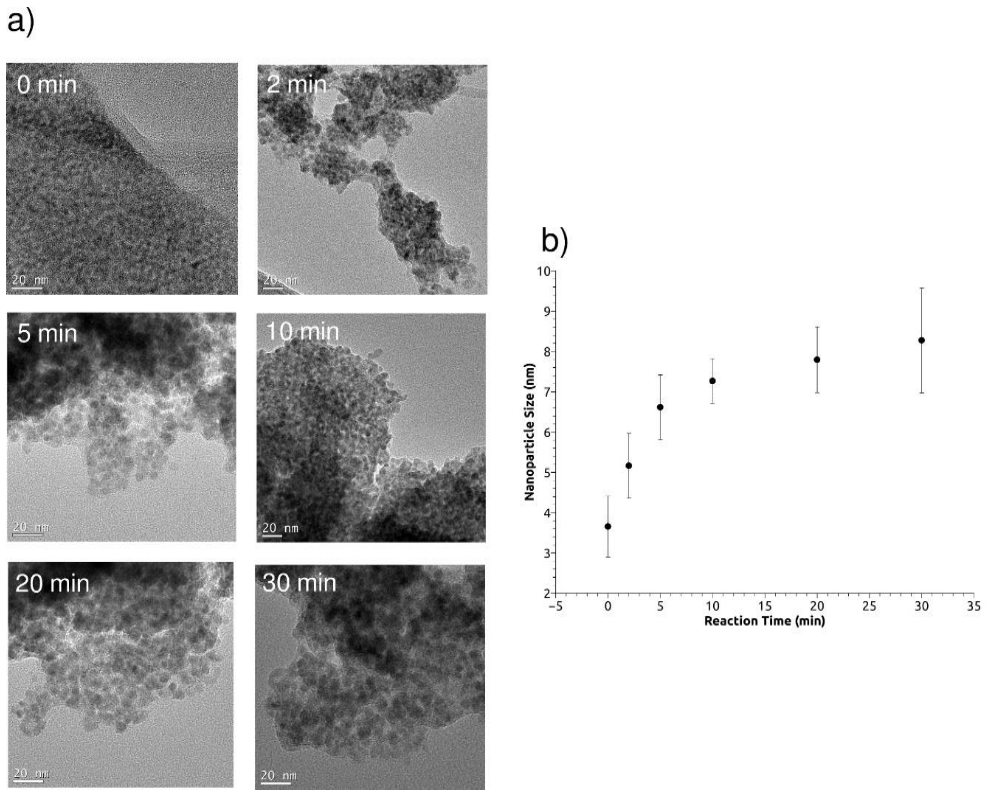

Figure 3.7: a) TEM images depicting nanoparticle growth within the liquid sulfur copolymer. b) Nanoparticle growth profile; the size of the nanoparticles was measured using TEM images.[100]

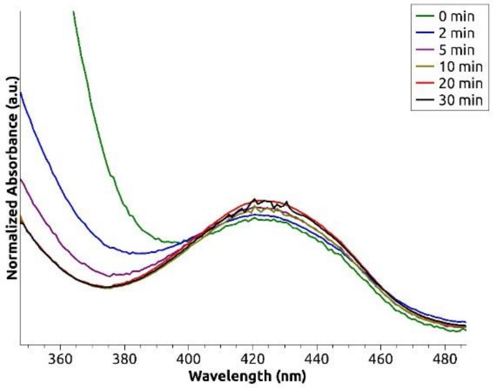

Figure 3.8: UV-Vis spectra illustrating a redshift in absorbance as the CdS nanoparticles grow within the sulfur copolymer matrix.[100]

the data in Figure 3.7b. The images and the data in Figures 3.7 and 3.8 show a typical nanoparticle growth scheme, where an initially more rapid nucleation phase with a smaller size size distribution is followed by a slower growth phase with a larger size distribution. Since only some of the sulfur is consumed by the cadmium precursor, this synthesis produces CdS nanoparticles that are suspended within a sulfur polymer matrix. Next, the CdS nanoparticles were separated from the sulfur copolymer, as described in section 3.3.3. In a manner consistent with that reported by Chung *et al.*,[95] a procedure was attempted with elemental sulfur instead of the sulfur copolymer to check if the polymeric material was indeed required for a nanoparticle synthesis. The elemental sulfur procedure resulted in the production of a viscous paste that was not a liquid during synthesis, that once cooled became a very hard brown material that cannot be easily processed or used to synthesize viable CdS nanoparticles. Moreover, a metal-sulfide nanoparticle synthesis cannot be easily completed with a divinylic cross-linking monomer such as DIB in the sulfur source, since this monomer produces a highly viscous material due to the high molecular weight polymers produced and the cross-linking reactions taking place.[94] In contrast, once heated, the single vinylic group of the methylstyrene based sulfur copolymer promotes depolymerization and the formation of oligomeric radicals that cause the solution to remain a liquid at elevated temperatures and can subsequently react with the metal precursors.

TEM was used to image the resulting CdS nanoparticles in **Figure 3.9**, which show nanocrystals with a diameter of 7-10 nm that aggregate together once some of the copolymer is removed and the solvent has evaporated. The TEM image in Figure 3.9b shows a magnified image of the highlighted region in figure 3.9a and exhibits a clear crystal plane spacing of 3.3 Å, which is consistent with the (111) plane of zincblende CdS or the (002) plane of wurtzite CdS. **Figure 3.9c** shows the selected area electron diffraction pattern (SAED) for the CdS nanoparticles, which

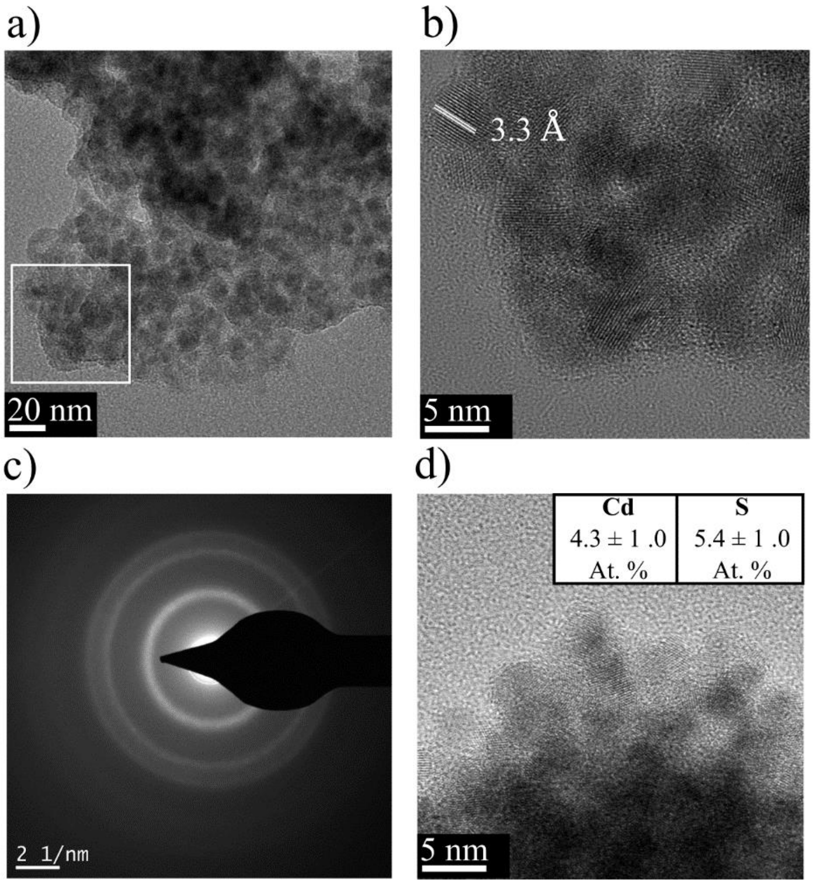

Cd	S
4.3 ± 1 .0 At. %	5.4 ± 1 .0 At. %

Figure 3.9: a) TEM image of CdS nanoparticles with some of the sulfur copolymer removed. b) Magnified TEM image of the highlighted region, showing a clear planar spacing of 3.3 Å. c) SAED pattern for CdS nanoparticle aggregates. d) TEM image of nanoparticle aggregates once the sulfur copolymer has been completely removed with inset EDS data.[100]

shows the presence of polycrystalline aggregates. **Figure 3.9d** shows the CdS nanoparticles once all of the copolymer has been removed and the inset shows the EDS data, where a nearly 1 to 1 ratio of Cd to S atoms is seen, which indicates that the sulfur copolymer has been effectively removed and further confirms the formation of CdS nanoparticles. X-ray diffraction (XRD) was performed to examine the crystal structure of the resulting nanoparticles (**Figure 3.10**). The diffraction pattern is consistent with the SAED pattern in Figure 3.9c and is consistent with the formation of wurtzite and zincblende structured CdS.

Once all of the sulfur copolymer was removed, the nanoparticles were examined with ^{1}H NMR and FTIR for the presence of organic ligands. **Figure 3.11** shows the ^{1}H NMR spectra with

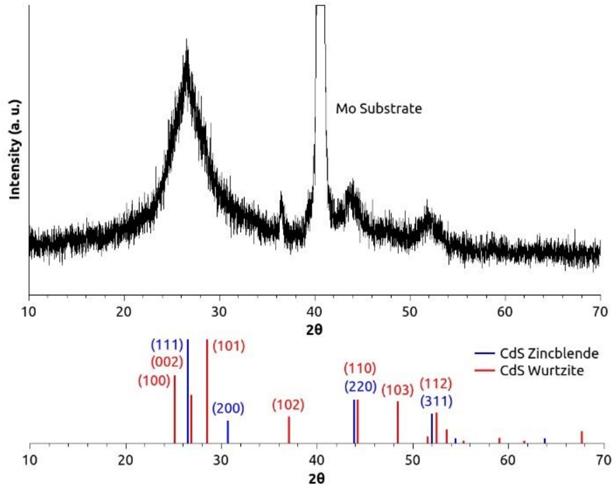

Figure 3.10: XRD pattern for CdS nanoparticles drop-cast onto a molybdenum coated soda lime glass substrate.[100]

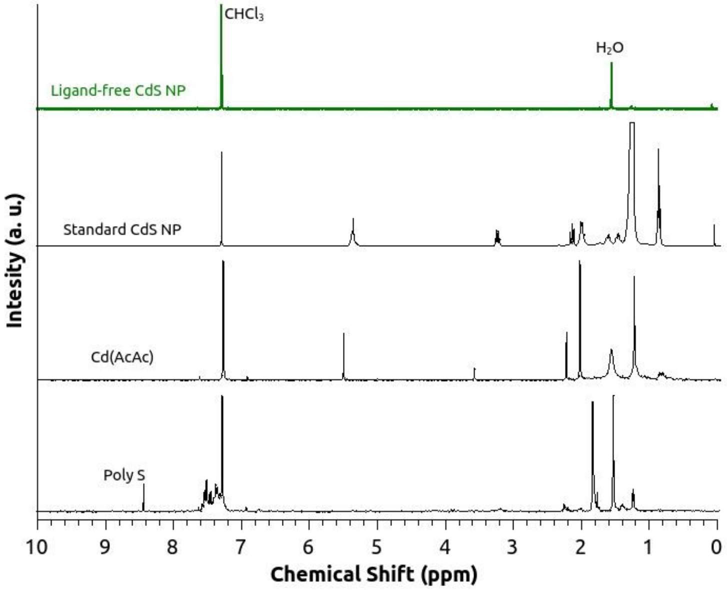

Figure 3.11: ^{1}H NMR spectrum for the ligand-free CdS nanoparticles. Reference spectra for conventional CdS nanoparticles with oleic acid and octadecylamine ligands (Standard CdS NP), the cadmium acetylacetonate precursor (Cd(AcAc)) and the sulfur copolymer (Poly S) are also presented for comparison.[100]

several reference spectra, including standard OLA/oleic acid ligated CdS particles synthesized according to the steps presented in section 3.17. Clearly, the spectra show that the nanoparticles do not possess conventional organic ligands. In addition, the sulfur copolymer NMR does not show any protons coordinating at the methylstyrene vinyl functional group at 5-6 ppm, which supports the sulfur copolymer structure presented in Scheme 3.2. **Figure 3.12** shows the powder FTIR spectra for the same samples, which also show that the nanoparticles do not have conventional organic ligands.

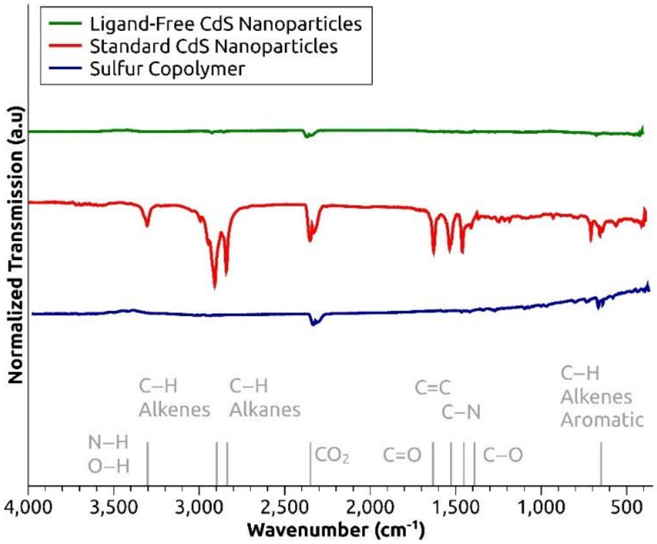

Figure 3.12: FTIR spectra for the ligand-free CdS nanoparticles. Standard CdS nanoparticles capped with oleic acid and octadecylamine, and the sulfur copolymer are also included for comparison.[100]

Next, the CdS nanoparticles were characterized using UV-Vis and PL spectroscopy, to determine the photonic properties of the nanoparticles. **Figure 3.13** shows the absorbance of the particles while they are suspended within the sulfur copolymer matrix (nanocomposite). **Figure 3.14** shows the PL of the nanocomposite and the sulfur copolymer. Since the concentrations of each dispersion are equal for Figures 3.13 and 3.14, the data show that the nanocomposite exhibits an enhanced absorbance onset in comparison to only the sulfur copolymer that is blue-shifted from the bulk bandgap of CdS (510 nm, 2.4 eV). The photoluminescence data presented in Figure 4.19 show that the nanocomposite exhibits a broad peak that is also blue-shifted from the bulk bandgap of CdS, while the sulfur copolymer peak is comparatively small. The broad, blue-shifted nature of the PL spectra is likely due to quantum confinement effects that arise in CdS particles in the 2-5 nm size range, coupled with a relatively high level of nanoparticle size dispersity as seen in the

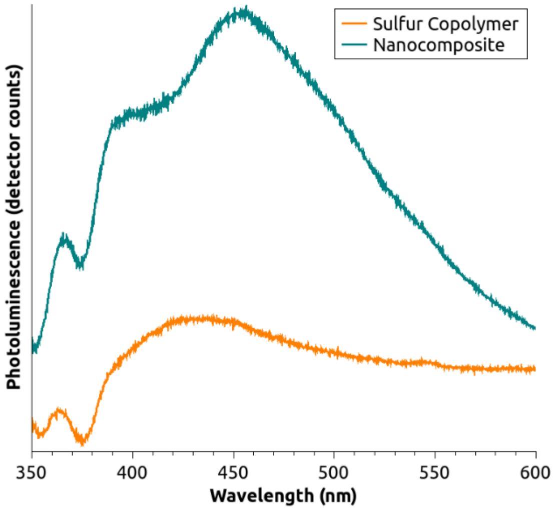

Figure 3.13: Photoluminescence spectroscopy for sulfur copolymer and nanocomposite. The nanocomposite exhibits a peak that is blue-shifted from the bulk bandgap of CdS (510 nm, 2.4 eV), while the sulfur copolymer exhibits comparatively little photoluminescence.

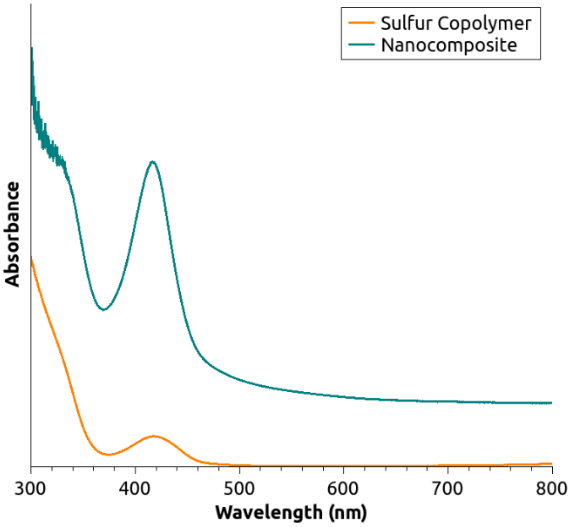

Figure 3.14: Absorbance spectroscopy for sulfur copolymer and nanocomposite**.** The nanocomposite exhibits a significantly enhanced absorption peak in comparison to the sulfur copolymer alone. Both materials have equal concentrations while in dispersion.

TEM images, as well as the presence of surface-mediated sub-bandgap energy states.[102–105]

The isolated nanoparticles were also examined using UV-Vis and PL spectroscopy once the sulfur copolymer was removed. **Figure 3.15** shows both the UV-Vis and PL data. In Figure 3.15, the nanoparticles have a broad PL peak that is centred at the bulk bandgap of CdS and a correspondingly broad absorption spectrum with a small absorption edge that is in the range of

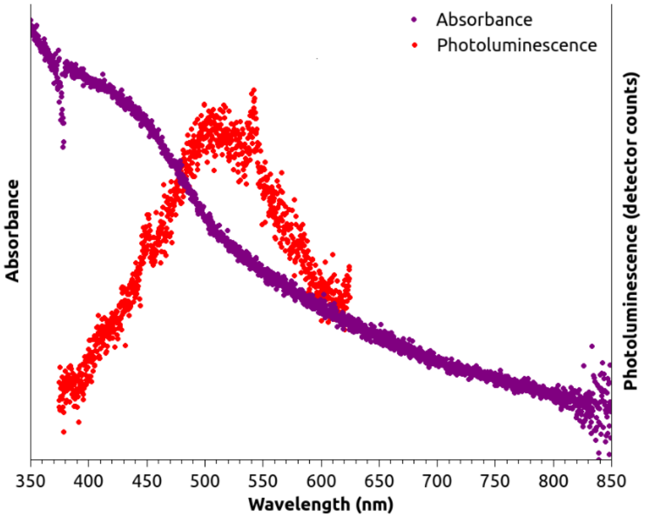

Figure 3.15: Absorbance and Photoluminescence spectroscopy of ligand-free CdS nanoparticles. The PL data show a broad peak centered at 510 nm. The UV-Vis-NIR data show a broad absorption curve with a weak absorption shoulder in the range of 450-550 nm.[100]

450-550 nm. Once the sulfur polymer is removed, the nanoparticle surface is no longer passivated and contains surface defects due to the presence of dangling bonds. This leads to the presence of new surface-mediated energy states that subsequently broaden and red-shift the PL and absorbance spectra in comparison to the spectra presented in Figures 3.13 and 3.14 for the nanocomposite material.[102–106] Therefore, in conjunction with the ^{1}H NMR and FTIR spectra, these data indicate that these nanoparticles do not have conventional defect passivating organic ligands once the sulfur copolymer is removed.[100] Furthermore, these data show that the sulfur copolymer passivates surface defects prior to its removal. One study by Nag *et. al.* showed that metal-sulfide nanoparticles can be effectively ligated with anionic sulfur species via a ligand exchange reaction.[59] In addition, related studies have shown that nanoparticles can be effectively ligated with chalcogenide surface species, although this process requires using hydrazine, which is a highly toxic and explosive liquid.[33] This work posits that the nanoparticles made using this method have similarly structured chalcogen species on the nanoparticle surface, although in comparison the method described herein is a simple, scalable, and nontoxic way to synthesize nanoparticles without the presence of organic ligands.

3.5 Conclusions

This work established a unique method for utilizing elemental sulfur and presented a novel technique for directly synthesizing nanoparticles without conventional aliphatic ligands. Specifically, the work began by developing a new sulfur copolymer that is simple to synthesize, easily processable and is a liquid at elevated temperatures. This sulfur copolymer can be used as a high boiling point solvent and as a sulfur precursor to synthesize stabilized metal-sulfide nanoparticles that are suspended within a sulfur copolymer matrix. Once the ligand-free nanoparticles are ready to be used, they can be separated from the sulfur copolymer. This nascent ligand-free nanoparticle synthesis method can potentially be useful in a range of situations including future biomedical and photonic materials applications, where the presence of aliphatic coordinating ligands is otherwise detrimental.

Chapter 4. Making Photovoltaic Materials

4.1 Introduction

Once the new sulfur polymer and nanoparticle synthesis method were invented and proven for the CdS system, the next step of this project focused on using these discoveries to produce PV materials. Specifically, the chalcopyrite CISSe was chosen as a next step due to its reduced complexity in comparison to CIGSSe and CZTSSe. CISSe benefits from comparatively simplified crystallographic, stoichiometric, and defect chemistry properties due to the reduction in elemental constituents. Accordingly, the goal of this stage of the research was to transition from synthesizing simple binary metal-chalcogenides to more complicated PV materials.

4.2 Methods

4.2.1 CIS Nanoparticles from a Sulfur Copolymer

CIS nanoparticles were synthesized in a manner similar to what was outlined in sections 3.3.1-3.3.3. Specifically, a batch of sulfur copolymer was synthesized using the methods outlined in section 3.3.1 (4.0 g). Next, copper (I) acetate (Cu(ac), 202 mg, 1.65 mmol 97.0%) and indium (III) acetate (In(ac), 482 mg, 1.65 mmol 99.9%) were added to a three-neck flask on top of the sulfur copolymer. The flask was purged with vacuum and dry nitrogen several times. Next, the flask was heated to 200 °C and the metal precursors subsequently mixed with the liquid sulfur copolymer. The nanoparticles were allowed to grow for 30 min before the flask was cooled to room temperature. Next, the nanoparticles were removed from the sulfur copolymer using the methods detailed in section 3.3.3.

4.2.2 Printing PV absorber films using CIS Nanoparticles from Sulfur Copolymer

Isolated CIS nanoparticles were dispersed in formamide (200 mg/mL) and were sonicated for 30 min to ensure dispersion. This nanoparticle ink was then pipetted onto a cleaned Mo coated

SLG substrate in 7 µL increments. The ink was printed onto the substrate using a doctor-blade printing technique with a 125 µm thick spacer and was then rapidly dried on a hot plate set at 300 °C in a fume hood for 10 s. Next, these printed thin films were annealed and selenized concurrently, in accordance with the methods used in the CZTS study and outlined in section 2.2.4.

4.3 Results and Discussion

4.3.1 Large CIS Nanoparticles

Figure 4.1 shows the TEM images of the resulting nanoparticles. It is important to note that the metal precursors used were acetates, instead of acetylacetonates, as was used in the CdS synthesis. A precursor with a smaller counter ion was chosen in an effort to try to increase the reactivity of the precursors by choosing a smaller molecule. With a more reactive precursor, the nanoparticles will grow to a larger size, as is clearly seen in the TEM images in Figure 4.1. If

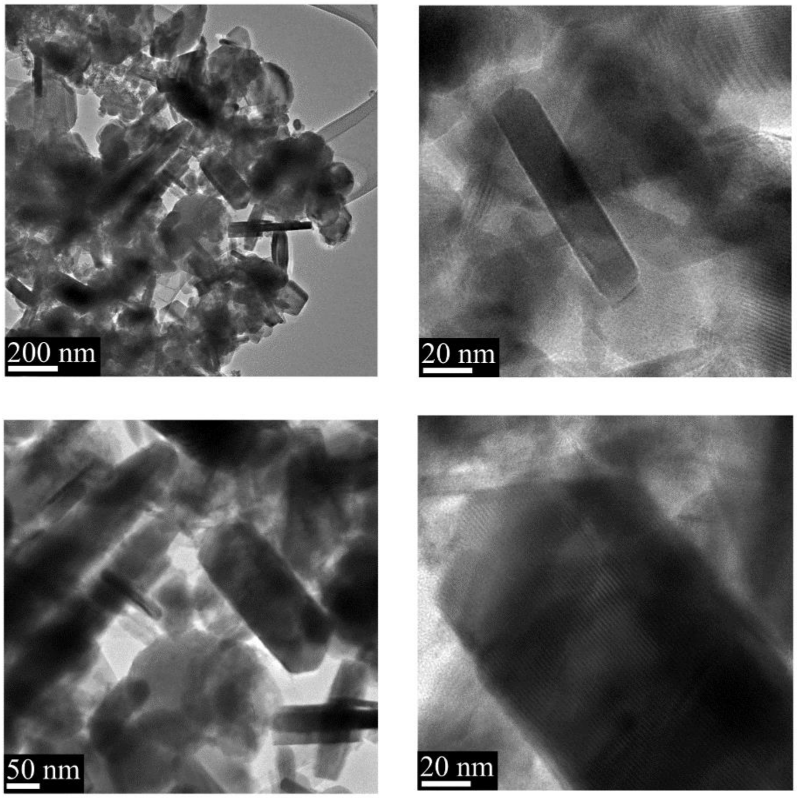

Figure 4.1: TEM images of CIS nanoparticles synthesized using the sulfur copolymer. The nanoparticles exhibit a multifarious platelet structure in the 100 nm size range.

larger, more crystalline nanoparticles can be grown in solution, then this will help facilitate the formation of a more crystallographically ordered thin-film material.

The nanoparticles were next printed onto Mo coated SLG substrates and analysed with XRD (**Figure 4.2**) using the methods presented in section 4.2.2, except without the annealing step. From the diffraction pattern, it is clear that the nanoparticles exhibit several different crystal structures. Although it is difficult to deconvolute these spectra, there are several peaks that are well defined and are consistent with the formation of Cu_2S, $CuInS_2$, and In_2S_3. Therefore, although several phases are present, some CIS formation does occur and the metals remain in the proper oxidation states (Cu^{1+} and In^{3+}).

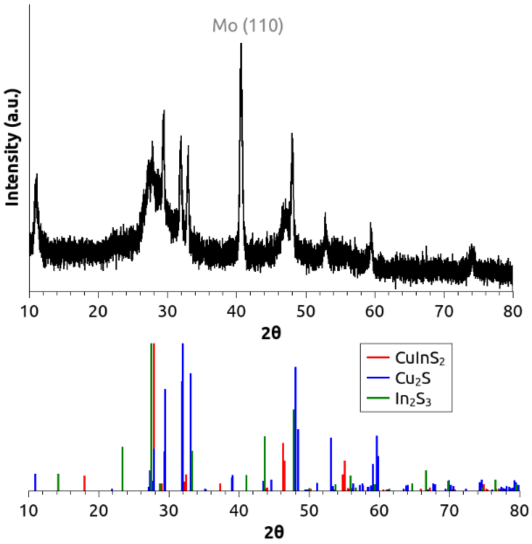

Figure 4.2: XRD spectra of CIS nanoparticle film synthesized using the sulfur copolymer prior to annealing.

Next, these thin films were annealed and selenized in a manner that is analogous to the procedure that was implemented in the previously discussed CZTS work and that is outlined in section 4.2.2. An XRD spectrum was acquired post annealing and is presented in **Figure 4.3**. Encouragingly, the nanoparticles transition to the $CuInSe_2$ structure and exhibit extremely sharp

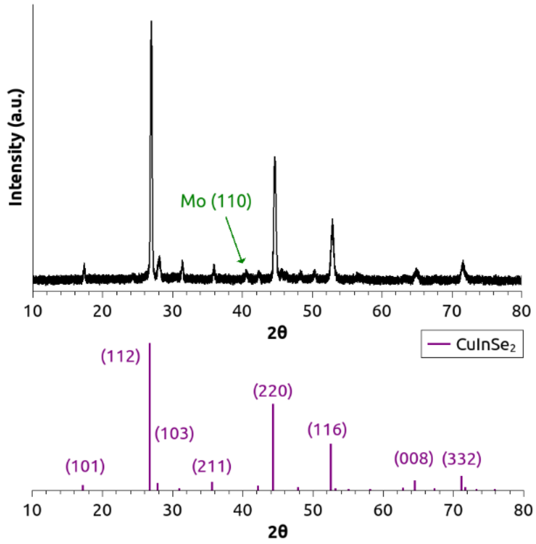

Figure 4.3: XRD diffraction pattern of CISSe film post annealing/selenization made from sulfur copolymer based CIS nanoparticles.

peaks that are indicative of a high level of crystallinity, where the crystallite size is beyond the range of the Scherrer equation and is within the 100 nm order of magnitude range. In order to further probe the crystal structure of this material, Raman spectroscopy was also performed (**Figure 4.4**) using the methods outlined in section 2.2.7. The Raman spectrum confirms the formation of highly crystalline $CuInSe_2$ but also shows a prominent Cu_2Se subspecies peak.

In order to examine the morphology and stoichiometry of these films, cross sectional SEM

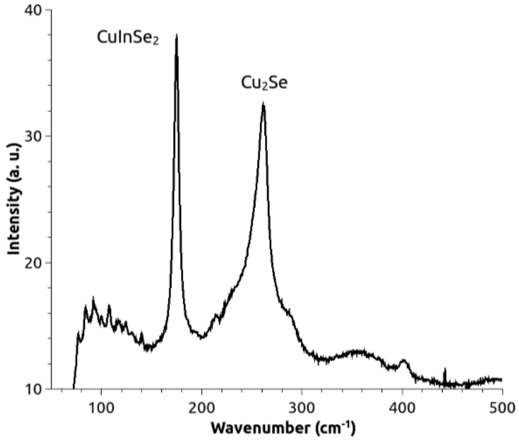

Figure 4.4: Raman spectrum of CISSe film post annealing/selenization made from sulfur copolymer based CIS nanoparticles.

was also performed (**Figure 4.5**). The films exhibit large grains on the micron scale, which is very encouraging and supports the previous evidence that these nanoparticle inks can undergo a high level of crystallization and grain growth; however, the films have a high level of surface roughness and are extremely non-conformal, which is not ideal for PV absorber layers. This is likely due to the large nanocrystals that were grown in solution. Moreover, the films appear to be several microns thick in some locations, which is larger than the ~1 µm optimal thickness for PV applications.

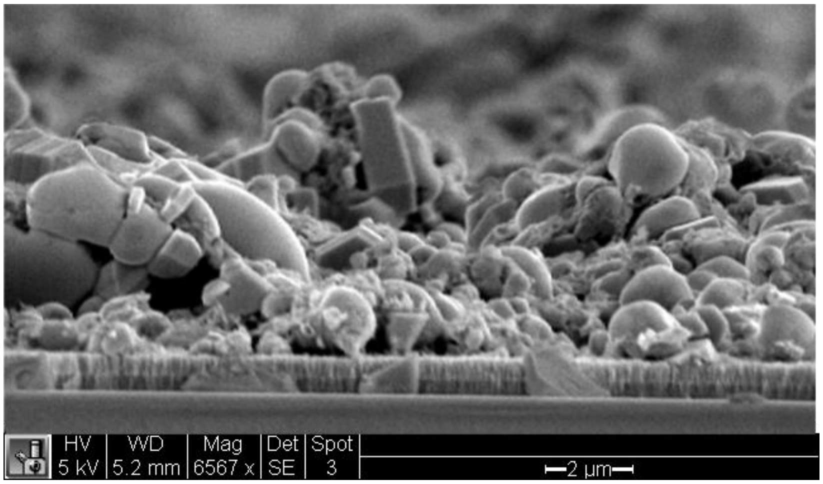

Figure 4.5: Cross sectional SEM image of CISSe films made using CIS nanoparticles synthesized within a sulfur copolymer and annealed at 500 °C in the presence of Se vapor.

To investigate the quality of these films for PV applications, PL spectroscopy was conducted using the methods outlined in section 2.2.7. The PL spectra presented in **Figure 4.6** is centered at approximately 1.0 eV (1240 nm) which is the theoretical bandgap value for a fully selenized $CuInSe_2$ material. This is extremely encouraging, since many printed PV materials exhibit a PL peak that is redshifted from the theoretical value due to the presence of defect states.[70,71] However, the PL intensity of the peak is low, indicating that the photoluminescence quantum yield of the material is diminished.

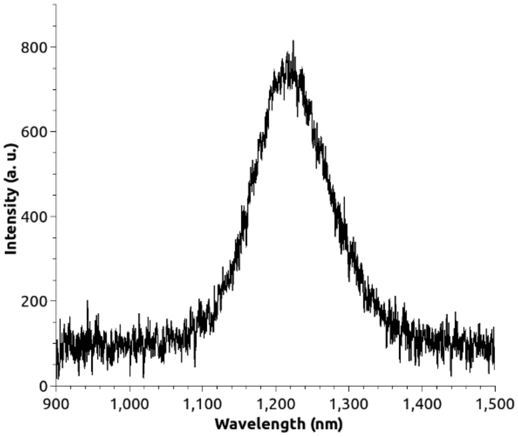

Figure 4.6: PL spectrum of CISe film post annealing/selenization made from sulfur copolymer based CIS nanoparticles.

4.3.2 Small CIS Nanoparticles

In order to further probe the influence of nanoparticle size on thin film morphology and optoelectronic quality, CIS nanoparticles were synthesized using a shorter reaction time (3 min instead of 30 min) to produce smaller particles, in a manner analogous to what was presented in section 4.2.1 and to the previous synthesis methods with respect to all other variables. **Figure 4.7**

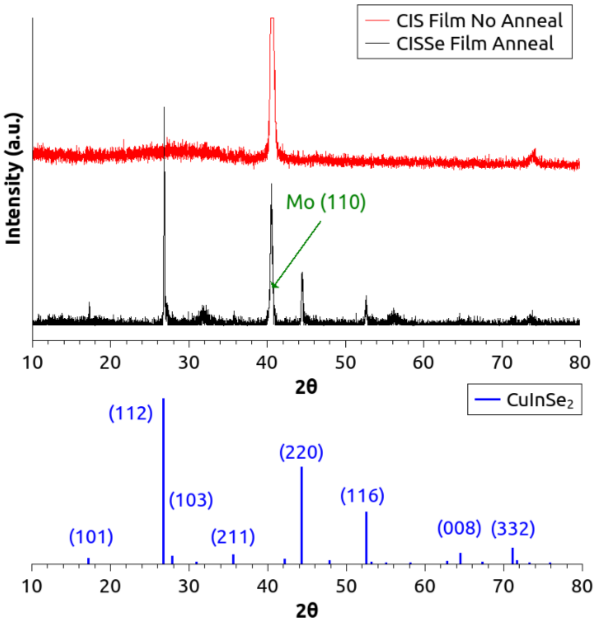

Figure 4.7: XRD diffraction pattern of CISSe film post annealing/selenization and CIS film prior to annealing. Films were made from smaller CIS nanoparticles.

shows XRD spectra of the resulting films before and after annealing. The nanoparticle films only exhibit a very broad diffraction peak in the 20-30 2θ region before annealing, which indicates that the particles are within the 5-10 nm size range. Remarkably, despite the small size of these initial particles, the crystals grow to produce a very sharp CISSe diffraction pattern after annealing (Figure 4.7). This is an extremely encouraging result, since it illustrates how these nanoparticle films are able to undergo substantial crystal growth during annealing. **Figure 4.8** shows the Raman spectra for the annealed/selenized films. The spectra exhibit a prominent $CuInSe_2$ peak, but also a Cu_2Se subspecies peak. In order to gain a further understanding of the morphology and stoichiometry of these films, SEM images and concurrent EDS spectra were collected. **Figure 4.9** shows SEM images of the printed CIS nanoparticle films before and after annealing. **Table 4.1** summarizes the stoichiometry data from the EDS spectra. The images in Figures 4.9a and 4.9b show that the films transition from a high surface area nanostructured material to a film consisting of smooth CISe grains, which is a promising result for producing conformal PV films in the future. In addition, the films exhibit a platelet morphology, which agrees well with the TEM images shown in Figure 4.21, although these particles are smaller due to their reduced reaction time. Once the films are annealed and selenized, the surface roughness of the grains diminishes drastically and

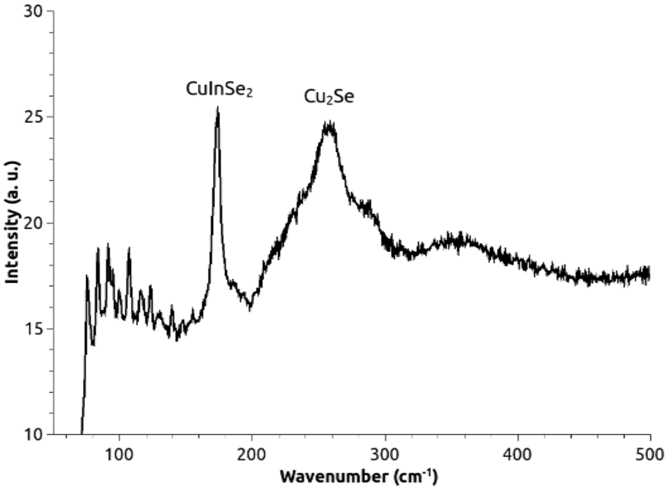

Figure 4.8: Raman spectra of CISSe film post annealing/selenization. Films were made from smaller CIS nanoparticles.

the grains grow to be a much larger size with smooth surfaces. The non-conformal nature of the films however, remains problematic for PV implementation; where discontinuities in the film will lead to shunting pathways and diminished device performance.

It is important to note that for the EDS data, the spectra for the sulfur signal and the molybdenum signal overlap, so it is not possible to decouple these spectra to determine the sulfur stoichiometry accurately. In addition, the selenium stoichiometry is elevated beyond the stoichiometry of the $CuInSe_2$ material that is present, since there is a significant amount of background signal from $MoSe_2$ on the substrate surface and should therefore be treated qualitatively only. Despite these limitations however, the EDS data in Table 4.3 shows that the

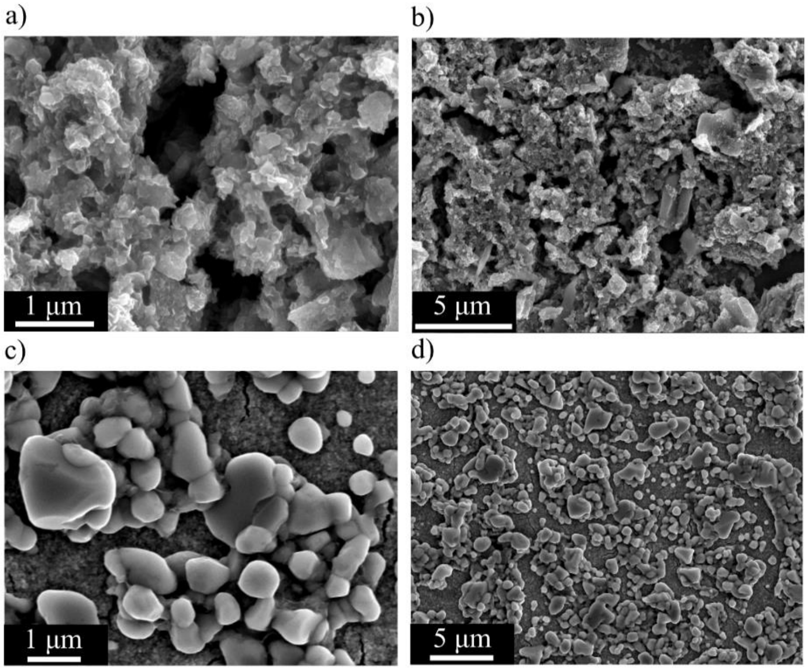

Figure 4.9: a) and b) SEM images of CIS nanoparticle prior to annealing. c) and d) SEM images of CISSe films after annealing/selenization,

Table 4.1: Stoichiometric ratios for pre-annealed and annealed CIS/CISSe Films

Thin Film	Cu/In	Se/(Cu+In)
Pre-annealed	0.99 ± 0.02	N/A
Annealed	1.18 ± 0.19	2.28 ± 0.83

Cu:In ratio is nearly 1:1 prior to annealing, but after annealing the films are slightly Cu rich. Therefore, this data agrees with the Raman data presented in Figure 4.28, which shows the presence of some Cu_2Se resonance modes. These films were subsequently examined with PL spectroscopy, but the signal was completely quenched. Accordingly, it is likely that there is some copper-rich material that quenches the PL. Furthermore, the films that were fabricated using larger CIS particles did show some PL signal; since these films will have proportionally fewer nanoparticle surface interfaces, it is therefore likely that these films have some interfacial copper-rich defects that quench PL. It has been shown that Cu rich defects can be thermodynamically stable and will lead to the formation of sub-bandgap defect states that will quench PL emission.[56,107–109] Moreover, the CdS work showed that the presence of the sulfur copolymer helped passivate surface defects and its removal introduced dangling bonds that broadened and red-shifted photonic properties. Therefore it is likely that in this CIS system, when the sulfur polymer is completely removed, the smaller particles possess a higher population of surface defect states in comparison to the larger CIS particles.

4.4 Conclusions

This work showed that the methods that were developed for the CdS system can be readily extended to make CIS nanoparticles. Furthermore, it was shown that when CIS nanoparticles are synthesized without conventional aliphatic ligands, the films will undergo extraordinary crystal growth to produce highly crystalline CISe. This material produces a PL curve that is not red-shifted from the theoretical 1.0 eV position, indicating promising optoelectronic properties. The extent of this crystallization is well beyond what has been seen for nanoparticles with conventional aliphatic ligands. This is an extremely promising result that helps establish the validity of this technique as a superior method to produce high quality PV materials from nanocrystal inks, due to the favourable crystal formation thermodynamics that can be achieved when the aliphatic ligands are removed from the equation.

The method suffers from some issues with the presence of copper-rich surface species that can quench PL and lead to recombination. However, it is likely that this issue can be fixed by synthesizing inks that are stoichiometrically indium rich at the outset. In addition, when the sulfur copolymer is completely removed, it is likely that some surface defect passivation is lost. Therefore, it may be favourable to retain some amount of polymer to passivate these surface defects. Overall, this work constitutes a promising step towards making PV devices using these techniques.

Chapter 5. Selenium Sulfide Polymer for Low-Temperature, Completely Solution-Processed Chalcogenide Photovoltaics

5.1 Introduction

The work from the previous chapter showed that these new methods can be effectively implemented to produce highly crystalline CISSe materials, with crystal growth properties that are extremely promising in comparison to what is seen for conventionally ligated nanoparticle inks. However, those methods still relied on a high-temperature (500 °C) annealing procedure and a concurrent selenium vapor-phase reaction. The ultimate goal of this work is to develop a method to make low-bandgap chalcogenide materials without high-temperature processing, expensive vapor-phase reaction procedures, or hydrazine (a highly toxic and explosive solvent), which has not been previously achieved.

5.2 Methods

5.2.1 Synthesizing the Selenium Sulfide Terpolymer

Selenium disulfide (SeS_2, 4.0 g, 28.0 mmol) was placed in a three neck flask and combined with α-methylstyrene (910 μL, 6.99 mmol, 99%). The flask was connected to a temperature probe, a condenser, and connected to a Schlenk line. The flask was placed on a heating mantle and was purged several times with vacuum and dry nitrogen. The mixture was heated to 185 °C with stirring for 30 min, to allow the organic monomer to completely react with the selenium sulfide radicals. The organic monomer was refluxed until it completely reacted with the liquid radicals, at which point there was no longer any condensation within the condenser. The ratio of S, Se, and α-methylstyrene yields a random terpolymer with a stoichiometry of 8:4:1 for S:Se: α-methylstyrene as presented in **Scheme 5.1**.

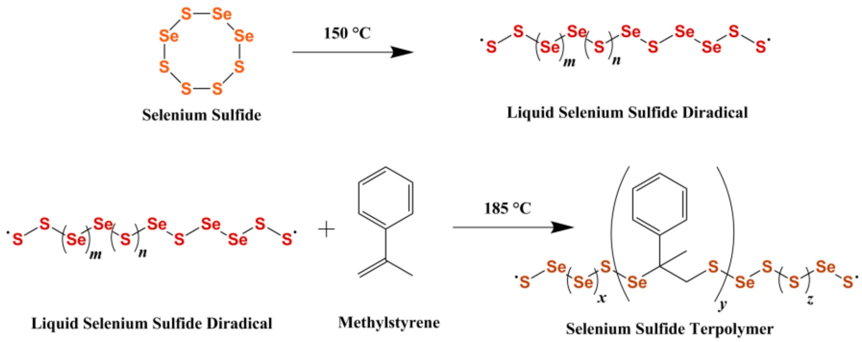

Scheme 5.1: Reaction scheme for producing selenium sulfide terpolymer.

5.2.2 CISSe Nanoparticle Synthesis using Selenium Sulfide Terpolymer

CISSe nanopraticles were synthesized within a terpolymer matrix in a manner analogous to the techniques outlined in section 3.21. The selenium sulfide terpolymer (4.0 g, 83.9 mmol chalcogen atoms) was placed in a three neck flask and copper (I) acetate (Cu(ac), 202 mg, 1.65 mmol 97.0%) and indium (III) acetate (In(ac), 482 mg, 1.65 mmol 99.9%) were added to a three-neck flask on top of the sulfur copolymer. The mixture was heated to 215 °C with stirring and the metal precursors subsequently mixed with the liquid terpolymer. The nanoparticles were allowed to grow for 30 min before the flask was cooled to room temperature. Next, the nanoparticles were removed from the sulfur copolymer using the methods detailed in section 3.3.3.

5.2.3 Printing PV absorber films using CISSe Nanoparticles from Terpolymer

The CISSe nanoparticles were dispersed in anhydrous formamide (100 mg/mL) and were sonicated for 30 min to ensure dispersion. The ink was then transferred to a controlled atmosphere glove box. The ink was pipetted onto cleaned Mo coated SLG substrates in 100 µL increments. Printing was accomplished with a spin coater set at 2k rpm for 30 sec. Once the printing step was finished, the films were immediately placed on a hot plate and heated to 150 °C. This printing and drying cycle was repeated 10 times to produce a nanoparticle thin film. Next, the final films were placed on a hot plate and heated to 250 °C and were annealed for 1 h.

5.3 Results and Discussion

Figure 5.1 shows some TEM images as well as a Fourier transform diffraction pattern for the synthesized CISSe nanoparticles. Figures 5.1a-c show that the CISSe nanoparticles exhibit a platelet morphology and range in size from 10 to 30 nm. In addition, it can be seen that the particles remain suspended within some remaining chalcogen polymer. This can be attributed to the fact that some fraction of the selenium sulfide terpolymer is less soluble than the pure sulfur variant and is consequently more difficult to remove from the nanoparticles via the ultrasonication and centrifugation step. This is evidenced by the fact that the isolated CISSe nanoparticles had a greater mass than was expected if all of the terpolymer had been removed. Furthermore, the selenium sulfide terpolymer is more viscous than the sulfur copolymer and is therefore less likely to be easily solubilized. It is likely that the addition of Se atoms decreases the flexibility of the polymer backbone and/or promotes the formation of some population of polymer chains with a larger mass, both of which would decrease solubility. The patterns seen in Figures 5.1d and 5.1e are consistent

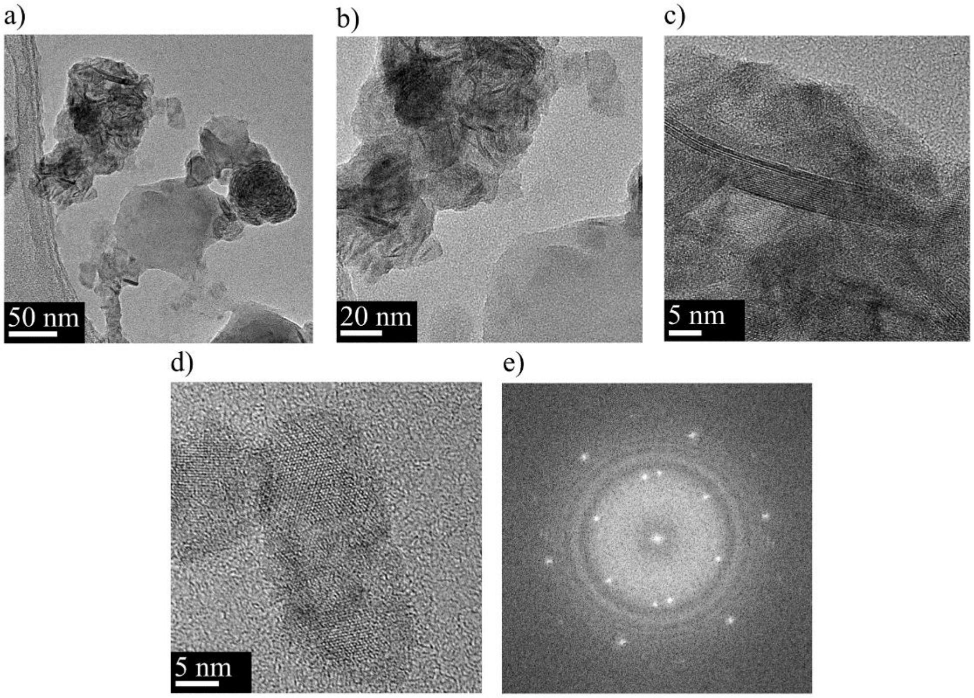

Figure 5.1: a), b), c), and d) TEM images of CISSe nanoparticles synthesized using the selenium sulfide terpolymer. e) Fourier transform of the image presented in d) showing a diffraction pattern consistent with the tetragonal crystal structure of chalcopyrite.

with the formation of a tetragonally structured material, which is indicative of the formation of CISSe. The presence of additional diffraction spots on the diffraction pattern in Figure 5.1e is likely due to the presence of substitution defects within the material, such as the presence of Cu_{In} antisite defects.[110,111]

The CISSe nanoparticles were then printed onto substrates and dried at 250 °C for 5 min and subsequently examined with SEM/EDS to determine the initial film morphology and stoichiometry. **Figure 5.2** shows some representative SEM images of the resulting films as well as several elemental maps obtained via EDS spectroscopy. Figures 5.2a and 5.2b show that the films consist of CISSe particles that remain suspended within the selenium sulfide terpolymer matrix, as opposed to the pre-annealed films shown in Figures 4.9a and 4.9b, where it is evident that all of the sulfur copolymer polymer has been removed. This further confirms the evidence that

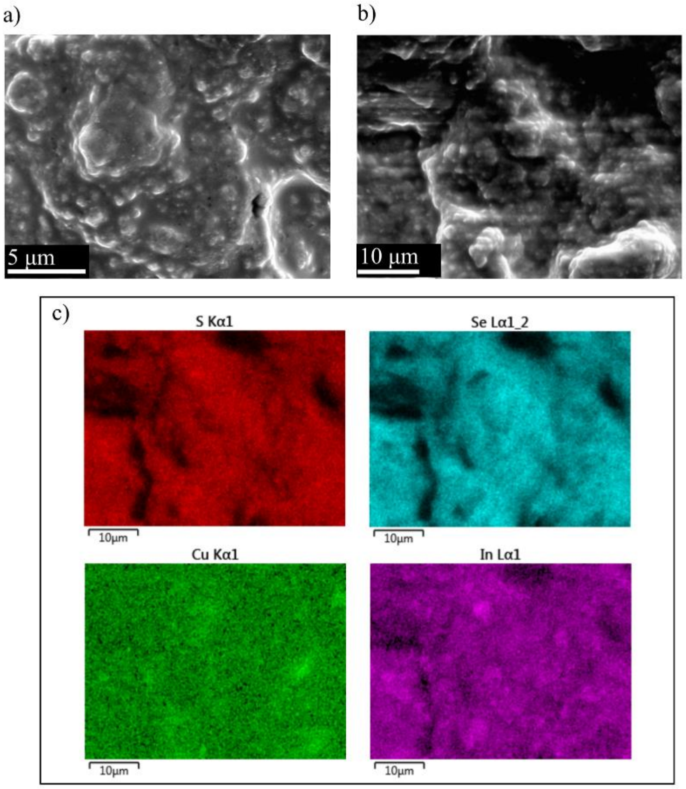

Figure 5.2: a) and b) SEM images of CISSe nanoparticle films with selenium sulfide terpolymer residue prior to annealing. c) Elemental maps from EDS spectra for region shown in b).

the selenium sulfide terpolymer is less soluble and is more difficult to remove. From the elemental maps shown in Figure 5.2c, it can be seen that there are also regions with different stoichiometric ratios of Cu and In. Therefore, it appears as though there are regions with nanoparticle aggregates that are In rich or are Cu rich. The Cu distribution appears to be more uniform, suggesting that there are larger clusters of particles that tend to be In rich versus smaller particles that tend to be more Cu rich. This result agrees well with the previous studies, which indicated the presence of a Cu rich surface material that quenches PL. Moreover, although these films have only been briefly dried at 250 °C for 5 min, it is known that Cu is relatively mobile even at this temperature range, so it is possible that Cu species have begun diffusing within the film after this step, which would lead to the more homogeneous distribution of Cu as seen in Figure 5.2c.[112,113]

Next, these films were annealed at 250 °C for 1 h in a glovebox. **Figure 5.3** shows the XRD diffraction patterns for the films before and after annealing. Remarkably, these films show substantial crystal growth at this low temperature. This result is extremely encouraging and constitutes an important first step in the path towards making low-temperature, completely solution-processed chalcopyrite PV films. The diffraction pattern is consistent with the formation

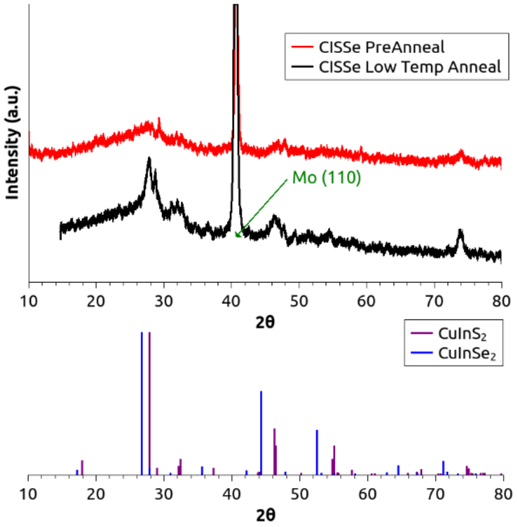

Figure 5.3: XRD patterns for CISSe films before and after 250 °C 1 hr annealing.

of both CIS and CISe. The annealed films were subsequently analysed with Raman spectroscopy (**Figure 5.4**). The Raman spectrum shows a multitude of resonance modes that are consistent with the formation of $CuInSe_2$,[114,115] $CuInS_s$,[114] $CuSe_2$,[116,117] CuS_2,[116] In_2Se_3,[118] In_2S_3,[119] and chalcogen-chalcogen[120] resonance modes.

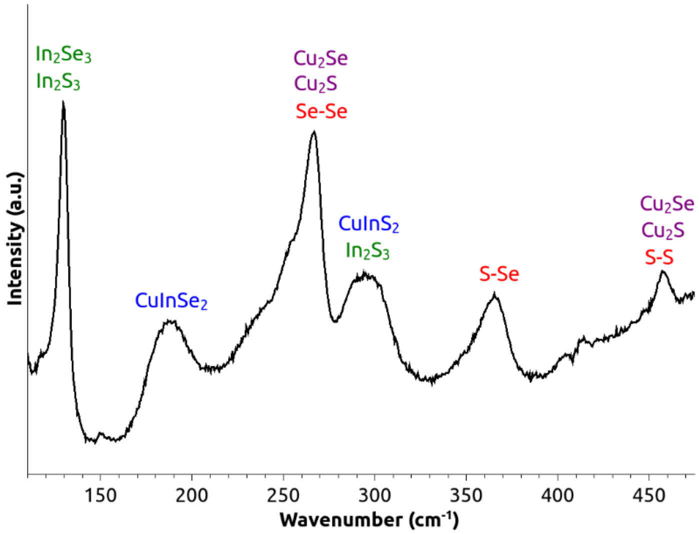

Figure 5.4: Raman spectrum for CISSe nanoparticle films after 1 hour of annealing at 250 °C.

Next, the films were examined with SEM and EDS to characterize the morphology and stoichiometry of the films after annealing. **Figure 5.5** shows the images and elemental maps for the films after the low-temperature annealing procedure. The images and maps show that much of the terpolymer has evaporated. Moreover, similarly to Figure 5.2, the elemental maps show that there are some regions which are Cu rich while others are In rich, which agrees with the Raman spectra. Furthermore, the images show that the particles have undergone some grain growth, with grains in the micron size range. The films are also have relatively improved surface coverage in

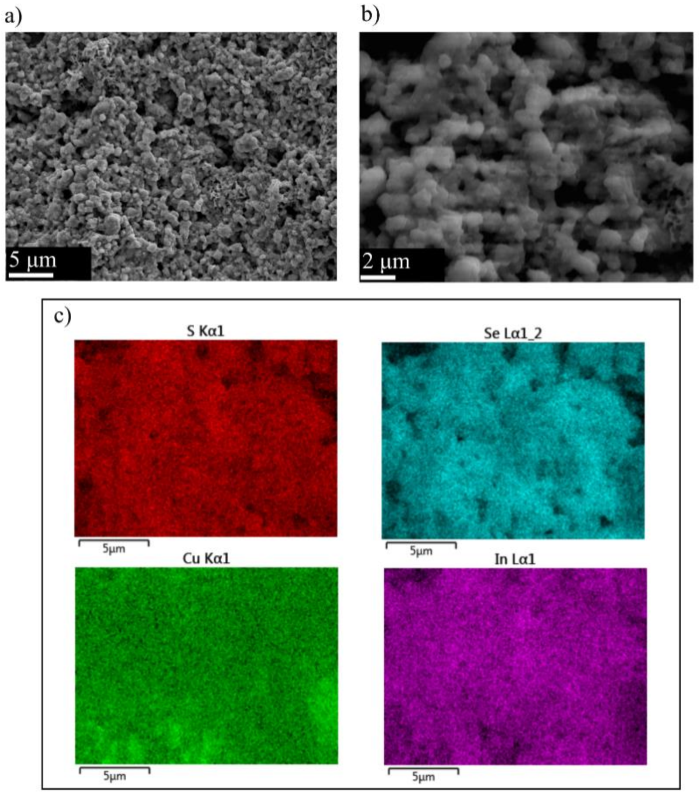

Figure 5.5: a) and b) SEM images of CISSe nanoparticle films with selenium sulfide terpolymer residue after low-temperature annealing. c) Elemental maps from EDS spectra for region shown in b).

comparison to the films shown in Figure 4.9, which is encouraging for PV applications, however these films are in the range of 2-5 µm in thickness, which is thicker than is needed for thin-film absorbers. This extra thickness eliminates the background signals associated with the molybdenum substrates, however future films will require optimization of the printing process. **Table 5.1** summarizes the stoichiometric date for these films from various EDS spectra. The data indicate that some of the selenium sulfide terpolymer remains after this annealing procedure, however

Table 5.1: Stoichiometric ratios for pre-annealed and low-temperature annealed CISSe Films synthesized using the selenium sulfide terpolymer

Thin Film	**Cu/In**	**(Se+S)/(Cu+In)**	**Se/S**
Pre-annealed	1.2 ± 0.1	7.7 ± 2.0	1.6 ± 0.2
Annealed	1.7 ± 0.5	3.0 ± 0.4	2.4± 0.2

much of it has evaporated, which is a very promising result. The data also indicate that the films start out slightly copper rich and become even more copper rich after annealing. In addition, the data show that as the films anneal, the selenium to sulfur ratio increases, indicating relative sulfur loss due to its higher vapor pressure. The data also indicate that as the annealing process proceeds, the terpolymer vaporizes overall (although the rate of sulfur loss is faster than the rate of selenium loss), as indicated by the reduction in the overall chalcogen to metal ratios.

Next, the films were examined with PL spectroscopy in order to gauge the quality of the material for PV applications (**Figure 5.6**). Unfortunately, the Charge-coupled detector (CCD) system that was used has an abrupt reduction in sensitivity beginning at approximately 900 nm and extending into lower wavelengths, which means that the data beyond 900 nm should be considered qualitatively only and that the abrupt drop off seen in the data is likely due to this issue in part. Nevertheless, the spectrum is useful and promising for several reasons. The data show that the material produces a PL spectrum that is situated between the bandgap of $CuInS_2$ and $CuInSe_2$, where a material that has a mixture of chalcogenides will undergo a change in the bandgap as the relative stoichiometric ratio of the chalcogens is changed. Therefore, this material has a solid

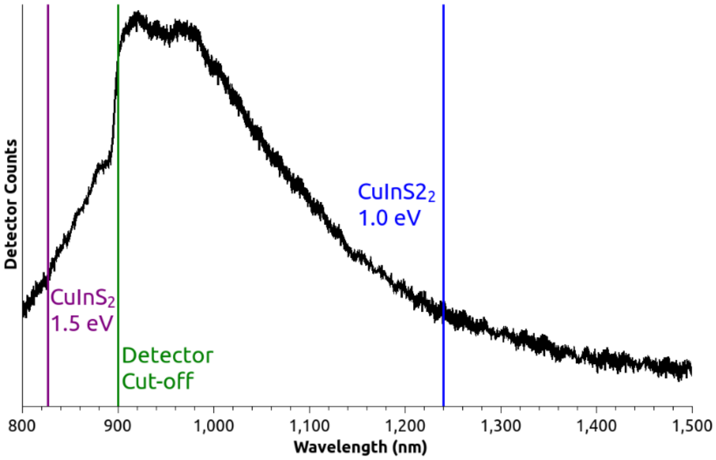

Figure 5.6: PL spectrum for CISSe nanoparticle films after 1 h of annealing at 250 °C. The bandgaps of pure $CuInS_2$ and $CuInSe_2$ are presented for comparison. The detector used has an abrupt reduction in sensitivity at approximately 900 nm.

solution mixture of chalcogen atoms ($CuInS_xSe_{2-x}$), meaning that both chalcogens from the polymer have been effectively incorporated. It is likely that the broadness of the peak is due to the fact that a population of particles with a range of chalcogen stoichiometries that very between that of $CuInS_2$ and $CuInSe_2$ are illuminated simultaneously, thereby producing an amalgam of spectra that convolute to produce the broad peak observed in the data. However, the data are also promising in that the PL signal is not completely quenched, as was seen in the small CIS particles that were annealed in the presence of Se vapor. Accordingly, although it is more difficult to remove all of the selenium sulphide terpolymer, it may be useful as a mechanism to passivate surface defects when it is printed with the nanoparticles and is slowly volatilized as the films are annealed at this low temperature.

These results in conjunction with the previous data and discussions allow for the formation of a generalized scheme for this thin film formation process. **Scheme 5.2** shows a schematic representation of the process. First, the initial nanocomposite consists of

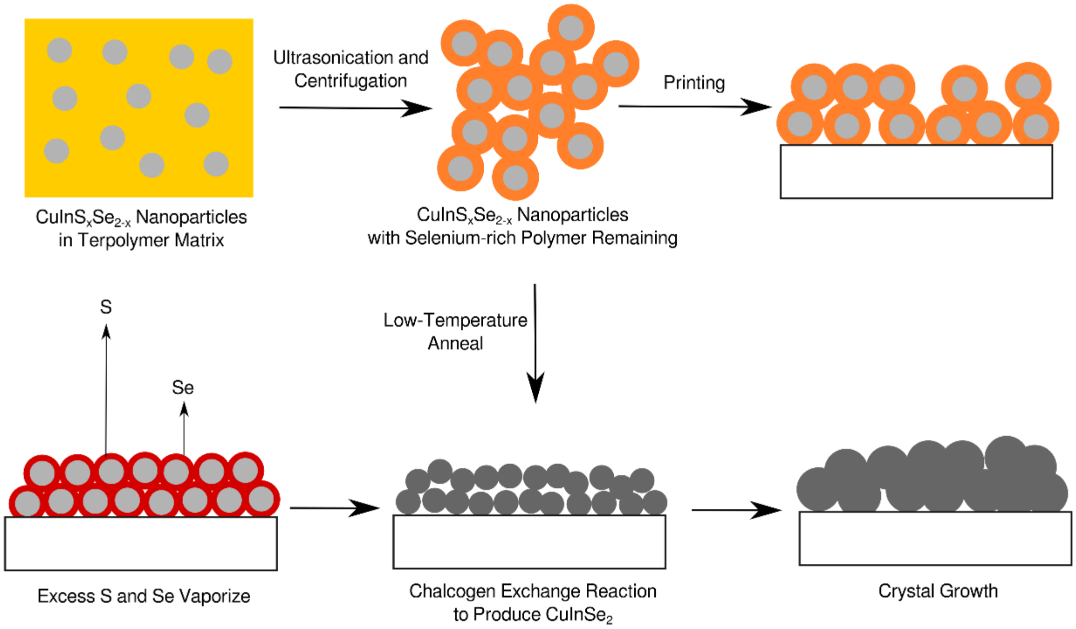

Scheme 5.2: Schematic representation of a low-temperature, completely solution-processed method for printing $CuInSe_2$ PV absorber layers using an ink that consists of $CuInS_xSe_{2-x}$ nanoparticles coated with a selenium sulfide terpolymer.

$CuInS_xSe_{2-x}$ nanoparticles suspended within a selenium sulfide terpolymer matrix. Next, most of the polymer is removed via the ultrasonication and centrifugation process, however some selenium rich polymer remains and coats the nanoparticles. Next, the nanoparticle ink is printed onto a substrate and is annealed at 250 °C. During this annealing process, the extra terpolymer vaporizes, where the sulfur vaporizes more rapidly due to its higher vapor pressure, so the film becomes steadily more selenium rich as the annealing process proceeds. Finally, once all of the extra terpolymer has evaporated, the $CuInSe_2$ films will undergo crystal growth, producing a dense, conformal PV absorber layer. Although the data and results presented in this section indicate that the process outlined in Scheme 5.2 is occurring to some extent, the complete scheme has not been fully realized.

5.4 Conclusions

The results from this chapter indicate that this new technique provides a promising route towards fabricating low-temperature, completely solution-processable, low-bandgap chalcogenide photovoltaics. Previous work in this field has relied on one or more steps that require high-temperature processing, vapor-phase reactions, or hydrazine solvents to produce these materials. Therefore, this work constitutes a unique method to achieve the goals discussed in sections 1.6 and 1.7; where newly invented chalcogen polymers are used to produce novel nanoparticle inks that can then be subsequently printed to directly produce a functioning CISSe PV absorber layer.

Chapter 6. Improved Polymer Structures

6.1 Introduction

The results from the previous chapter have shown that is it possible to make a mixed chalcogenide photovoltaic material such as $CuInS_xSe_{2-x}$ (CISSe), using a polymer that contains both sulfur and selenium atoms within the polymer backbone. Although this is a substantial step forward, there are several limitations to the techniques discussed in Chapter 5. Firstly, the nanoparticle formation is conducted within a molten polymer that contains a very large excess of chalcogens, not within a conventional solvent. Secondly, the necessary kinetics of the nanoparticle formation mechanism is impeded since metal species diffusion is likely slowed within the viscous polymer, as compared to typical solvents.[121–123] The consequence of these two points is that it is more probable that secondary phases such as Cu_2Se, Cu_2S, In_2Se_3, and In_2S will form instead of the desired CISSe material. This is because a metal atom is much more likely to react with an abundant chalcogen atom before it is in the proximity of another metal atom. This limitation is evidenced by the Raman spectrogram shown in Figure 5.4, which shows the presence of these secondary phases.

Therefore, the next phase of this research focused on modifying the polymer structure in a number of ways in order to address this issue and to develop and expand the capabilities of this emerging polymer technology. First, this work aimed to develop new polymer structures that enabled the polymers to be soluble at high concentrations in organic solvents. This allows the polymers to be used for a variety of solution-processing methods, which drastically improves the utility of the polymers for printed photovoltaics applications. In addition, with highly soluble polymers that can react with metal precursors in solution, it is easier to limit the formation of subspecies since it is more likely that both copper and indium precursors are proximal to a nucleated seed crystallite. Second, this work focused on developing polymers that contain organic monomer moieties that allow the polymers to coordinate with metal cations and to be miscible with solutions of metal salts. This allows the polymers to be mixed with various metal precursors, thereby producing one ink that contains all of the necessary ingredients to directly produce a semiconducting chalcogenide material. Third, this phase of the project focused on developing a polymer with only selenium atoms and no sulfur atoms. This is beneficial for photovoltaic device performance, since it has been shown that for both CZTSSe and CIGSSe, devices with stoichiometries of mostly selenium exhibit the best PV performance.[36,67,124,125] It has been posited that the selenium-based devices have superior device performance because their propensity to form detrimental defects is lower.[126] Specifically, Chen *et al*. suggested through density function theory (DFT) calculations and finite elements simulations of CZTSSe, that the conduction band edge downshift caused by $[2Cu_{Zn} + Sn_{Zn}]$ in CZTSe is much smaller than in CZTS, so the electron trapping effect is much weaker in CZTSe.[126] Moreover, the formation energies of the isolated deep donor defects Sn_{Zn}^{2} + and V_{Se}^{2+} are much higher in CZTSe than in CZTS, so the concentration of the recombination centers is lower.[126] Therefore, it is extremely beneficial to develop a Se-only polymer from a device-physics perspective. Fourth, this phase of the project also developed a method to vary the S to Se ratio in the polymers. This is attractive because in kesterite and chalcopyrite materials the bandgap of can be varied from about 1.0 eV to 1.5 eV by varying the S to Se ratio,[37,68] which overlaps well with the solar spectrum (Figure 1.4) and provides a mechanism for bandgap tuning relative to the Shockley-Queisser maxima and the principles of detailed balance (see Section 1.2 for discussion). **Figure 6.1** shows the Shockley-Queisser maximum efficiency as a function of bandgap relative to the bandgaps of kesterite and chalcopyrite materials that can be made using a sulfur-only polymer (PolyS), a selenide only polymer (PolySe) and a mixed sulfoselenide polymer with varying chalcogen stoichiometry (PolyS_xSe_y).

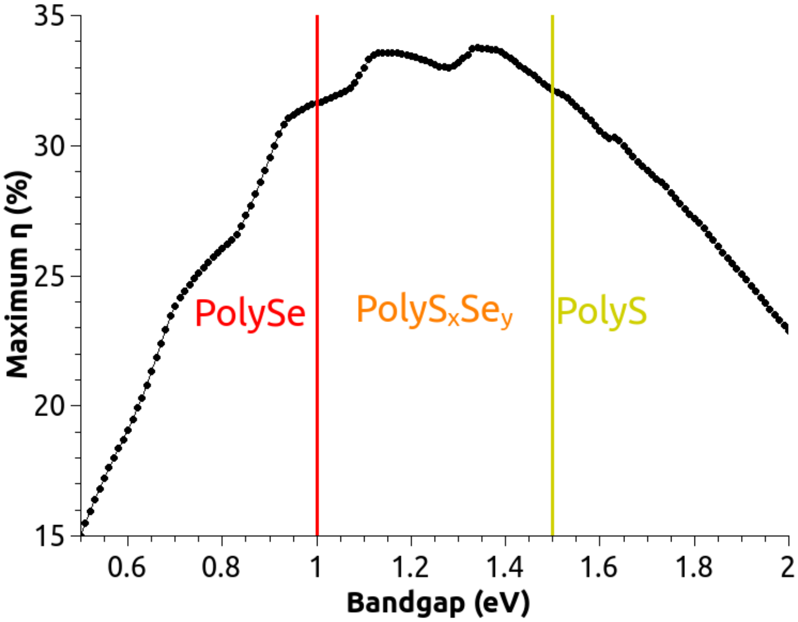

Figure 6.1: Shockley-Queisser maximum power conversion efficiency (η) for a single-junction PV device as a function of bandgap.[142] The bandgaps of kesterite and chalcopyrite materials can be varied within the maximum range of these data depending on polymer stoichiometry.

6.2 Polymer synthesis

6.2.1 Sulfur polymer synthesis (PolyS)

Elemental sulfur (1.0 g, 31.2 mmol S atoms) was placed in a 25 mL three neck flask. The flask was connected to a temperature probe, a condenser, and connected to a Schlenk line. The flask was placed on a heating mantle and was purged of air by alternating between vacuum and dry nitrogen several times. The mixture was heated to 150 °C under dry nitrogen. As soon as the sulfur melted, forming a yellow liquid, N,N-dimethylvinylbenzylamine (DMVBA, mixture of isomers, 0.91 mL, 5.2 mmol, 97%) was injected. The solution was heated to 185 °C and held for 10 mins to allow the organic monomer to completely react with the sulfur radicals.

6.2.2 Selenium disulfide polymer synthesis (PolySSe)

Selenium disulfide (SeS_2, 1.0 g, 7.0 mmol) was placed in a 25 mL three neck flask. The flask was connected to a temperature probe, a condenser, and connected to a Schlenk line. The flask was placed on a heating mantle and was purged several times with vacuum and dry nitrogen. DMVBA (mixture of isomers, 0.91 mL, 5.2 mmol, 97%) was injected into the flask. The mixture was heated to 200 °C under dry nitrogen with stirring for 25 min, to allow the organic monomer to reflux and completely react with the selenium sulfide radicals.

6.2.3 Selenium polymer synthesis (PolySe)

Selenium (Se, 1.0 g, 12.7 mmol) was placed in a 25 mL three neck flask. The flask was connected to a temperature probe, a condenser, and connected to a Schlenk line. The flask was placed on a heating mantle and was purged several times with vacuum and dry nitrogen. The mixture was heated to 225 °C under dry nitrogen with stirring for 10 min to form liquid selenium. DMVBA (mixture of isomers, 2.2 mL, 12.6 mmol, 97%) was injected into the flask dropwise over the course of 5 min, to ensure that the mixture remained at the same temperature throughout the course of monomer addition (225 ± 5 °C). The mixture was reacted for another 25 min once all of the monomer was injected, to allow the organic monomer to reflux and completely react with the selenium sulfide radicals. The flask was cooled immediately once the mixture became viscous, in order to limit the polymer growth and network formation to retain solubility.

6.2.4 Chalcogen polymer isolation and purification

The chalcogen polymer (500 mg) was placed in a 20 mL vial and combined with 20 mL of chloroform ($CHCl_3$). The vial was sealed and placed in an ultrasonicator for 60 min. This mixture was pipetted into two 20 mL Teflon centrifuge tubes and was centrifuged at 5 krpm for 10 min. The isolated polymer remained in solution while the unreacted chalcogen side-products dropped out of solution. The polymer was decanted from the centrifuge tubes and combined into a 20 mL vial. The $CHCl_3$ solvent was removed under reduced pressure and placed under high vacuum for

12 h to ensure removal of the solvent.

6.2.5 Polymer solution and ink preparation

The chalcogen polymers were dissolved in an organic solvent such as toluene at concentrations of 480 mg per 1 mL to form printable inks. It is possible to increase the concentration beyond this point, where the mixture begins to form increasingly viscous gels. Beyond the threshold of approximately 800 mg of polymer mixed with 1 mL of solvent, fractions of solvent are dissolved into the polymer.

6.3 Results and Discussion

Many different monomers were screened for this study, including various functionalized styrene monomers such as styrene, methylstyrene, trimethylstyrene, ethylstyrene, vinylnaphthalene, vinylanthracene, vinylbenzylamine, stilbene, vinylpyridine, nitrostyrene, vinylbenzyl alcohol, vinylbenzoic acid, fluorostyrene, and chlorostyrene. However, for the sake of brevity, this work will focus on discussing the use of the monomer N,N-dimethylvinylbenzylamine (DMVBA) which was found to be the most promising monomer for producing chalcogen polymers for printed PV applications for the following reasons. First, the DMVBA monomer has a boiling point of 213 °C, which is high enough for the liquid monomer to be reacted with molten selenium, which begins to melt at approximately the same temperature. Second, the lone electron pair and therefore Lewis basicity of the ternary amine moiety allows for the chalcogen polymers to be miscible with solutions of metal salts and allows for the polymers to directly coordinate with metal cations, while avoiding some of the undesired side-reactions that can occur between chaclocen atoms and primary amines.[41,127] Third, the DMVBA monomer was found to impart the resulting polymers with a high level of solubility in organic solvents such as toluene. The important properties of this class of polymers are illustrated in **Figure 6.2**.

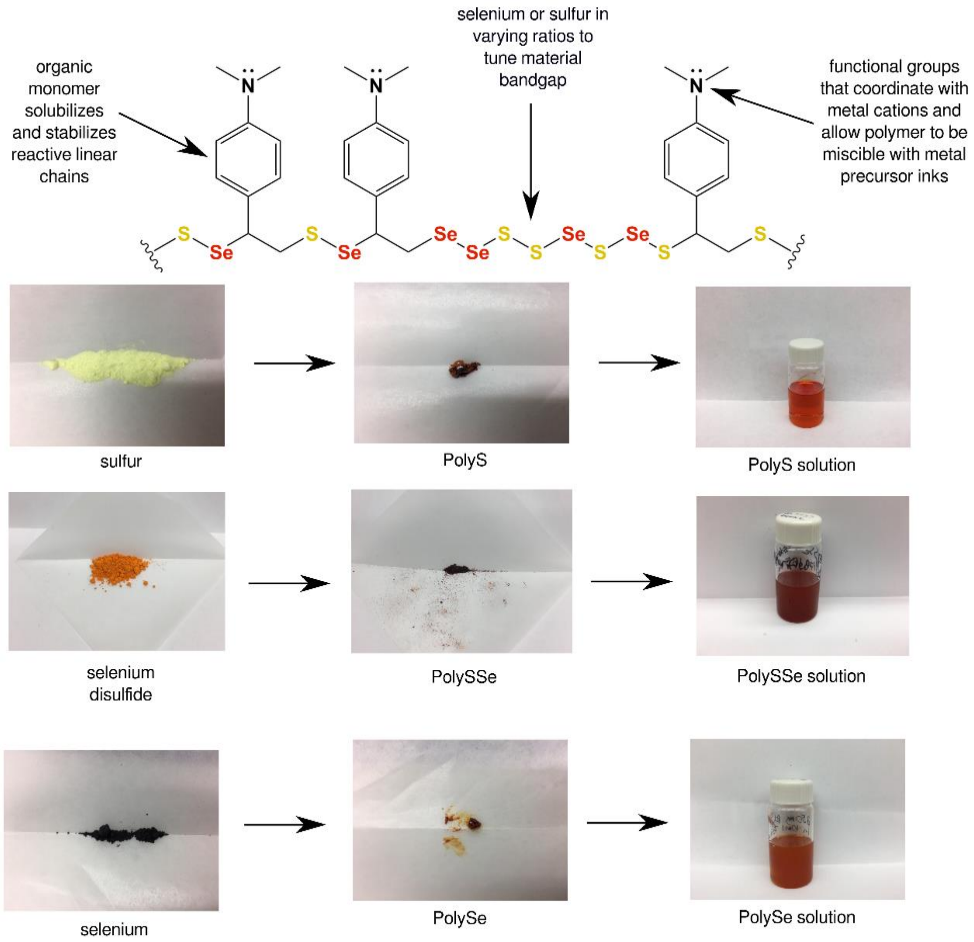

Figure 6.2: The DMVBA based polymers are stable, highly soluble, highly reactive, are easily printable, are miscible with metal cation precursor solutions, and can be designed with varying ratios of S and Se to tune semiconductor bandgaps.

Although it is possible to synthesize a polymer with any ratio of S to Se atoms by incorporating varying ratios of S and Se into the molten chalcogen and monomer mixture, as a proof of concept three different polymers with varying S to Se ratios were chosen. These are a 100% S polymer (PolyS), a 100% Se polymer (PolySe), and a 66% S to 33% Se (S_2Se) polymer (PolySSe), in order create a pathway for future bandgap tuning concepts that are presented in Figure 6.1.

PolyS and PolySSe can be synthesized using techniques that are similar to those outlined in Chapters 3 and 5, however the process for producing PolySe was considerably more challenging than previous polymer synthesis methods. Elemental selenium has a staggeringly large variety of allotropes.[128,129] These include an amorphous red colored allotrope that consists of Se_8 and Se_6 ring structures that are similar to sulfur and selenium disulfide, as well as a black or grey colored molecular solid structure that consists of linear chains of selenium atoms.[128,129] These molecular solids can be arranged as an amorphous (black allotrope) assortment of chains or in a hexagonal crystal lattice of helical chains (grey allotrope).[128,129] The ring-structured allotropes are less stable than the linear chain structure and consequently the ring-structured allotropes will revert to the linear structure once heated to melting temperature and then cooled again.[128,129] Therefore, this work necessarily focused on developing a selenium polymer from the linearly structured black allotrope as presented in **Scheme 6.1** and outlined in Section 6.2.3.

A selenium polymer synthesis was initially attempted using the methylstyrene monomer that had previously been successful. However, it was discovered that because the methylstyrene boiling point is 170 °C and because elemental selenium melts between 210 and 225 °C, then the

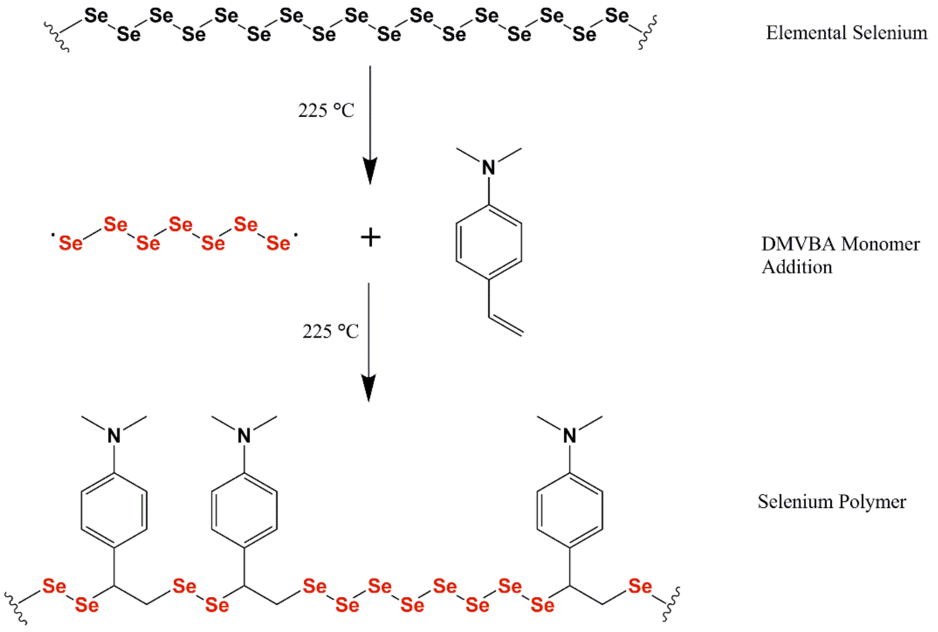

Scheme 6.1: Selenium polymer (PolySe) synthesis with DMVBA monomer. Elemental selenium exists as linear chains of selenium atoms. Upon heating to 225 °C these selenium atom chains break down into oligomeric radicals. These radicals are subsequently reacted with the DMVBA monomer to produce PolySe.

synthesis will fail because the monomer will evaporate before it reacts with the selenium radicals effectively. After studying various monomer options, DMVBA was finally selected because of its higher boiling point and the other beneficial attributes that were previously discussed.

It was also discovered that although the majority of the selenium atoms eventually become incorporated into the polymer structure, the final product is actually a composite of unreacted elemental selenium particles suspended within a selenium polymer matrix. In addition, it was discovered that although the increased boiling temperature of DMVBA was suitable for the polymer synthesis, since the reaction is conducted slightly above the boiling point of DMVBA, a significant fraction (in some cases up to approximately 50%) of the monomer was lost during the synthesis despite the attachment of a refluxing condenser to the reaction flask. This issue was particularly pronounced near the beginning of the reaction, when the majority of the monomer is not yet chemically linked to the selenium atom chains and can therefore be volatilized more easily. These issues necessitated a subsequent purification step that removed the unreacted elemental selenium, thereby isolating the soluble selenium polymer. This process is discussed in Section 6.2.4 and is presented in **Figure 6.3**.

PolySe, PolSSe, and PolyS can be readily dissolved in organic solvents such as toluene and are stable for months. Furthermore, if these polymers are dissolved in toluene beyond a concentration of approximately 240 mg/mL, then the resulting polymer inks begin to become viscous and are very well suited for simple printing procedures such as blade coating. This is an extremely beneficial characteristic for printing PV devices and is one that is not easily achieved with other methods. For example, single molecule chalcogen sources such as thiourea will drop

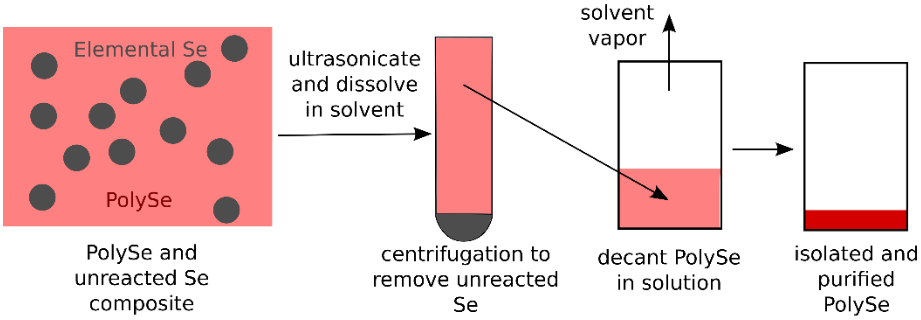

Figure 6.3: The PolySe synthesis produces unreacted selenium particles that are embedded within the selenium polymer. The soluble PolySe is dissolved in solvent and then extracted from the unreacted selenium and isolated, thereby yielding a purified PolySe.

out of solution at concentration approaching 1 M, so an ink based on this type of precursor is not well suited for many printing techniques, especially those that would be employed in a roll-to-roll printing facility.

6.4 Conclusions

Drawing from some of the limitations that were discovered during the course of research outlined in Chapter 5, this phase of the project focused on developing new and improved chalcogen polymer structures. It was revealed that the previously used methylstyrene-based polymers had several limitations that required a reengineered molecular structure to move forward. Specifically, developing highly soluble polymers will help improve PV material formation kinetics. Furthermore, inventing a polymer structure that enables the polymer to directly coordinate with metal cations and be soluble with metal salt solutions greatly expands the range of available printing and reaction schemes that can be used. In addition, developing a polymer that only has selenium atoms in the polymer backbone is beneficial from a device physics perspective. Finally, it is also very useful to be able to synthesize polymers with a range of sulfur to selenium stoichiometries in order to tune the bandgap of kesterite and chalcopyrite PV materials near the Shockley-Queisser maximum. Quite remarkably, the polymers discussed in this chapter are able to achieve all of these goals simultaneously.

Chapter 7. Directly Forming CISe with a PolySe Ink

7.1 Introduction

In order to meet the clean energy demands of the future, photovoltaics (PV) must be efficient, stable, and simple to manufacture.[21,130] To date, there are no viable technological options within the PV field that ideally exhibit all three of these attributes simultaneously. For example, perovskite materials are very efficient and can be printed using solution-processing methods, which provides a route for simple manufacturing; however, they have considerable stability issues.[131,132] Organic photovoltaics (OPVs) can also be solution-processed, are relatively cheap and simple to manufacture, can be reasonably stable, but are comparatively inefficient.[133] Conventional silicon PV and thin-film metal-chalcogenide materials such as CdTe, the chalcopyrite material $CuInS_xSe_{2-x}$ (CISSe), the gallium alloy variant $CuIn_xGa_{1-x}S_ySe_{2-y}$ (CIGSSe), and the earth-abundant kesterite material $Cu_2ZnSnS_xSe_{4-x}$ (CZTSSe) are stable and efficient, but are extremely complicated to manufacture, which causes the technology to remain expensive.[7,21,27,30,130,134] This issue is represented graphically in **Figure 7.1**.

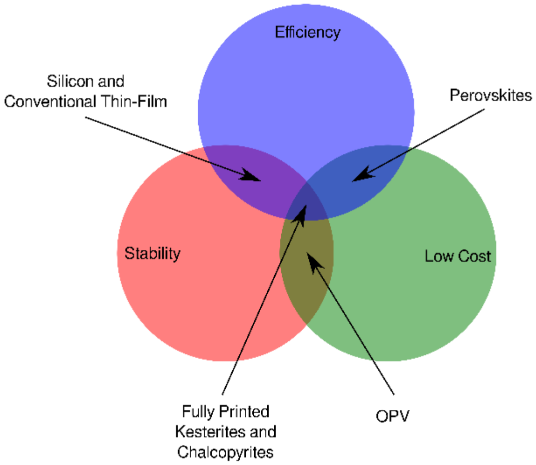

Figure 7.1: Conventional PV technologies such as silicon, CdTe, and CIGSSe (thin-film) are very efficient and stable, but are extremely costly to manufacture. Perovskite devices are simple to make and can achieve high efficiencies, but have considerable stability issues. Organic photovoltaics (OPV) can be comparatively stable and are simple to manufacture with solution-based techniques, but have limited efficiencies.

The work presented in this chapter aims to understand how the chalcogen polymers developed in Chapter 6 can be used to fabricate metal-chalcogenide photovoltaic materials that are efficient, stable, and simple to manufacture via solution-processing. Some progress has been made to develop solution-based methods of deposition for metal-chalcogenide materials in order to simplify PV device fabrication.[29,47,67,81,124] However, all of these methods deposit sulfurized films that must then undergo a vapor-phase reaction where elemental selenium is heated, vaporized and subsequently reacted with the film to produce a selenized material, as depicted in **Figure 7.2**. This method is used exclusively since it is the only viable option for selenium introduction because there has previously been no viable options for readily printable selenium precursors. Producing selenized materials is important because of the device physics advantages that come with a selenized material, as discussed in Chapter 6. Therefore, although these methods constitute a promising step forward, they cannot be used to make completely solution-processed materials.

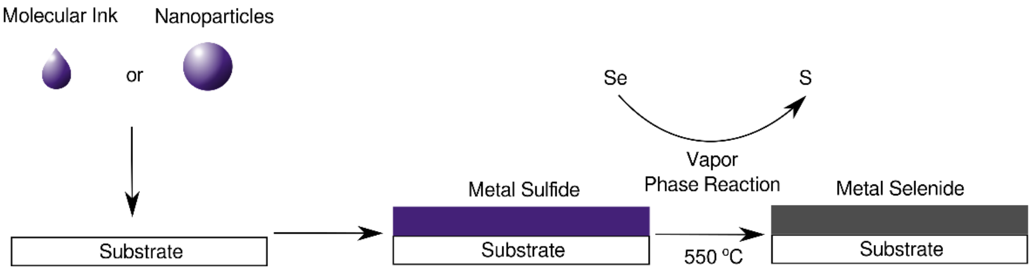

Figure 7.2: To date, all printed metal-chalcogenide PV device fabrication procedures that use inks or nanoparticles still rely on a high-temperature selenium vapor-phase reaction to produce the final selenized material.

The goal of the work discussed in this chapter is to eliminate this selenium vapor-phase reaction step, which is a tremendously challenging task, considering the ubiquity of this technique and the fact that it has remained the best method for the better part of a decade. [29,47,67,81,124] As discussed in Chapter 1, one of major obstacles for rapid PV deployment is high CAPEX costs. The process shown in Figure 7.2 requires high temperature, high vacuum, controlled atmosphere, and precise vapor-phase reaction techniques, all of which will necessitate advanced equipment and therefore high CAPEX costs. This hurdle severely constrains the appeal of this technology in comparison to conventional silicon and thin-film deposition methods. Consequently, this type of process has remained limited to the academic realm and has not been industrially implemented. Moreover, the vaporization of elemental selenium is not well suited for scaling up to industrial production, since it is a very tedious process with low throughput, comparatively limited control, and requires a substantial excess of selenium.

A much more appealing process would enable a metal-selenide material to be directly formed on a substrate, thereby eliminating the vapor-phase reaction step. **Figure 7.3** illustrates an idealized, very low CAPEX printing process, where one ink can be used to directly form a metal-selenide material with simple printing procedures.

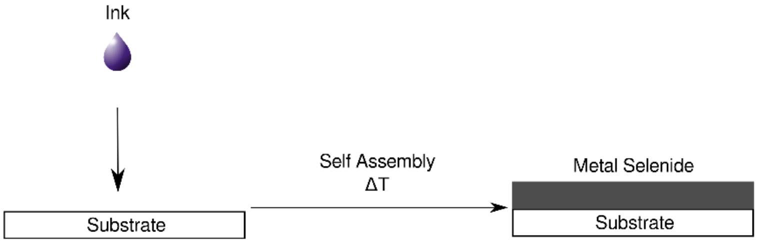

Figure 7.3: An ideal printed PV method would use an ink that contains all of the necessary components to directly form a metal-selenide PV material through self-asssembly mechanisms once heated.

7.2 Methods

7.2.1 Ink Formulation

Selenium polymers (PolySe) were synthesized using the techniques discussed in Chapter 6, Sections 6.2.3, and 6.2.4. The resulting purified PolySe was dissolved in anhydrous toluene in an nitrogen atmosphere glovebox at a concentration of 720 mg in 6 mL.

Next, copper acetate (Cu(I)Ac, 93 mg, 0.75 mmol, 97%) and indium acetate (In(III)Ac, 219 mg, 0.75 mmol, 99%) were dissolved in a mixture of dimethylformamide (DMF) and tetramethylethylenediamine (TMEDA) (1:3 volume ratio, 1.2 mL TMEDA and 4.8 mL DMF) in an inert atmosphere glovebox.

The PolySe ink and the metal precursor inks were mixed together in an inert atmosphere glovebox in equal parts immediately prior to printing, to prevent reaction of the reagents prior to their use.

7.2.2 Printing Procedures

All printing and annealing techniques described herein were conducted within an inert atmosphere glovebox with H_2O levels < 1 ppm and O_2 levels < 10 ppm. Once the inks were ready to use, two different printing techniques were implemented. The first technique implemented spin-coating methods. Specifically, 100 µL of the mixed ink was pipetted onto a cleaned 2.5 cm × 2.5 cm Mo coated SLG substrate and spun at 500 rpm for 60 s. The resulting films were then dried at 100 °C for 2 min. This process was repeated 10 times to produce a film that is approximately 1 µm thick. The resulting films were annealed at on a hotplate at 400 °C for 30 min.

Blade-coat printing was also used as an effective demonstration of the capabilities of the polymer technology and as a means to prove that the methods described herein can be easily implemented on an industrial scale roll-to-roll printing system. Specifically, 10 µL was pipetted onto cleaned 2.5 cm × 2.5 cm Mo coated SLG substrate and were printed using a 125 µm thick spacer.

7.2.3 Washing and Annealing Procedure

The blade-coated films were then heated to 115 °C for 30 min. Next, the films were cooled to RT and transferred to a sealed Teflon container. 50 mL of anhydrous $CHCl_3$ was then added to the container on top of the substrate and the container was sealed inside of the glovebox. Next, this container was transferred out of the glovebox and placed in a sonicator bath for 30 min. The container was then removed from the sonicator and opened, the films were washed briefly with $CHCl_3$, and were then transferred back into the glovebox. Next, the films were annealed on a hotplate at 400 °C for 30 min.

7.3 Results and Discussion

7.3.1 Directly Forming CISe

The first phase of this project investigated the feasibility of producing a CISe PV thin-film using the simplified printing procedure that is outlined in Figure 7.3 and Section 7.2.2. The resulting thin-films were characterized using techniques discussed in detail in Chapter 2 and utilized in other chapters. The morphology of the resulting films is shown in the SEM images of **Figure 7.4**. The images show that nanocrystals in the range of 100–500 nm have nucleated within

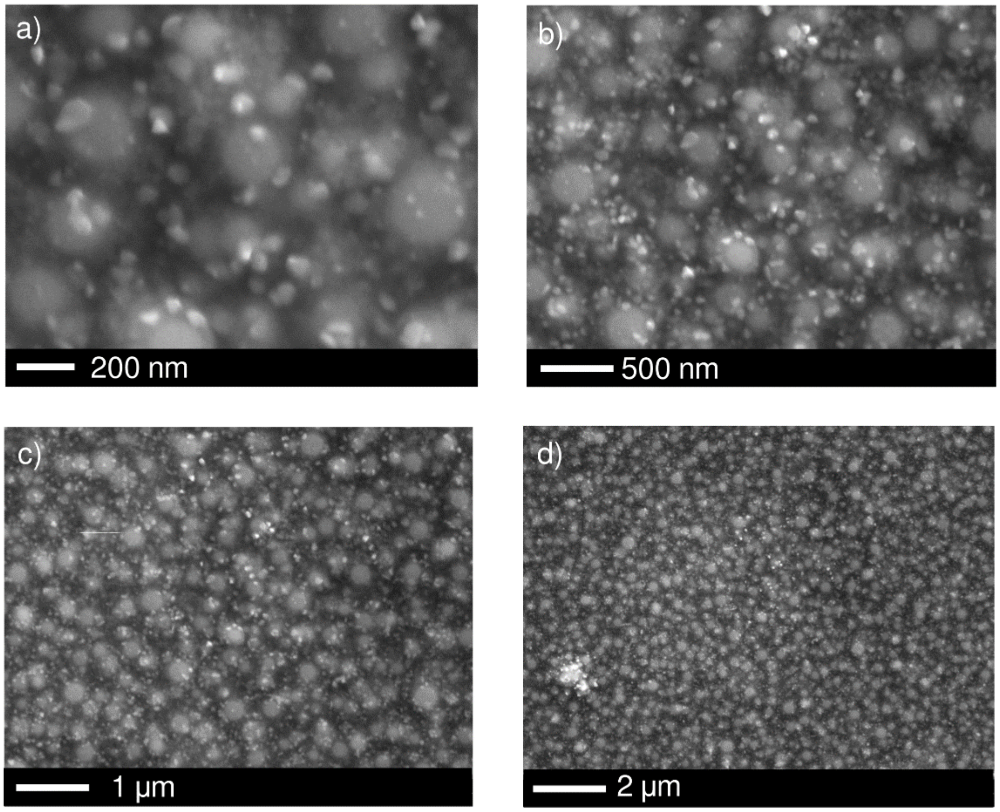

Figure 7.4: SEM Images of films made using PolySe. The inks consisted of a mixture of PolySe and Cu/In precursor salts in solvent. The inks were printed using spin-coating and were annealed at 400 °C for 30 min. Decreasing magnification from a), b), c) to d).

the thin-film. There is also a population of smaller particles within the range of 10 nm. The crystals are separated by a darker colored amorphous region, which is likely excess polymer. The XRD data shown in **Figure 7.5** suggest that crystalline $CuInS_2$ is formed. The data also show the presence of broad secondary peaks, which are likely due to the small crystals or amorphous material that is seen in Figure 7.4. The EDS data shown in **Table 7.1** show that the films have the appropriate Cu/In ratio, but are slightly selenium rich, which is likely due to an excess of PolySe. Note that at this stage it is difficult to calculate the stoichiometry of selenium to metals in the ink, since an exact molecular weight or monomer to chalcogen ratio is not known empirically after the polymer is synthesized, but is calculated based on the reaction precursors. Furthermore, the EDS map data presented in **Figure 7.6** shows that the films have a relatively uniform distribution of copper, indium, and selenium.

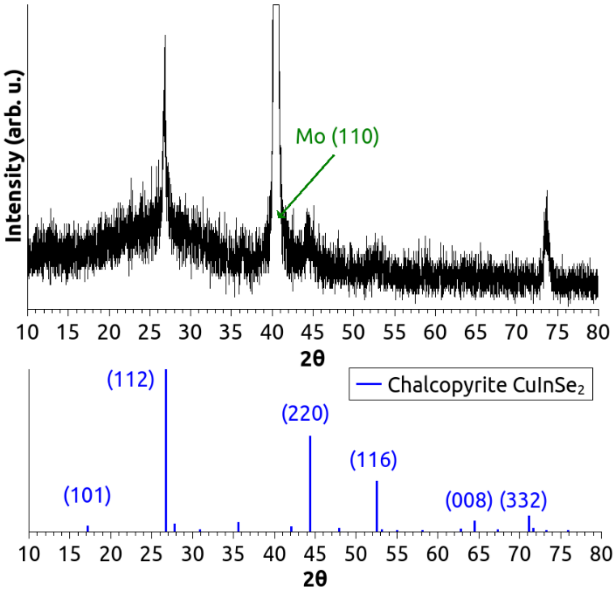

Figure 7.5: XRD pattern for the films that are shown in Figure 7.4. The diffraction pattern is consistent with the formation of crystalline chalcopyrite $CuInSe_2$, however there are also broad background peaks present, which indicates the formation of a secondary polycrystalline material.

Table 7.1: Stoichiometric (EDS) ratios for annealed CISe films formed directly on substrate using PolySe

	Cu/In	**(Se)/(Cu+In)**
Film Stoichiometry	0.95 ± 0.05	1.27 ± 0.08

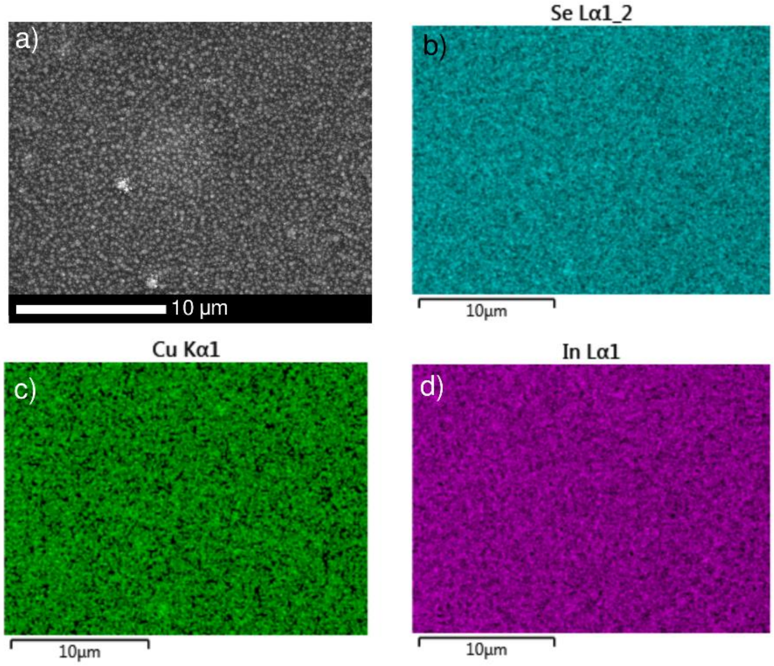

Figure 7.6: a) SEM image of films from Figure 7.4 with EDS mapping data for Se b), Cu c) and In d).

Building on these results, it is possible to improve this morphology by changing the ratio of PolySe to metals salts and by tuning the stoichiometry of the metals to improve the film morphology and to promote CISe formation. The films shown in **Figure 7.7** have an improved morphology that shows the formation of CISe nanocrystals. The EDS data in **Table 7.2** and **Figure 7.8** show that the thin films have the appropriate stoichiometry and that the elemental distribution is uniform on the micron scale, with some regions of varying metals ratios. The XRD data in **Figure 7.9** show that it is possible to produce highly crystalline $CuInSe_2$ using this method. The Raman spectrum shown in **Figure 7.10** confirms that crystalline CISe is formed and does not show

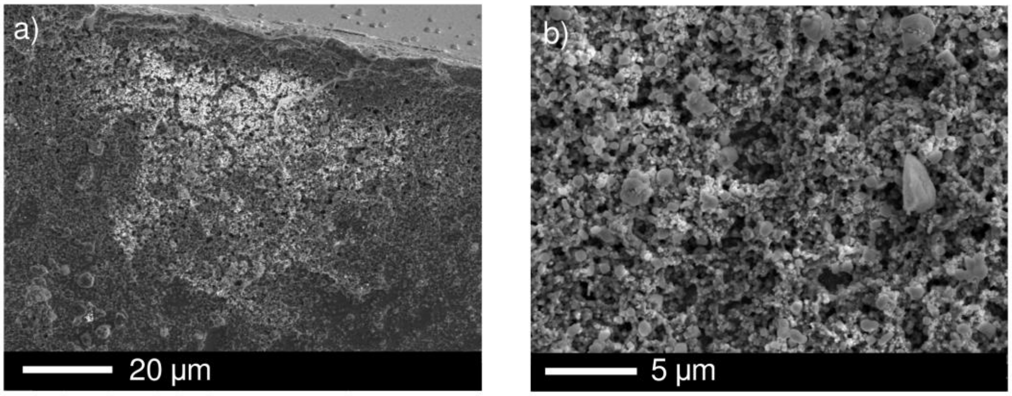

Figure 7.7: SEM Images of films made using PolySe. The inks consisted of a mixture of PolySe and Cu/In precursor salts in solvent. The inks were printed using spin-coating and were annealed at 400 °C for 30 min. Increasing magnification from a) to b).

Table 7.2: Stoichiometric (EDS) ratios for CISe films shown in Figure 7.7

	Cu/In	**(Se)/(Cu+In)**
Film Stoichiometry	1.0 ± 0.2	0.9 ± 0.4

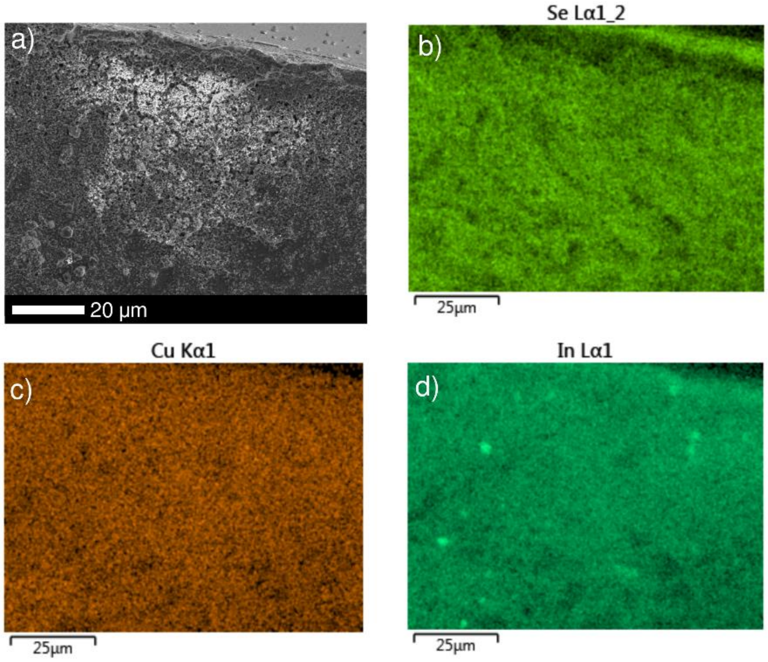

Figure 7.8: a) SEM image of films from Figure 7.7 with EDS mapping data for Se b), Cu c) and In d).

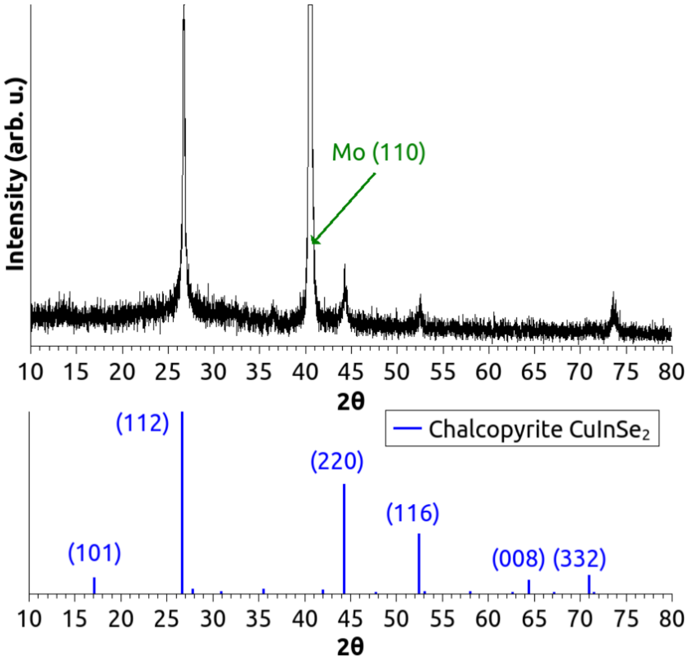

Figure 7.9: XRD pattern for the films that are shown in Figure 7.7. The diffraction pattern is consistent with the formation of crystalline chalcopyrite $CuInSe_2$ and is more crystalline than the pattern shown in Figure 7.5.

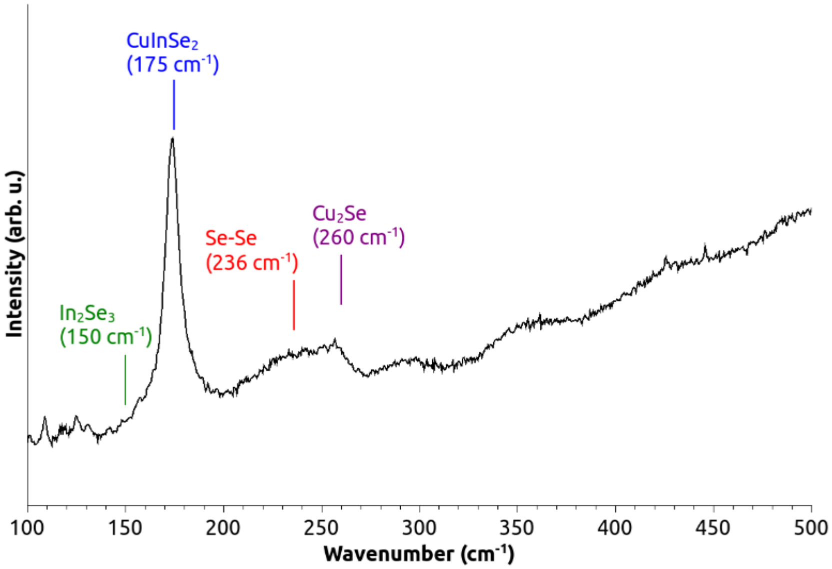

Figure 7.10: Raman spectroscopy for the films that are shown in Figure 7.7. The main peak is consistent with the formation of crystalline chalcopyrite $CuInSe_2$. The films have very minimal Cu_2Se formation and very little residual PolySe.

significant peaks for the resonance modes of subspecies such as Cu_2Se, CuSe, and In_2Se_3, which is an extremely promising result. Furthermore, the PL spectrums shown in **Figure 7.11** show that the material has promising opto-electronic properties and exhibits a bandgap that is directly situated at the expected value of 1.0 eV (1240 nm). These results prove that it is possible to produce opto-electronic quality $CuInSe_2$ using a selenium polymer and entirely solution-based printing techniques. Moreover, this result likely constitutes the first time a low-bandgap selenide PV material has been made using only printed inks and is therefore the first time that the selenium-vapor step has been effectively bypassed. Figure 7.11a shows the PL data as collected. Figure 7.11b shows the absolute photon flux replotted as a function of energy, the calculated peak energy value of 1.02 eV, and the full width at half max (FWHM) value of 93.6 meV. Figure 7.11c shows

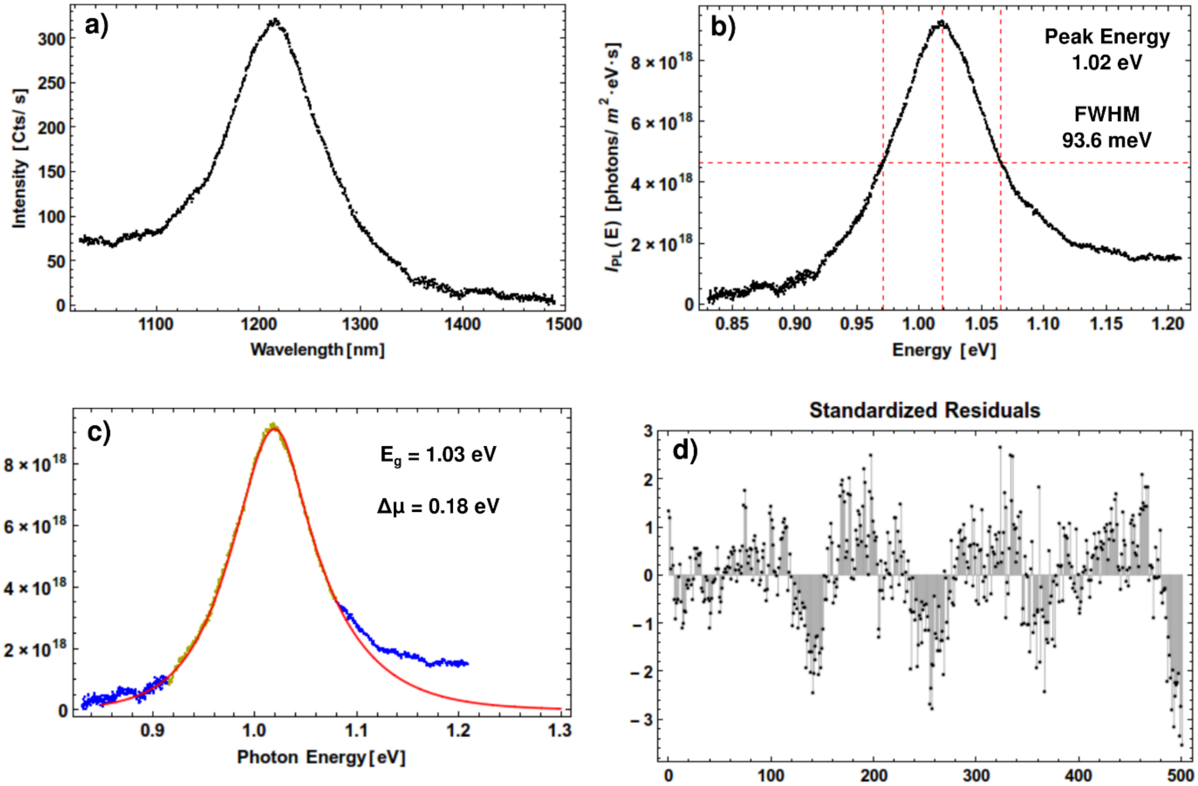

Figure 7.11: PL spectroscopy for the films that are shown in Figure 7.7 a) PL data as collected. b) PL data as a function of bandgap with peak energy and full width at half max (FWHM) values. c) PL data with curve fit for the data highlighted in green with E_g and $\Delta\mu$ values. Excluded data are shown in blue. d) Curve fit residuals for c).

the data fitted using the methods that were outlined in Chapter 2.[66] The curve fitting algorithm is designed to fit only one peak and so breaks down when the PL data are a result of a convolution of several spectra. It is likely that when the selenium polymer is used to directly from CISe nanoparticles, there are some smaller nanoparticles that are formed that exhibit quantum confinement effects and will produce PL spectra that are slightly blue-shifted from the bulk material bandgap. Therefore, the PL spectrum shown in Figure 7.11c exhibits a high-energy shoulder that is not typically seen for bulk films. This shoulder likely causes the curve fitting algorithm to break down particularly in the high energy range and so some data were excluded to achieve a fit (data used for the fit are highlighted in green while excluded data are shown in blue). The curve fit residuals shown in Figure 7.11d also suggest that the PL data are perhaps a convolution of several different PL signals, since there is some periodicity seen in the values. Accordingly, the bandgap (E_g), quasi Fermi level splitting values ($\Delta\mu$), and shape of the PL spectra should be considered qualitatively only. Nevertheless, these results show that it is possible to form CISe with reasonable opto-electronic quality using the selenium polymers.

However, despite this extremely promising result, these films had a number of attributes that remained problematic and challenging. In particular, although it is possible to form high quality CISe in some instances, it is very difficult to control the morphology of the resulting films using this technique, resulting in a variable film quality. The films exhibited a wide range of morphologies and stoichiometries, and frequently produced some amount of Cu_2Se and CuSe. For example, although the films shown in Figure 7.4 and Table 7.1 have a similar ink formulation to those of Figure 7.7 and Table 7.2, the resulting film morphologies and stoichiometries vary widely, where the films from Figure 7.7 have promising optoelectronic properties and produce a strong PL peak, while those from Figure 7.4 do not. In order to be industrially viable, this method will need to be much more controllable and reproducible.

One useful glimpse into why there is little control over the morphology of the films came when the films shown in Figure 7.4 were imaged as a cross-section. The images shown in **Figure 7.12** show a clear striation across the depth of the film, indicating that there is irreversible material formation during each of the subsequent spin-coating deposition steps. This result was very surprising, since it suggests that the polymer and metals precursors are reactive during the printing process before the 400 °C annealing step. Since the films are dried at 100 °C between each printing step, this suggests that there are some nanoparticles that form within the film at this low temperature, prior to the final 400 °C annealing step.

7.3.2 Low Temperature Reactions and Solvent Washing

When considered in totality, the results of section 7.3.1 are extremely promising. In short, this work has shown that it is possible to directly self-assemble optoelectronic quality CISe on a substrate with an entirely solution based method and simple printing procedures. Furthermore, the striation seen in Figure 7.12 suggests that CISe nanocrystals may be forming at temperatures much

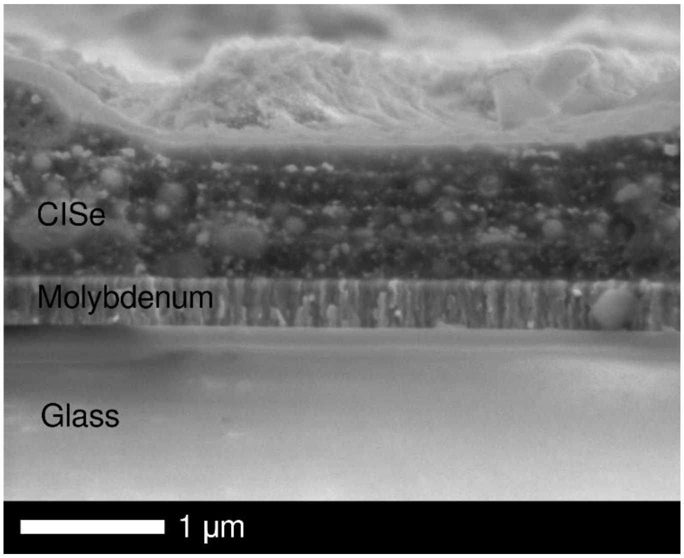

Figure 7.12: Cross-section SEM image of films from Figure 7.4 showing a striated deposition profile.

lower than initially anticipated. In order to examine this low temperature formation process, the next stage of this research focused on investigating the mechanisms of material formation that occur near 100 °C. Specifically, PolySe inks with Cu and In precursors were blade-coated onto substrates using the techniques discussed in Section 7.2.2. Next the films were heated to initiate nanoparticle formation using the methods discussed in Section 7.2.3 and as illustrated in **Figure 7.13**. This method is promising since it can be used to form nanoparticles directly on the substrate and at low temperatures. Once the particles have formed, then the excess polymer, monomers, and reaction side-products can be washed away, leaving behind a self-assembled layer of metal-chalcogenide nanoparticles. The films shown in **Figure 7.14** show the nanoparticles that have formed on the surface of the films at 115 °C and after a brief washing step. The particles can be clearly seen on the substrate and have a size of approximately 50-200 nm. The excess polymer, monomers, and reaction side-products constitute the dark-colored semi-transparent material that

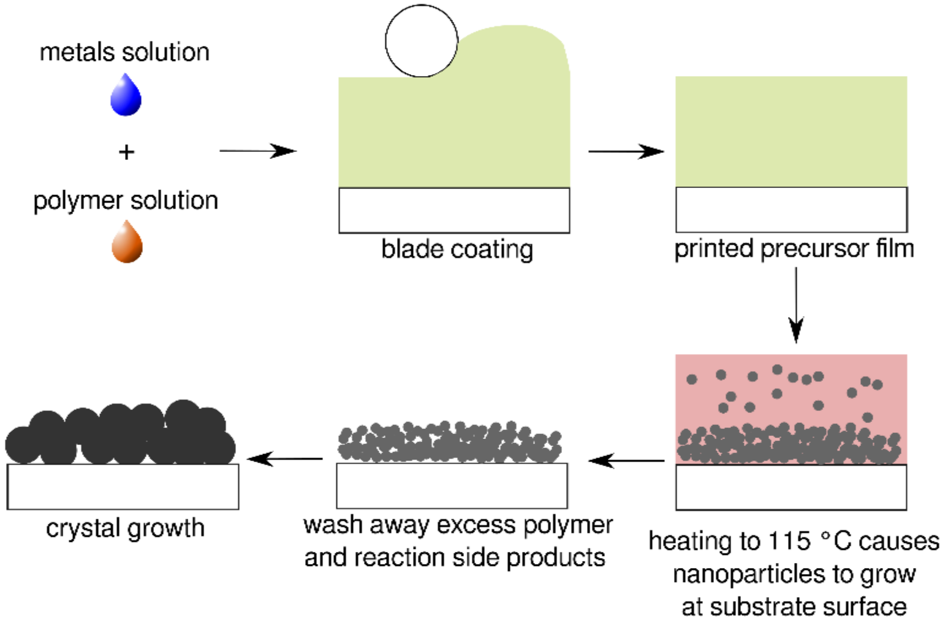

Figure 7.13: Procedure for directly forming CISe nanoparticles on a substrate at low temperatures. Once the nanoparticles have formed, the excess polymer, mononmers, and reaction side-products can be washed away, thereby revealing bare nanoparticles. These nanoparticles can then be sintered and annealed to form a thin-film material.

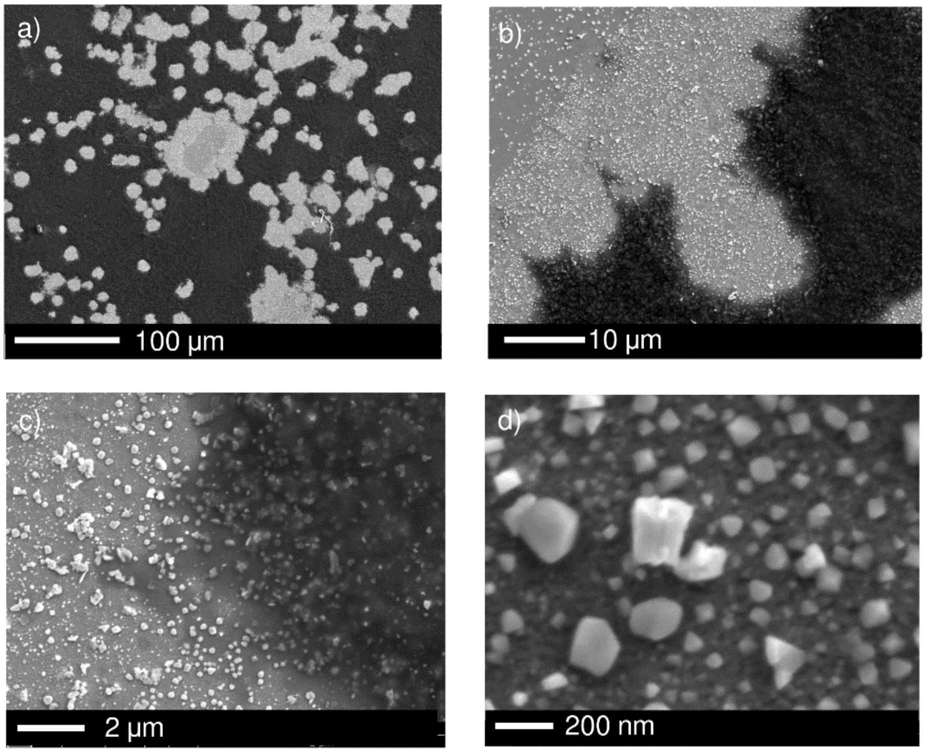

Figure 7.14: SEM images of metal-chalcogenide nanoparticles formed directly on a substrate from PolySe at 115 °C. The excess polymer, monomers, and reaction side-products constitute the dark-colored semi-transparent material that can be subsequently washed away after nanoparticle formation. Increasing magnification from a), b), c), and d).

is washed away in some areas but not in others. If the time of the washing step is extended, then all of this top material can be washed away, as shown in **Figure 7.15**. These films were then subsequently annealed at 400 °C for 30 min. **Figure 7.16** shows a cross-section image of these thin films with a corresponding EDS linescan across the depth of the absorber layer. It is important to note that the resolution of this EDS method is limited to approximately 1 µm, however the data provide a useful confirmation that nanocrystals containing Cu, In, and Se are grown of the surface of the substrate. **Table 7.3** shows the stoichiometry of the resulting films. **Figure 7.17** shows a top-down EDS map of the films. The films are significantly copper-rich, which suggests that Cu containing nanoparticles nucleate before In containing particles. However, there are locations where the stoichiometry is what is expected for $CuInSe_2$, as is the case in the linescan data shown

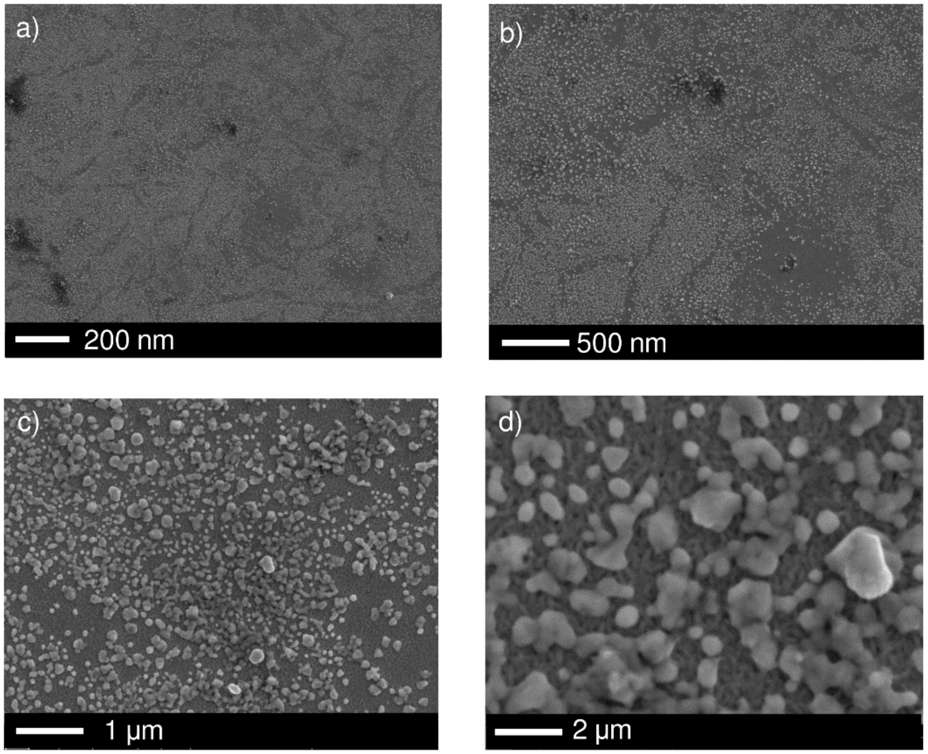

Figure 7.15: SEM images of metal-chalcogenide nanoparticles formed directly on a substrate from PolySe at 115 °C. The excess polymer, monomers, and reaction side-products have been effectively washed away and the resulting nanoparticles were annealed at 400 °C for 30 min. Increasing magnification from a), b), c), and d).

Table 7.3: Stoichiometric (EDS) ratios for CISe films shown in Figure 7.15

Element	**Se**	**Cu**	**In**
Atomic %	51.0 ± 1.8	45.3 ± 2.3	3.8 ± 0.9

in Figure 7.16. This suggests that although there are regions where $CuInSe_2$ forms at this low temperature, the metals precursors do not react equivalently. Moving forward, it is crucial that the Cu and In precursors react with equivalent kinetics to produce a high-quality material with appropriate stoichiometries for PV applications

7.4 Conclusions

The results of this section built upon the sulfur polymer work of the previous chapters to invent new selenium-based polymers in order to tackle the issue of producing low-cost

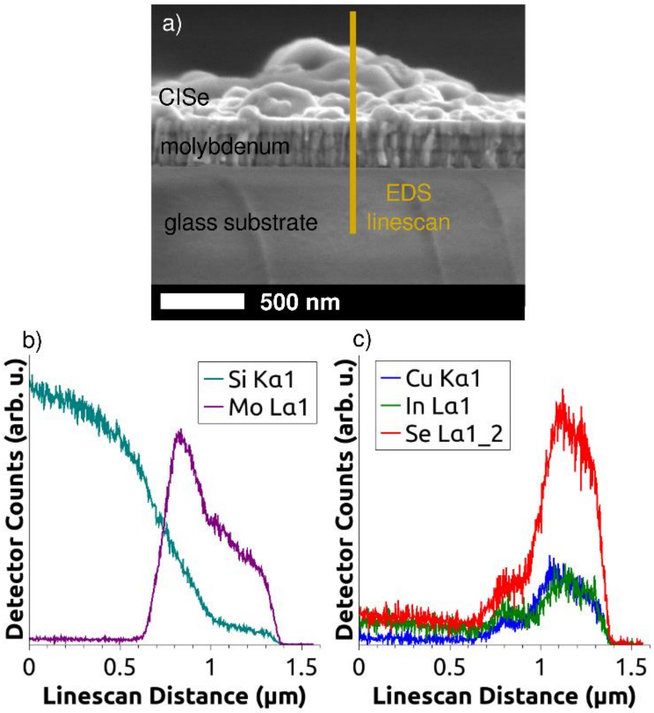

Figure 7.16: a) Cross-section SEM image of metal-chalcogenide nanoparticles from Figure 7.15 b) Substrate atom signal across depth of film. c) CISe atom signal across depth of film.

chalcogenide PV in an innovative way. These selenium polymers can be readily solution processed and can be designed with moieties that directly coordinate with metal precursors. Moreover, varying amounts of sulfur can be incorporated into the polymer backbone, in order to change the material bandgap and therefore potentially tune the material properties for maximal solar absorption and device performance. These new polymer inks can then be printed onto a substrate and heated to form a photovoltaic material directly on a substrate via self-assembly mechanisms. This method provides a pathway for producing completely solution-processed chalcogenide photovoltaics such as CISSe, CIGSSe, and CZTSSe with low-temperatures and an extremely simple process, which has not been previously demonstrated. Therefore, this work affords a unique opportunity to make gains within the field of printed photovoltaics by presenting a method to make

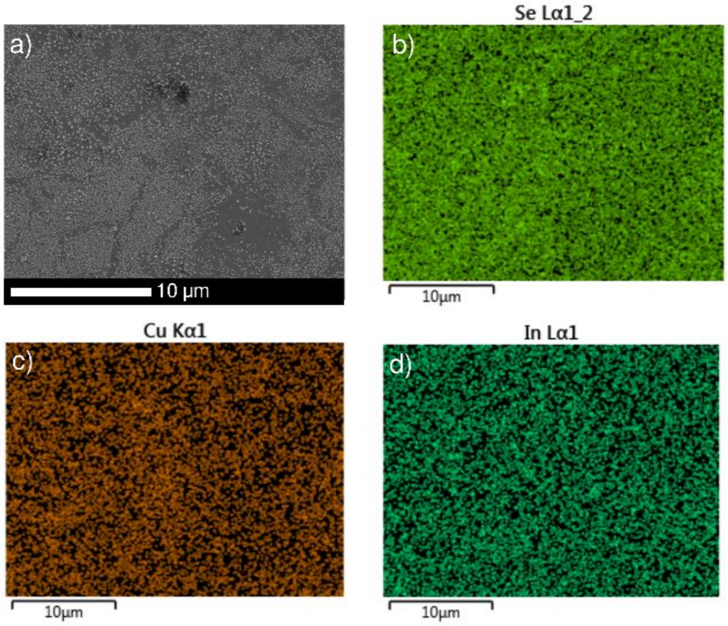

Figure 7.17: a) SEM image of metal-chalcogenide nanoparticles from Figure 7.15. and d) EDS mapping of Se b), Cu c), and In d).

PV materials that are efficient, stable, and simple to manufacture. This work has also concurrently invented a new class of polymers that can potentially be used for a range of additional applications.

These chalcogen polymer solutions can be combined with metal precursor solutions to produce an ink that contains all of the necessary components to directly form a PV material without any additional reagents. This ink can be printed onto a substrate (molybdenum coated glass) using simple, scalable printing techniques such as blade coating. This amorphous polymer film can then be heated (115 °C) to form semiconducting nanoparticles. During this process, the chalcogen atoms in the polymer backbone react with the metal precursors (for example: Cu^+ and In^{3+} salts) to form a photovoltaic material (for example: $CuInS_xSe_{2-x}$). The reaction produces a semiconducting nanoparticle layer with some reaction side products and remaining monomers, which are subsequently washed away with an organic solvent, thereby yielding a bare nanoparticle film without problematic carbon impurities. This nanoparticle film can then be annealed at a moderate temperature (300-400 °C) to produce a PV thin film. Although the results of this section constitute a tremendous step forward for this research, CISe material formation remains hampered by issues with reproducibility and the consistent formation of copper rich species. Unfortunately, at this stage, the process will need to be more reproducible in order to make complete PV devices for testing.

Chapter 8. Low Temperature Nanoparticle Formation in Solution

8.1 Introduction

The results of the previous chapter showed that it is possible to form CISe by combining a selenium polymer and metal precursor salts into one ink. This ink can then be used to directly form a PV material using extremely simple printing and processing techniques. In addition, it was discovered that it is possible to form these materials at 100 °C, which is a much lower temperature than previously thought possible. However, the process was not very reproducible and was prone to forming copper rich materials.

The next stage of this work focused on gaining a better understanding of how these materials form from the polymers and how to select metal precursors that have commensurate reactivates in order to improve the material stoichiometry. It has been shown that precursors with different reactivates have a profound effect on nanoparticle formation, especially in the case of CISSe, where the Cu precursors are typically much more reactive than the In precursors.[46,135] This is a consequence of the soft-acid nature of Cu^+, the comparatively hard-acid nature of In^{3+}, and the soft-base nature of organo-chalcogen compounds.[46] During the heat-up synthesis of metal-chalcogenide nanoparticles, the precursors will initially favor the formation of soft-acid to soft-base complexes and therefore will preferentially initially form copper-chalcogenide species.[46] Therefore, it is extremely important to find a slowly reacting copper precursor and a more reactive indium precursor. Moreover, it is well known that $Cu_2(S,Se)$ and Cu(S,Se) have a lower energy barrier of formation and therefore usually nucleate first.[81,136] Nanocrystal growth and thin-film formation is a non-equilibrium kinetic process and therefore the final material formation depends on the route taken through the various reaction pathways towards the end state and not necessarily the global thermodynamic minimum.[137] The crux of this problem is manifested as the formation of subspecies such as $Cu_2(S,Se)$ and $Cu(S,Se)$ at local thermodynamic minima during the reaction process before a lower energy $CuIn(S,Se)_2$ state is achieved. This issue is graphically depicted in **Figure 8.1**. The work in this chapter has aimed to investigate how selecting different metal precursors can help mitigate these issues. In addition, this work has investigated the feasibility of forming CISSe at such a low temperature, since it is possible that the thermodynamics at this temperature range prohibit the effective formation of CISSe, although encouragingly, it has been reported that it is possible to form CIS nanoparticles 100 °C or even at room temperature.[138]

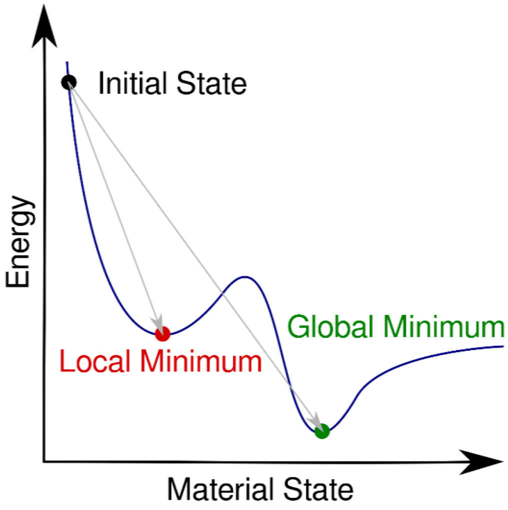

Figure 8.1: The route towards making CISSe with the polymers is kinetically limited, so it is possible to make secondary materials at a local thermodynamic minimum, instead of the desired material.

8.2 Methods

8.2.1 Solution Formulation

Sulfur polymer (PolyS), sulfoselenide polymer (PolySSe), or selenium polymer (PolySe) was dissolved in anhydrous toluene in an inert atmosphere glovebox (PolyS 49 mg, PolySSe 72 mg, PolySe 120 mg in 4mL). Copper precursors (CuCl, CuI, Cu(II)Nitrate, Cu(I)Acetate (Cu(I)Ac), Cu(II) Acetylacetonate (Cu(II)AcAc), each 0.125 mmol) and indium precursors ($InCl_3$,

InI_3, In(III)Nitrate, In(III)Acetate (In(III)Ac), In(III) Acetylacetonate (In(III)AcAc) 0.125 mmol) were dissolved in 4 mL anhydrous dimethylformamide (DMF) or 4 mL tetramethylethylenediamine (TMEDA) in an inert atmosphere glovebox. After dissolution, this solution of metals was immediately loaded into a syringe in the glovebox in order to avoid potential copper oxidation prior to the reaction due to aerial oxidation.

8.2.2 Nanoparticle Formation

The polymer was injected into a 20 mL vial held under dry nitrogen and heated to 100 °C with stirring at 900 rpm. The metal precursor solution was subsequently injected and the reaction proceeded for 4 h. Aliquots of the reaction solution were taken at 0, 2.5, 5, 10, 15, 20, 30, 60, and 120 min by drawing 0.5 mL of the reaction solution into a syringe and immediately diluting in 2.5 mL of a 1:1 mixture of tolune and DMF. The nanoparticle dispersion was cooled to room temperature and 10 mL of chloroform was added to dissolve any potential extra polymer.

8.2.3 Nanoparticle Isolation

This mixture was sonicated for 5 min and divided into two 9 mL fractions and pipetted into two teflon centrifuge tubes. The nanoparticles were centrifuged at 14k rpm for 30 mins. The reaction side products and extra polymer were decanted away, leaving the isolated nanoparticles behind. The nanoparticles were redispersed in 10 mL chloroform and centrifuged again 14k rpm for 30 mins. This process was repeated one more time to ensure that all of the excess polymer and reaction side products were removed. The final nanoparticles were dispersed in 3 mL chloroform and sonicated for 30 min. This dispersion was pipetted into a 4 mL vial and the nanoparticles were dried using a rotovap and a final high vacuum step. These dried nanoparticles were then dispersed in DMF at a concentration of 200 mg/mL, yielding a printable nanoparticle ink. These inks were dropcast onto a cleaned substrate in order to characterize the resulting particles.

8.3 Results and Discussion

A set of different metal precursors was chosen based on the types of precursors that have been used in the literature to make CISSe nanoparticles.[135,138,139] For the first stage, this work focused on examining the reactivity of various precursors with PolyS, since it is a simpler system to use in comparison to the PolySe or PolySSe. It was discovered that it is possible to grow nanoparticles using this method over the course of several hours. **Figure 8.2** shows representative UV-Vis spectra of the nanoparticles as they nucleate and grow over time for several different precursors. Not all of the data are included for the sake of brevity, but a selected amount is included here to give a general picture of the reactivity trends that are seen. **Table 8.1** summarizes the results from the metal precursor reactivity experiments and provides some general comments regarding specific issues or properties for each precursors. The reactivity of each precursor was grouped into one of three categories for comparison, by determining the time window within which colored nanoparticles were first seen. These categories are: **Fast** (0 – 10 min), **Medium** (10 – 30 min), and **Slow** (30 – 120 min). The only indium precursors that were reactive by themselves were In(III)nitrate and In(III)AcAc, where In(III)AcAc reacted much more quickly and could be seen forming nanoparticles within 30 min, whereas In(III)nitrate took 240 min to form some nanoparticles. In general, the iodide precursors reacted the slowest, the acetate and acetylacetonate precursors reacted the most quickly, while the chlorides and nitrates were somewhere in between. Moreover, it can be seen that the reactivity rate of the precursors is largely determined by the reactivity of the copper precursors, in that the rate of nanoparticle formation for the copper precursor only is very similar to the rate of nanoparticle formation with both the copper and indium

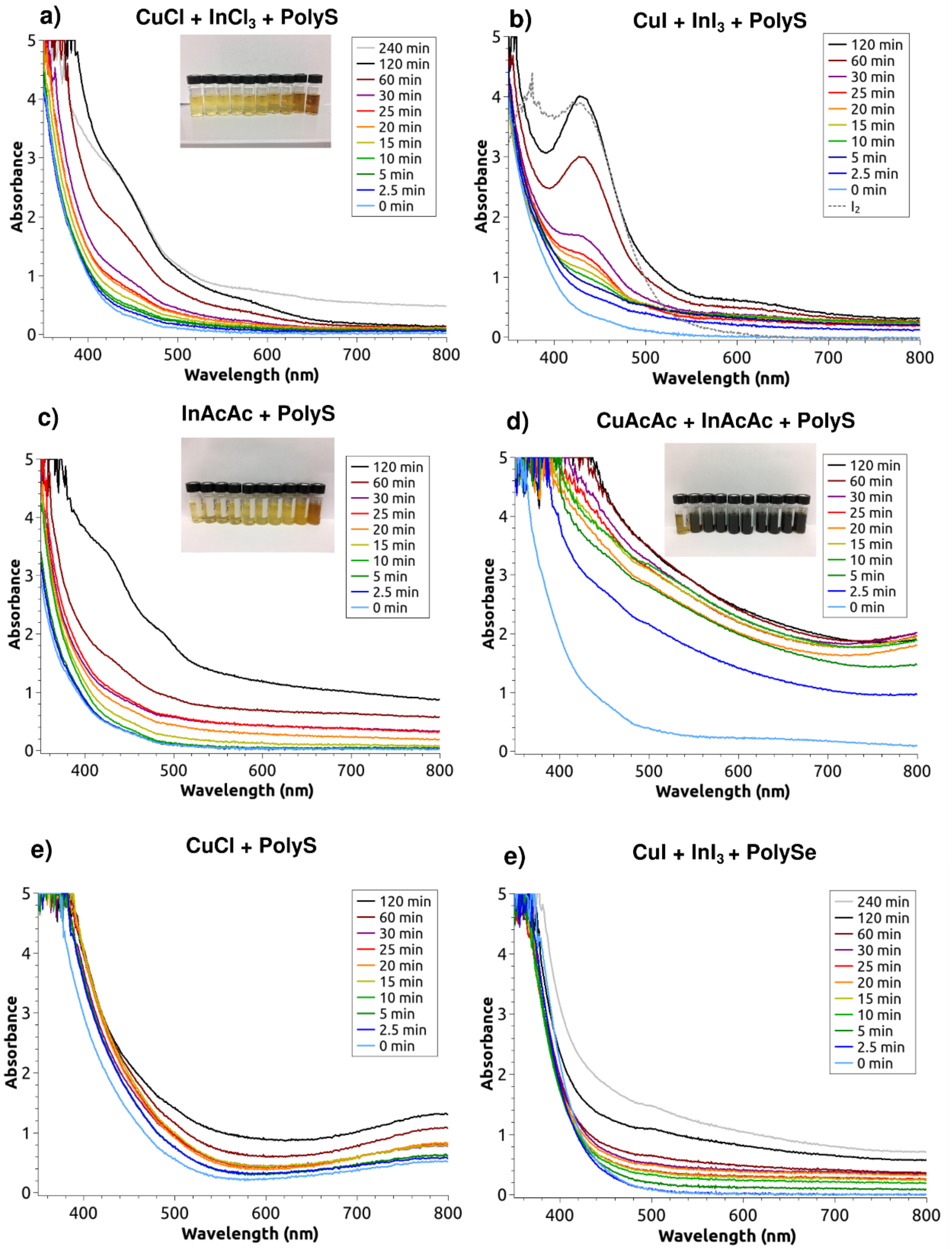

Figure 8.2: Selection of UV-Vis data examining the rate of nanoparticle growth with various metal precursors. Some graphs have insets showing how the color of the nanoparticles change over time. Note that a) and e) have extra data for 240 min and b) has an extra curve showing the absorbance of iodine for comparison.

Table 8.1: Comparison of metal precursor reactivity for individual precursors to form binary metal-chalcogenide nanoparticles as well as both metal precursors to form $CuIn(S,Se)_2$ nanoparticles

Precursor	Cu	In	Cu + In	Notes
Iodides CuI InI_3	**Slow**	None	**Slow**	CuI is the most stable Cu^+ precursor
Chlorides CuCl $InCl_3$	**Medium**	None	**Medium**	CuCl can disproportionate into Cu^{2+} and Cu^0 metal
Nitrates Cu(II) Nitrate In(III) Nitrate	**Medium**	**Slow**	**Medium**	Cu^{2+} is problematic for forming CISSe
Acetates Cu(I) Acetate In(III) Acetate	**Fast**	None	**Fast**	Cu^+ can readily oxidize to Cu^{2+}
Acetates Cu(II) Acetylacetoante In(III) Acetylacetoante	**Fast**	**Medium**	**Fast**	In(III) AcAc is by far the most reactive Indium precursor Cu^{2+} is problematic for forming CISSe

precursors. It is also important to note that Cu(II)nitrate and Cu(II)AcAc are not commercially available in the 1+ oxidation state. In addition, Cu(I)Ac and CuCl would change color in solution from clear to green or blue colored after approximately 24 h, indicating a switch from a +1 oxidation state to the +2 oxidation state. However, CuI was a stable clear solution indefinitely, further confirming that this is the most stable Cu^+ precursor.

For the iodide precursors, the UV-Vis data show a peak that increases in magnitude over time that aligns very well with the absorbance of iodine (I_2), which is presented in Figure 8.2b in addition to the nanoparticle data. This suggests that the iodine is evolved as the nanoparticles grow according to reaction presented in **Scheme 8.1**, where the iodide ions can reduce polymeric sulfur. It is important to note that it is not possible to monitor the reaction of the other precursors using UV-Vis in this manner, since the other anions do not form a colored byproduct, whereas iodine is

$$CuI + InI_3 + 2S^0 \longrightarrow Cu^+ + In^{3+} + 2S^0 + 4I^- \longrightarrow$$

$$Cu^+ + In^{3+} + 2S^{2-} + 2I_2 \longrightarrow CuInS_2 + 2I_2$$

Scheme 8.1: Proposed reaction scheme where iodide ions reduce sulfur and produce iodine as a reaction byproduct.

a colored byproduct that is easy to track. It is possible to see a shoulder that might be from iodine in Figure 8.2e with PolySe as a precursor, however since this reaction is much slower, the peak is difficult to resolve.

The next portion of this work focused on examining the properties of the nanoparticles made using the various metal precursors. As a first step, nanoparticles were made using Cu(I)Ac, In(III)AcAc, and PolyS, since these types of precursors were found to be the most reactive. Cu(I)Ac was used instead of Cu(II)AcAc since Cu^+ is required to form CIS nanoparticles. **Figure 8.3** shows SEM images of CIS nanoparticles that have been isolated and drop-cast onto a molybdenum coated glass substrate. The nanoparticles have a consistent spherical morphology and are approximately 100 nm in diameter. **Figure 8.4** shows the XRD pattern of these nanoparticle films, which is consistent with the formation of nanoscale CIS. **Figure 8.5** shows a representative EDS spectrum from the films, which shows that the particles have an are about 25% indium deficient. It is also important to note that the sulfur stoichiometry is difficult to deconvolute from the molybdenum signal and is therefore qualitative in nature only. **Figure 8.6** shows a Raman spectrum for the nanoparticle films, which confirms the formation of chalcopyrite structured CIS crystals and shows little or no discernable peaks from subspecies or residual polymer.

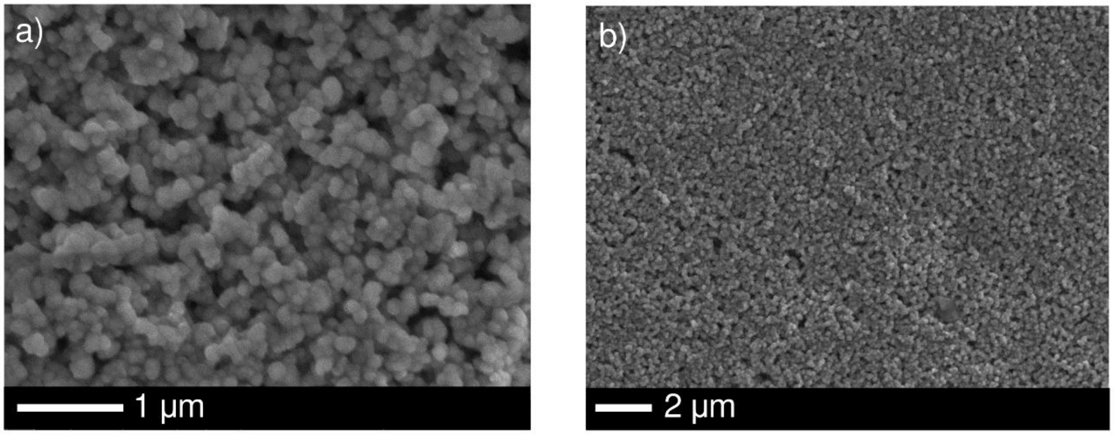

Figure 8.3: SEM images of $CuInS_2$ nanoparticles grown at 100 °C in solution using PolyS and dropcast onto a substrate. Decreasing magnification from a) to b).

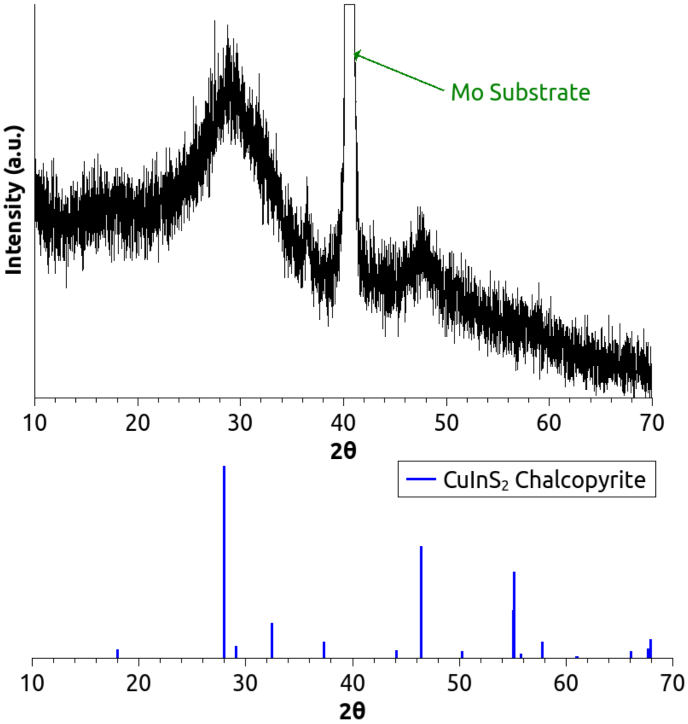

Figure 8.4: XRD pattern for $CuInS_2$ nanoparticles grown at 100 °C in solution using PolyS and dropcast onto a substrate.

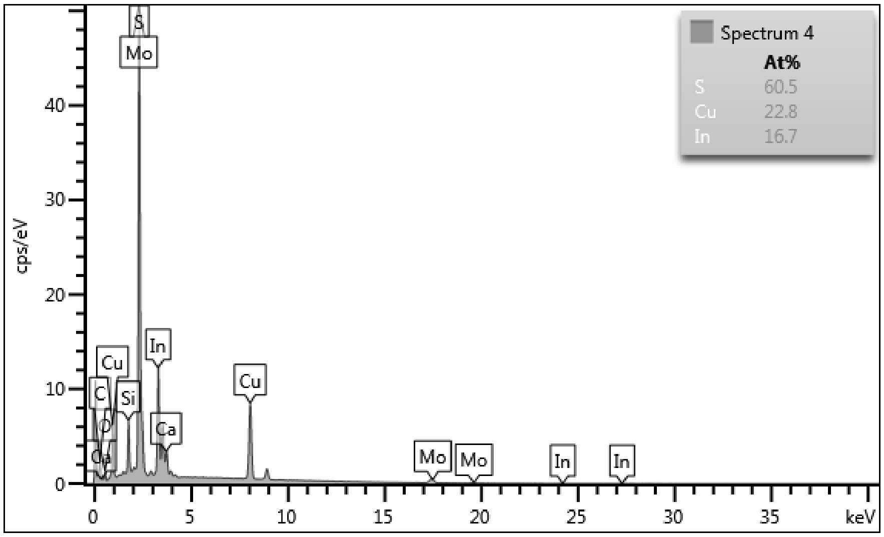

Figure 8.5: EDS spectrum for $CuInS_2$ nanoparticles grown at 100 °C in solution using PolyS and dropcast onto a substrate. Sulfur (S) stoichiometry is elevated due to signal overlap with molybdenum (Mo) coated soda-lime glass substrate. Silicon (Si), oxygen (O), and calcium (Ca) are from soda-lime glass. Carbon (C) is from residual material on the film and contamination of the instrument.

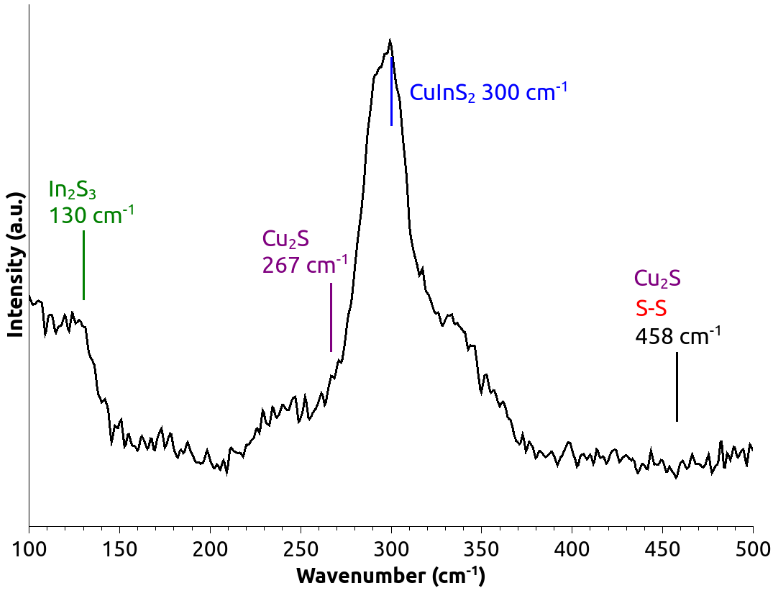

Figure 8.6: Raman spectrum for $CuInS_2$ nanoparticles grown at 100 °C in solution using PolyS and dropcast onto a substrate.

These results are extremely important since they prove that it is possible to make CIS at 100 °C using a chalcogen polymer with the type of structure that has been discussed in Chapters 6 and 7. The next steps for this project examined using PolySe to make nanoparticles using an analogous procedure, Cu(I)Ac, and In(III)AcAc, to see if it is possible to make CISe. The SEM images of the resulting CISe particle films shown in **Figure 8.7** show that there are some resulting nanoparticles that are formed, but they are also formed with an amorphous material. A representative EDS spectrum shown in **Figure 8.8** shows that these particles are very copper rich. These data indicate that although it is possible to form CIS particles that are somewhat copper rich, but close to the correct stoichiometry with PolyS, this stoichiometric issue becomes exacerbated when transitioning to PolySe. It is interesting to compare the stoichiometric data from Figure 8.8 with the data from Table 7.3, which are commensurate with each other. This suggests that a precursor reactivity imbalance has produced copper-rich materials in both instances, where the formation of CuSe is dominant.

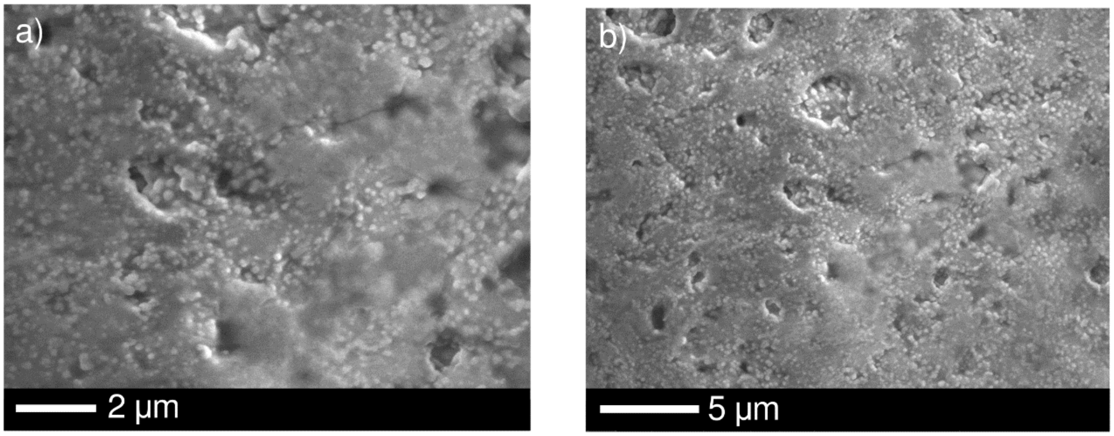

Figure 8.7: SEM images of nanoparticles grown at 100 °C in solution using PolySe and dropcast onto a substrate. Decreasing magnification from a) to b).

In order to attempt to address this issue, the results of the experiments that were presented in Table 8.1 were used to choose metals precursors that might mitigate the formation of copper-

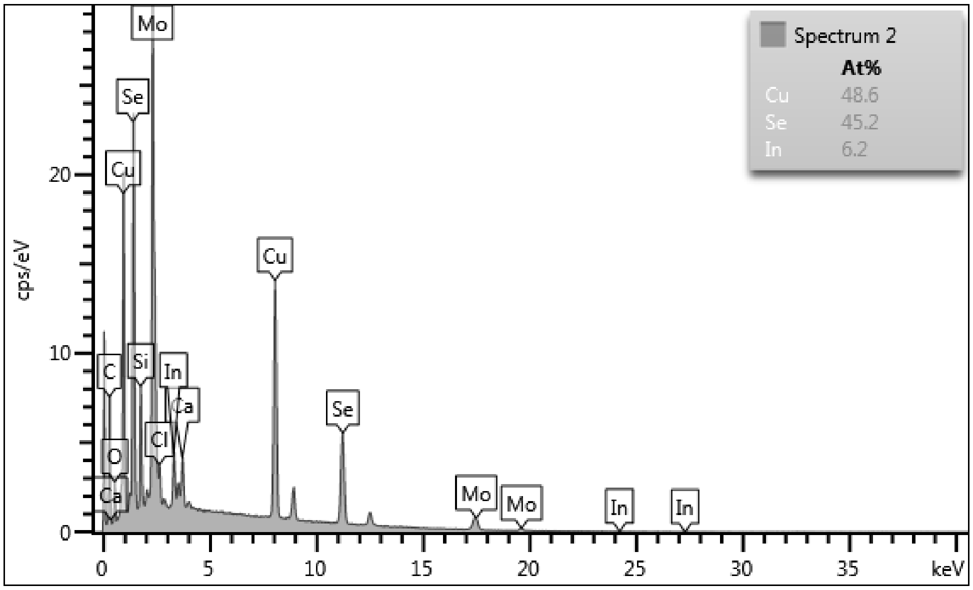

Figure 8.8: EDS spectrum for nanoparticles grown at 100 °C in solution using PolySe and dropcast onto a substrate. Molybdenum (Mo), Silicon (Si), oxygen (O), and calcium (Ca) are from soda-lime glass. Carbon (C) is from residual material on the film and contamination of the instrument.

rich materials. Specifically, nanoparticles were synthesized using copper iodide (CuI), Indium Acetylacetonate (In(III)AcAc), and PolySe. These precursors were chosen since it was discovered that CuI is the most stable Cu^+ precursor and is the slowest reacting copper precursor and In(III)AcAc was the most reactive indium precursor. There is some literature precedent for using CuI to synthesize CIS nanoparticles because of this issue, but very little investigation in the role of metal precursors for synthesizing CISe.[46,138,139] **Figure 8.9** shows the SEM images of the resulting films. The films show a large population of small nanoparticles that are within the range of 10 – 50 nm and a population of platelet-shaped nanoparticles that are much larger and are in the size range of 200 – 500 nm. A representative EDS spectrum of the films is shown in **Figure 8.10**. This spectrum shows that despite an attempt to optimize metal precursor reactivity, the films are still very copper rich and likely are mostly CuSe, since there is approximately a 1 to 1 stoichiometric ratio of Cu to Se. This is likely because although the data shown in Table 8.1 indicate that the CuI precursor reacts more slowly than the In(III)AcAc when they are

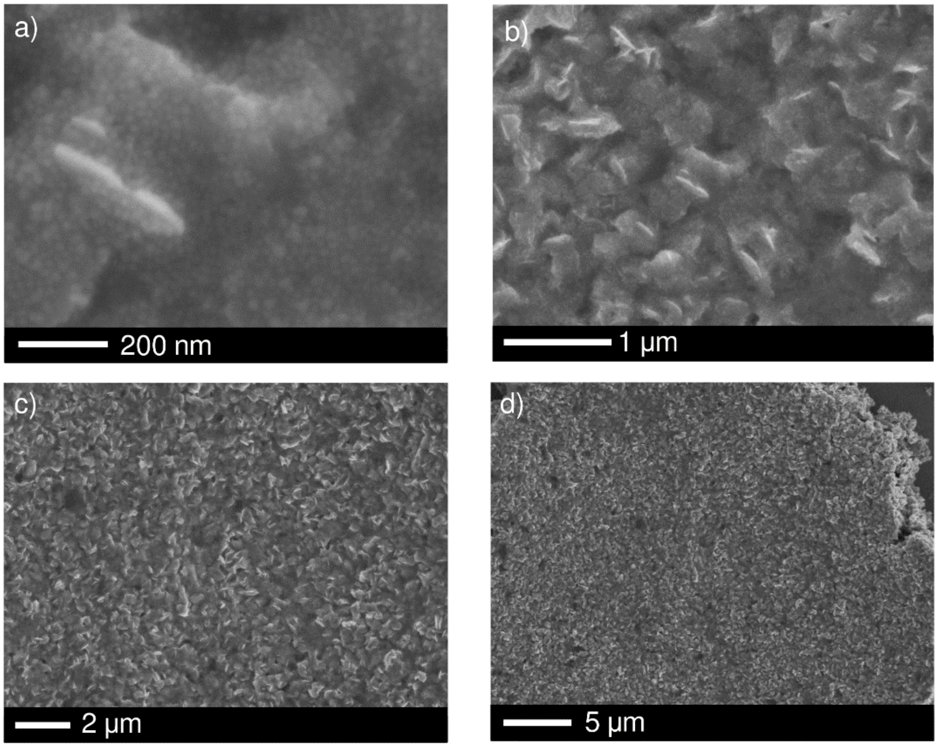

Figure 8.9: SEM images of nanoparticles grown at 100 °C in solution using PolySe, CuI, and In(III)AcAc and dropcast onto a substrate. Decreasing magnification from a), b), c) to d).

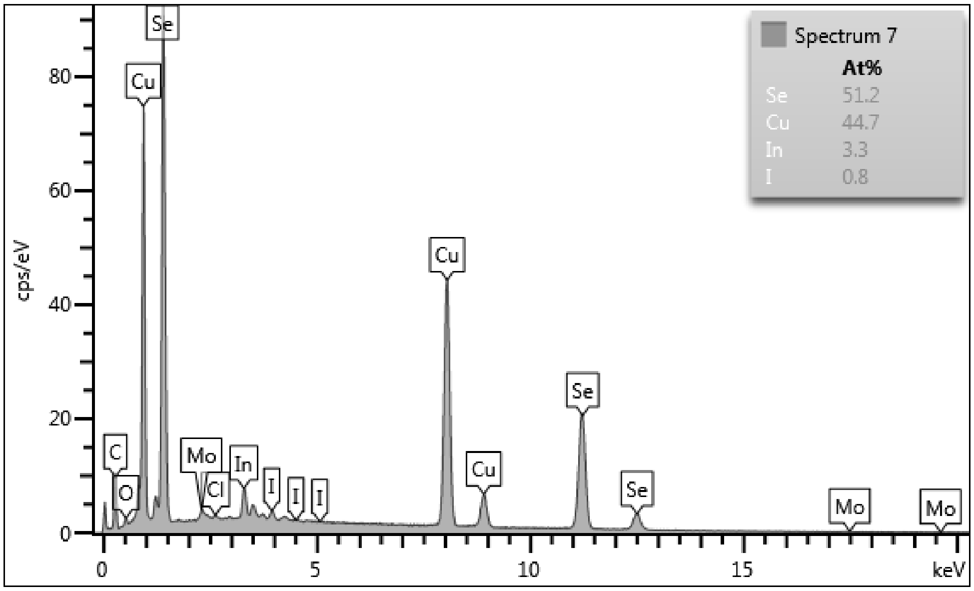

Figure 8.10: EDS spectrum for nanoparticles grown at 100 °C in solution using PolySe, CuI, and In(III)AcAc and dropcast onto a substrate. Molybdenum (Mo), Silicon (Si), oxygen (O), and calcium (Ca) are from soda-lime glass. Carbon (C) is from residual material on the film and contamination of the instrument. Note that the films also contain some residual iodine.

both reacted independently with PolyS, this is not necessarily also the case when PolySe is used and when both of the metal precursors are used in tandem. Unfortunately, this suggests that although tuning metal precursor reactivity is a valuable tool, it shows that a mismatch in precursor reactivity does not completely explain the issues that are at hand.

8.4 Conclusions and Future Work

It has been posited that tuning metal precursor reactivity is critical to forming stoichiometric CIS.[46,138,139] This work began by examining the reactivity rates of different metal precursors as a means to investigate and perhaps mitigate the formation of the copper rich materials that were seen in Chapter 7. This work then showed that by selecting an indium precursor with a higher rate of reactivity, it is possible to form CIS using PolyS at 100 °C, which is remarkable because it is a much lower temperature than previously thought possible. These results also serve to explain the formation of nanoparticles during the 100 °C drying step as seen in Figure 7.12 and help to explain some of the reproducibility issues that were seen in Chapter 7, since it is now apparent that nanoparticles were forming earlier on in the printing process than previously thought possible.

Unfortunately, when these same metal precursors were used to form CISe with the selenium polymer, the issue of forming copper rich materials became exacerbated, and the reaction mostly produced CuSe. This suggests that although tuning metal precursor reactivity is a valuable tool, it does not completely address the issues that were seen with the printed films in Chapter 7. It has been posited that when elemental sulfur is used as a chalcogen source, then there is an intermediary reaction step in which the sulfur is reduced to S^{2-} (which is often a rate-limiting step), which can then react with the metal cations to form a semiconducting material.[41,46,127] This is similar to the type of reaction that was posited in Scheme 8.1, in which the iodide anions were effectively reducing PolyS as an intermediary step to form CIS. This type of reaction would take the general form of what is proposed in **Scheme 8.2**:

$$\begin{aligned}&\mathrm{CuA} + \mathrm{InB_3} + 2\mathrm{S}^0 \longrightarrow \mathrm{Cu}^+ + \mathrm{In}^{3+} + 2\mathrm{S}^0 + \mathrm{A}^- + \mathrm{B}^{3-} \longrightarrow \\ &\mathrm{Cu}^+ + \mathrm{In}^{3+} + 2\mathrm{S}^{2-} + \mathrm{A} + \mathrm{B} \longrightarrow \mathrm{CuInS_2} + \mathrm{A} + \mathrm{B}\end{aligned}$$

Scheme 8.2: Proposed reaction scheme where the cations reduce sulfur as an intermediary step to produce CIS.

The results from this chapter suggest that this type of reaction happens to some extent and that this reaction takes place with the sulfur polymer. However, the results also suggest that the selenium atoms present in PolySe may not be as effectively reduced in comparison to the sulfur atoms from PolyS. It has been shown that selenium is typically less reactive than sulfur in a heat-up nanoparticle synthesis and that achieving effective selenium reduction is more challenging than in the case of sulfur.[46] It is important to consider that for the chalcogen polymer structures that were studied in Chapter 6, the vast majority of chalcogen atoms remain in a charge neutral state where linear chains of chalcogen atoms are linked together. Furthermore, it has been posited that forming reactive H_2Se and H_2S from elemental S and Se is a crucial intermediary step for nanoparticle formation and that H_2Se formation is more difficult to achieve than H_2S formation.[46] Therefore it is necessary for an intermediary reduction step and a cleavage of Se-Se bonds to take place in order to facilitate a reaction with the metal cations to form a semiconducting material and it is likely that this is more difficult in the case of PolySe. This information, when coupled with the results of this chapter, suggest that in the case of the selenium polymer, a more likely reaction pathway is one where the Se^0 atoms in PolySe are actually reduced by copper that oxidizes from Cu^+ to Cu^{2+}, which then reacts with the reduced selenium to form CuSe. This type of reaction pathway is also supported by the fact that the 100 °C nanoparticle synthesis with PolySe is often low yield (around 30% yield), which indicates that much of the metal precursors stay in solution as the species proposed in **Scheme 8.3**. Furthermore, this may be a reason why a clear iodine peak is seen in the case of Figure 8.2b and not in Figure 8.2e, since in the case of PolyS the iodide species are reducing the sulfur atoms and forming iodine as a byproduct, while in the case of PolySe, the reduction step is mainly occurring via copper oxidation, so a clear iodine evolution is not seen.

$$\begin{gathered} 2\mathrm{CuA} + \mathrm{InB_3} + \mathrm{Se^0} \longrightarrow 2\mathrm{Cu^+} + \mathrm{Se^0} + 2\mathrm{A^-} + \mathrm{InB_3} \longrightarrow \\ 2\mathrm{Cu^{2+}} + \mathrm{Se^{2-}} + 2\mathrm{A^-} + \mathrm{InB_3} \longrightarrow \mathrm{CuSe} + \mathrm{CuA_2} + \mathrm{InB_3} \end{gathered}$$

Scheme 8.3: Proposed reaction scheme where copper(I) is oxidized to copper(II) by selenium, which then reacts with copper(II) to form CuSe.

Although there are many studies that have been able to make CZTS and CIS nanoparticles with a Cu^{2+} precursor,[29,135] the Cu(II)nitrate and Cu(II)Ac precursors that were investigated in the study were problematic since they always formed CuSe and never CISe. This is likely because in a conventional nanoparticle synthesis the precursors are able to undergo an intermediary redox step where Cu^{2+} changes to Cu^{+}, which has been explicitly explored in the case of CZTS,[67] while in this case it is more favorable to directly form CuSe.

In order to produce printed films with improved metals stoichiometry, it is important to concurrently tune metal precursor reactivity and provide an efficient route for chalcogen reduction. This work has shown that CuI and In(III)AcAc provide the best balance of precursor reactivity, where CuI is the most stable and slowest reacting Cu^{+} precursor and In(III)AcAc is the most reactive indium precursor. The next phase of this work will need to investigate the options for directly reducing the chalcogen atoms in PolyS, PolySSe, and PolySe with some type of external reducing agent. It has been shown that effectively reducing the charge neutral chalcogen atoms is crucial for nanoparticle synthesis when elemental S or Se is used and that this is usually mediated by the primary amines that are used as a high temperature solvent and nanoparticle ligand.[41,46] In a similar manner, this technology will need to use an additional reducing agent that serves this role but that does not introduce the issues with large aliphatic-amine ligands that were discovered in Chapter 2.[47] Despite attempts at tuning metal precursor reactivity, analogous copper-rich stoichiometries were seen for the nanoparticles made in this chapter and the printed thin-films made in Chapter 7, so it is possible that both methods were hampered mainly by this non-ideal chalcogen reduction issue. Therefore, this means that the constraining issues of the previous chapter are not entirely a result of metal precursor reactivity imbalance or by the impeded species diffusion that occurs within the thin-films during nanoparticle growth and nucleation. Accordingly, it is likely that if the linear chains of chalcogen atoms in PolyS, PolySSe, and PolySe can be effectively reduced and broken down during the reaction, then printed thin-film morphology, stoichiometry, and reproducibility can be drastically improved.

An idealized printing scheme would resemble the process that is shown in **Scheme 8.4**, where the metal precursors are combined with a solvent and a reducing agent, which is then mixed with a chalcogen polymer solution immediately prior to printing. It has been demonstrated that polymers with similar structures can reversibly depolymerize yielding remaining monomers and small molecules.[140] In addition, it is known that the reduction of charge neutral chalcogen atoms and the generation of H_2S and H_2Se is facilitated by primary amines and is a necessary intermediary step for generating metal-chalcogenide nanoparticles.[41,46] Therefore, by selecting a primary amine that has a similar boiling point to the other solvents, such as pentylamine or ethylenediamine, then it may be possible to achieve the print scheme that is outlined in Scheme 8.4 and to efficiently produce CISSe nanoparticles from PolyS, PolySSe, and PolySe. It has been shown that these types of amines are also widely used to stabilize Cu^+ species, which is critical for producing high quality CISSe PV materials.[138]

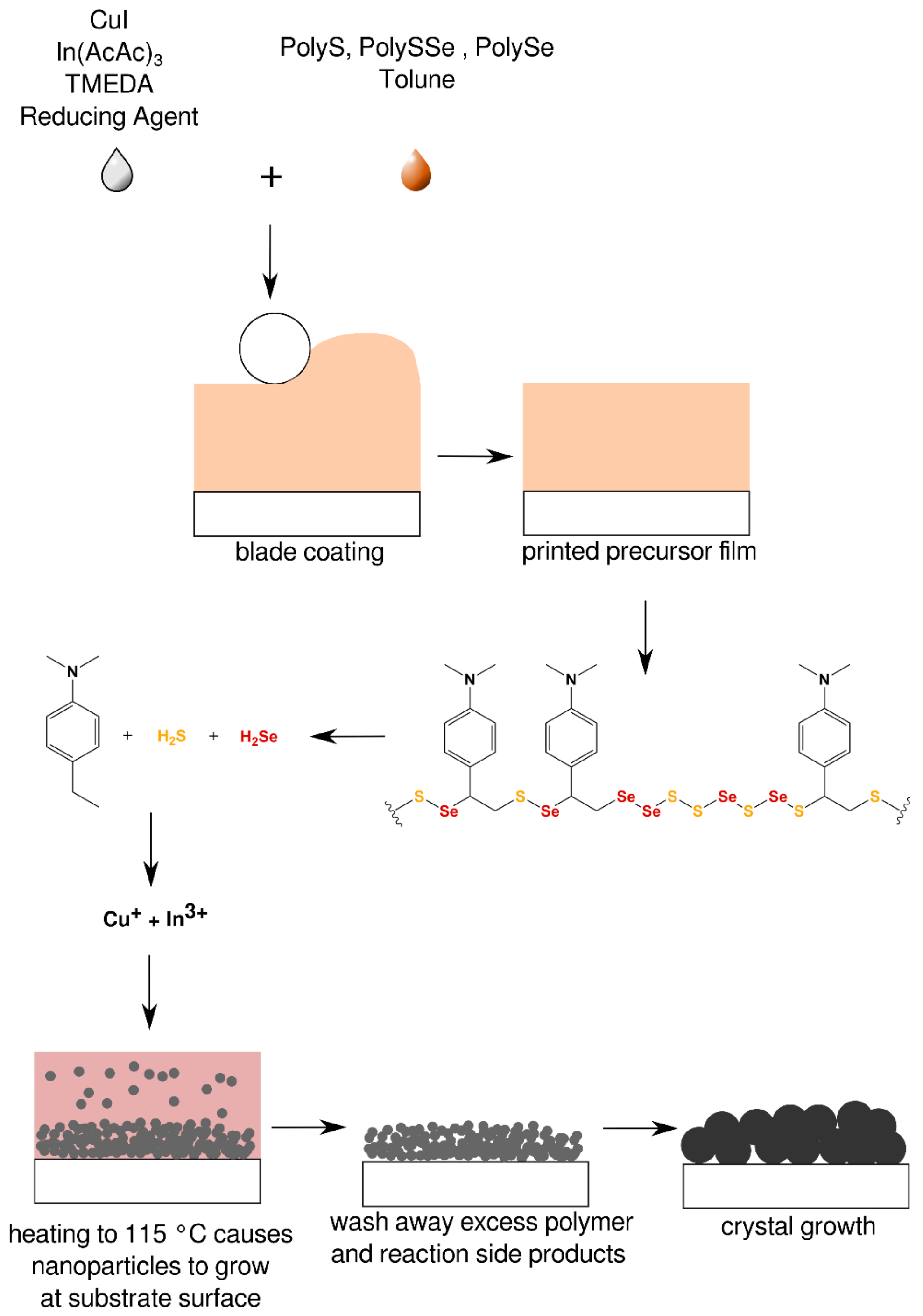

Scheme 8.4: Proposed printing scheme where the chalcogen polymers are broken down, reduced, and protonated by a reducing agent. The resulting H_2S and H_2Se will immediately react with the metal cations to form CISSe nanoparticles. Next, the excess polymer, monomers, and reaction side-products are washed away using an organic solvent. The bare nanoparticle thin-film that is left behind can then be annealed and sintered to produce a PV layer.

This work helped elucidate some of the reproducibility issues that were seen in Chapter 7. Specifically, it was discovered that the chalcogen polymers are much more reactive than previously thought and it was shown that it is possible to produce metal-chalcogenide nanoparticles at 100 °C using the chalcogen polymers. These results help to explain why copper-rich materials frequently form very early on in the printing process and resulted in the non-ideal film morphologies and stoichiometries seen in Chapter 7. Next, this work examined how tuning metal precursor reactivity is a helpful tool for making CISSe. It was also discovered that it is important to provide an efficient pathway for the linear chalcogen atoms in the polymers to be reduced, split apart, and protonated to create H_2S and H_2Se, which is a necessary intermediary reaction step for forming high-quality CISSe. If this can be achieved, then it is possible to directly print CISSe PV materials via a low-temperature, completely solution-processed, self-assembled method, with tunable S to Se stoichiometry to vary the material bandgap. This would be a tremendous achievement with a very viable pathway for future commercialization. Furthermore, it would help overcome the limitations of the conventional selenium vaporization technique, which despite its ubiquity and utility at the laboratory scale, has remained a major hurdle that has been hampering the commercialization of printed metal-chalocenide PV for almost a decade.

Chapter 9. Summary and Future Work

9.1 Summary and Research Accomplishments

This work began by examining the effects of conventional nanoparticle ligands on CZTS photovoltaic devices. It was discovered that conventional aliphatic ligands will undergo a pyrolysis reaction during annealing, which produces graphitic carbon doped with selenophene and thiophene moieties and is electrically conductive. It was also discovered that the OLA ligand improves PV devices by forming a more ordered graphitic material that more readily phase separates from the CZTS nanoparticles because of their increased reactivity and via the formation of an intermediary network polymer.[47] Specifically, this work posited that the OLA ligands react with the chalcogens at the double-bond and form a network polymer that promotes CZTS nanoparticle aggregation and crystal growth.[47]

Using this information as a starting point, the next phase of this work focused on developing a new nanoparticle synthesis method that circumvents the issues associated with conventional aliphatic ligands and that mirrors some of the advantages of the OLA ligands within the context of a new synthesis paradigm. First, a novel sulfur copolymer that remains a liquid at elevated temperatures was developed using reactions based on what was seen with sulfur and OLA.[100] This sulfur copolymer was used both as a sulfur source and a high-temperature solvent to synthesize CdS nanoparticles in solution.[100,141] Next, it was shown that the sulfur copolymer could be removed from the nanoparticles, thereby yielding CdS nanoparticles that did not have conventional organic ligands.[100,141]

Before producing more complicated materials such as CIGS and CZTS, this method was next used to produce CIS nanoparticles. It was shown that this sulfur copolymer synthesis method can be used to print CIS nanoparticle films that undergo exceptional crystal growth to produce highly crystalline CISe when annealed in the presence of selenium vapor at 500 °C.

Using these results as another starting point, a novel selenium sulfide terpolymer was developed. This terpolymer was similarly used to produce CISSe nanoparticles. Although this method proved useful for making sulfo-selenide polymers, it was discovered that a new polymer chemistry would need to be developed in order to make a selenium-only polymer.

The next phase of this work focused on developing an improved chalcogen polymer structure and synthesis methodology, in order to produce both sulfur polymers and selenium polymers, as well as polymers with a range of sulfur to selenium ratios, in order to be able to tune PV material bandgap. Moreover, these new chalcogen polymer structures employ ternary amine moieties, which allows them to coordinate with metal cations and allows the polymers to be miscible with metal precursor salts.

With these improved polymer structures, it is possible to formulate one ink that contains all of the necessary components to directly form a CISSe PV material with simple printing methods. The next phase of this work utilized the selenium polymer to directly form opto-electronic quality CISe thin-films using completely solution-processed methods, which has not been previously demonstrated.

The next phase of this work investigated the reaction kinetics of different metal precursors when combined with the chalcogen polymers in order to help understand the material formation process and improve thin-film reproducibility. It was discovered that selecting the slowest and most stable Cu^+ precursor (CuI) and the most reactive In^{3+}(In(III)AcAc) may be a helpful tool for forming CISSe. It was also proven that CIS particles can be readily formed at 100 °C, which provides a route for low-temperature processing. However, it was also discovered that although tuning metal precursor reaction kinetics is beneficial, making CISe remains challenging since the polymer is not effectively broken down and reduced prior to reacting with the metal precursors, which is an important intermediary step for forming high quality materials. Accordingly, if an appropriate reducing agent can be implemented, then it is possible that the properties of the resulting nanoparticles and printed thin-films can improve drastically.

Finally, it was shown that this ink provides a viable pathway towards producing completely solution-processed, low-temperature CISSe films (Scheme 8.4) with tunable bandgaps, which has not been previously demonstrated. If thin-film PV materials can be produced using cheap, scalable methods such as low-temperature annealing and solution-based processing, then PV deployment could be rapidly accelerated due to the drastically lower CAPEX levels afforded by such simplified production methods.

Overall, the opportunities that this technology affords are compelling for various uses, including for PV applications. There are several things that can be uniquely achieved by this technology:

- Highly reactive, stable, readily printable chalcogen polymers with tunable S to Se ratios
- Directly make chalcogenide nanoparticles without conventional ligands
- Chalcogen polymers are miscible with metal precursors and can coordinate with metal cations
- An ink containing all of the necessary components for directly producing CISSe using extremely simple printing methods
- Self-assembled CISSe materials using a benchmark low temperature of 115 °C
- Simple and efficient removal of excess reactants and impurities from high-quality films

As a result of these very promising attributes, this work has produced a series of intellectual property filings, which has culminated in the submission of an international patent filing (see

Appendix B).

9.2 Future Directions

9.2.2 Device Fabrication

If an effective reducing agent can be found, then the next stage of this work will likely focus on developing complete PV devices, using a device architecture that is analogous to what was used in the CZTS study. **Figure 9.1** shows the device architecture that will be implemented for these devices.

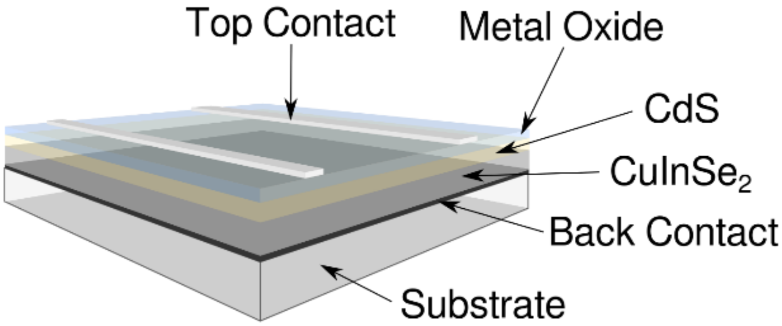

Figure 9.1: Structure of future PV devices based on a CISe absorber layer that is printed using nanoparticles grown with a selenium polymer. The CISe is printed on top of molybdenum coated (back contact) soda lime glass and is topped with RF sputtered ZnO and ITO passivation/conduction layers. Thermally evaporated aluminum top contact traces complete the device.

9.2.3 Bilayer Printing Methods

In addition to using PolySe to synthesize chalcogenide nanoparticles, the polymer has a potentially promising application as a novel printed selenium precursor in its own right. For example, a metal-sulfide layer could be printed onto a substrate using well-established techniques.[67,124] This bilayer film could then be annealed, and the metal precursors would react with the selenium in the PolySe film to produce the final absorber layer (**Figure 9.2**). This method

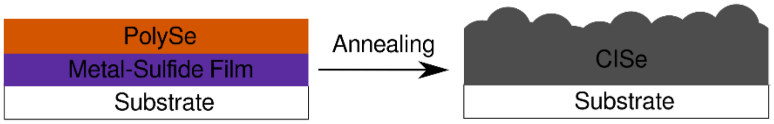

Figure 9.2: Method for making chalcogenide PV films by printing PolySe on top of a printed metal-sulfide film.

is particularly promising since it would eliminate the selenium vapor-phase reaction step in a very simply way, which is very difficult to control and is not amenable to scale-up. However, the necessity that the metal sulfide material engages in a chemical reaction with the polymer while in film form could prove to be problematic. It is possible that the PolySe films may have a propensity to decompose or volatilize before completely reacting.

Another option is to use this bilayer structure as a way to directly produce CISSe thin films without forming intermediary metal-sulfides (**Figure 9.3**). Instead of mixing the metal precursors and the chalcogen polymer together in one ink, this method would use two separate inks for the polymers and the metal precursors. The polymer films would be printed on top of a metal precursor film and then heated to begin the reaction. This method could be a useful way to increase the thickness of the printed films or to improve surface coverage. Some preliminary studies were conducted in both of these research areas, but the results were not conclusive enough yet to provide a clear picture of the details of the system. Further studies are currently underway.

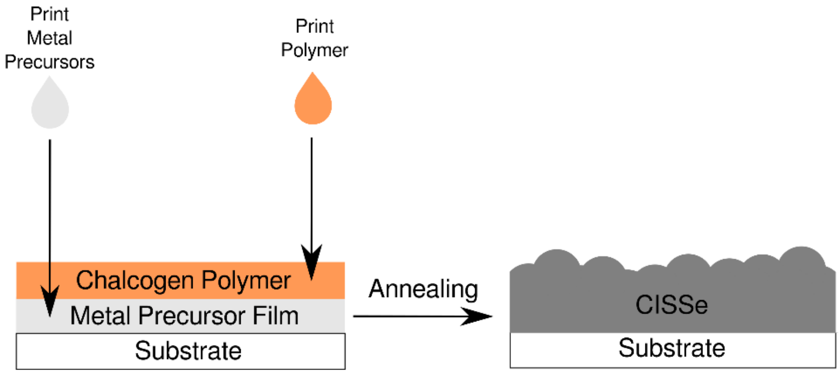

Figure 9.3: Method for making chalcogenide PV films by printing polymers on top of a printed metal precursor film.

9.2.4 Printing on Flexible Plastic Substrates

If there are successes with fabricating devices according to the architecture illustrated in Figure 9.1, another idea that could be implemented in the future is to produce CISe films on top of flexible plastic substrates. Since this method provides a pathway for low temperature processing, this process would be analogous to what is shown in Scheme 8.4. This concept would provide an excellent means to highlight some of the advantages of this system, and has not been previously accomplished for inorganic films. Moreover, it would provide a unique opportunity to prove the viability of scaling up this technology. **Figure 9.4** shows an example of the type of roll-to-roll printer that could be used to fabricate these types of devices. Since roll-to-roll processing requires a flexible thin-film, the nature of this polymer technology affords unique opportunities for this type of fabrication. For example, a brittle, crystalline material such as CISSe will crack and delaminate on a curved flexible substrate. This technology however, could be used to print a flexible polymeric thin-film that could be heated to 115 °C at a later stage when the substrate is configured in a flat module position to form the CISSe materials, thereby avoiding any potential issues with cracking and delamination and providing a viable method for roll-to-roll printing for these types of materials.

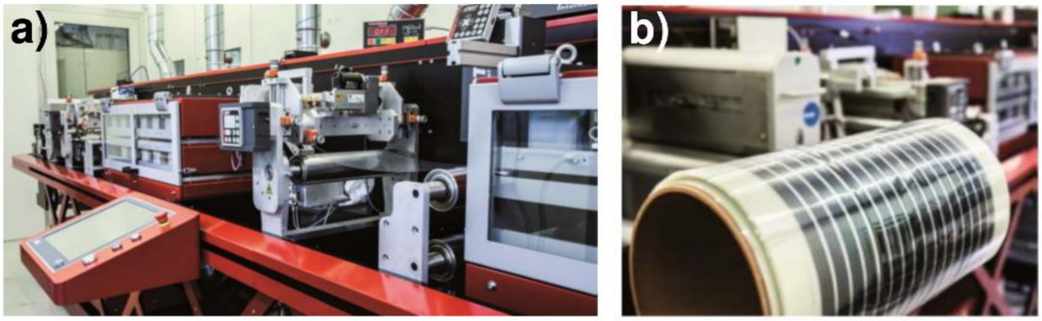

Figure 9.4: Images of roll-to-roll printing system located at the University of Washington Clean Energy Institute Testbed Facility. a) roll-to-roll printer b) close-up image of printed material on flexible plastic substrate. Photos courtesy of Michael Pomfret.

6.2.8 CIGSe and CZTSe Fabrication

If the methods described herein prove to be successful for CISe, then the next logical extension of this work would return to producing CZTSe as well as CIGSe materials for related PV applications. CZTSe is an interesting alternative since it consists of cheap, readily available metals, in contrast to CISe and CIGSe which require indium, which is a comparatively rare and expensive material and suffers from uncertainty due to price volatility. The CIGSe alloy is also an interesting candidate if CISe devices can be made, due to its record efficiencies and prominence within the PV industry.

6.3 Concluding Remarks

The methods described herein constitute a novel and promising route towards making low CAPEX photovoltaics using new chalcogen-based polymers and new nanoparticle synthesis methods that were developed during the course of this work. In addition, the foundational components of this work helped to elucidate the nature and role of carbon impurities in sintered nanoparticle based devices, which despite other related studies, had not been previously understood. The method for making nanoparticles without conventional aliphatic ligands can prove to be useful in a range of fields beyond PV, where the presence of these conventional ligands is otherwise detrimental for various applications. Moreover, these chalcogen polymers provide a route towards producing high-performance PV materials via a simple printing procedure that is completely solution processed and uses low temperatures.

In many ways, this work can be considered the unique combination of the realm of printed polymeric materials and the realm of inorganic photovoltaic materials. Polymer based devices are readily amenable to solution-processing and low-temperature fabrication, but remain hampered by intrinsic physical limitations such as dielectric properties that lead to high exciton binding energies. Inorganic based devices however, benefit from intrinsic physical advantages such as the formation of free charge carriers due to superior dielectric properties, but remain extremely difficult to process using solution based methods and low temperatures. This work constitutes one of the few studies that promises to fully combine the advantages of both of these paradigms.

References

(1) Myers, N.; Kent, J. New Consumers: The Influence of Affluence on the Environment. *Proc. Natl. Acad. ...* **2003**, *100*, 4963–4968.

(2) Kamat, P. V. Meeting the Clean Energy Demand: Nanostructure Architectures for Solar Energy Conversion. *J. Phys. Chem. C* **2007**, *111*, 2834–2860.

(3) Lewis, N.; Nocera, D. Powering the Planet: Chemical Challenges in Solar Energy Utilization. *Proc. Natl. ...* **2006**, *103*, 15729–15735.

(4) Campbell, C. Petroleum and People. *Popul. Environ.* **2002**, *24*, 193–207.

(5) Shafiee, S.; Topal, E. When Will Fossil Fuel Reserves Be Diminished? *Energy Policy* **2009**, *37*, 181–189.

(6) Lopez, A.; Roberts, B.; Heimiller, D.; Blair, N.; Porro, G. U . S . Renewable Energy Technical Potentials : A GIS-Based Analysis. *Natl. Renew. Energy Lab.* **2012**, No. July.

(7) Shah, A.; Torres, P.; Tscharner, R.; Wyrsch, N.; Keppner, H. Photovoltaic Technology: The Case for Thin-Film Solar Cells. *Science* **1999**, *285*, 692–698.

(8) Denholm, P.; Margolis, R. M. Land-Use Requirements and the per-Capita Solar Footprint for Photovoltaic Generation in the United States. *Energy Policy* **2008**, *36*, 3531–3543.

(9) Espinosa, N.; Hösel, M.; Angmo, D.; Krebs, F. C. Solar Cells with One-Day Energy Payback for the Factories of the Future. *Energy Environ. Sci.* **2012**, *5*, 5117.

(10) Arias, A. C.; MacKenzie, J. D.; McCulloch, I.; Rivnay, J.; Salleo, A. Materials and Applications for Large Area Electronics: Solution-Based Approaches. *Chem. Rev.* **2010**, *110*, 3–24.

(11) Turner, J. a. A Realizable Renewable Energy Future. *Science* **1999**, *285*, 687–689.

(12) Krebs, F. C.; Tromholt, T.; Jørgensen, M. Upscaling of Polymer Solar Cell Fabrication Using Full Roll-to-Roll Processing. *Nanoscale* **2010**, *2*, 873–886.

(13) Nelson, J. The Physics of Solar Cells; Imperial College Press, 2002; pp 24–39.

(14) Nelson, J. The Physics of Solar Cells; Imperial College Press, 2002; pp 64–69.

(15) Feldman, D.; Margolis, R.; Chung, D.; Fu, R.; Nrel, C. D.; Barbose, G.; Bolinger, M.; Seel, J.; Wiser, R.; Berkeley, L. Photovoltaic System Pricing Trends. *U.S. Dep. Energy* **2015**, No. August, 35.

(16) Chung, D.; Davidson, C.; Fu, R.; Ardani, K.; Margolis, R. U . S . Photovoltaic Prices and Cost Breakdowns : Q1 2015 Benchmarks for Residential , Commercial , and Utility-Scale Systems. *Natl. Renew. Energy Lab.* **2015**, No. September.

(17) Reichelstein, S.; Yorston, M. The Prospects for Cost Competitive Solar PV Power. *Energy Policy* **2013**, *55*, 117–127.

(18) Bazilian, M.; Onyeji, I.; Liebreich, M.; MacGill, I.; Chase, J.; Shah, J.; Gielen, D.; Arent, D.; Landfear, D.; Zhengrong, S. Re-Considering the Economics of Photovoltaic Power. *Renew. Energy* **2013**, *53*, 329–338.

(19) Lewis, N. S. Toward Cost-Effective Solar Energy Use. *Science* **2007**, *315*, 798–801.

(20) Ma, O.; Capanna, S.; Joseck, F.; Nathwani, J.; Nguyen, T.; Richard, C.; Spitsen, P.; Boyd, L.; Marcy, C.; Doe, E.; Davis, J.; Esterly, S.; Feldman, D.; Fu, R.; Johnson, C.; Lantz, E.; Livecchi, A.; Logan, J.; Mooney, D.; Newmark, R.; Porro, G.; Schwabe, P.; Smith, A.; Tian, T.; Williams, T.; Wipke, K. 2014 Renewable Energy Data Book. *Natl. Renew. Energy Lab.* **2014**.

(21) Powell, D. M.; Fu, R.; Horowitz, K.; Basore, P. A.; Woodhouse, M.; Buonassisi, T. The Capital Intensity of Photovoltaics Manufacturing: Barrier to Scale and Opportunity for Innovation. *Energy Environ. Sci.* **2015**, *8*, 3395–3408.

(22) Fthenakis, V. Sustainability of Photovoltaics: The Case for Thin-Film Solar Cells. *Renew. Sustain. Energy Rev.* **2009**, *13*, 2746–2750.

(23) Chopra, K. L.; Paulson, P. D.; Dutta, V. Thin-film Solar Cells: An Overview. *Prog. Photovoltaics Res. Appl.* **2004**, *12*, 69–92.

(24) Feltrin, A.; Freundlich, A. Material Considerations for Terawatt Level Deployment of Photovoltaics. *Renew. Energy* **2008**, *33*, 180–185.

(25) Wadia, C. Materials Availability Expands the Opportunity for Large-Scale Photovoltaics Deployment. *Environ. Sci. …* **2009**, *43*, 2072–2077.

(26) Goodrich, A.; Hacke, P.; Wang, Q.; Sopori, B.; Margolis, R.; James, T. L.; Woodhouse, M. A Wafer-Based Monocrystalline Silicon Photovoltaics Road Map: Utilizing Known Technology Improvement Opportunities for Further Reductions in Manufacturing Costs. *Sol. Energy Mater. Sol. Cells* **2013**, *114*, 110–135.

(27) Akhavan, V. A.; Goodfellow, B. W.; Panthani, M. G.; Steinhagen, C.; Harvey, T. B.; Stolle, C. J.; Korgel, B. A. Colloidal CIGS and CZTS Nanocrystals: A Precursor Route to Printed Photovoltaics. *J. Solid State Chem.* **2012**, *189*, 2–12.

(28) Bucherl, C. N.; Oleson, K. R.; Hillhouse, H. W. Thin Film Solar Cells from Sintered Nanocrystals. *Curr. Opin. Chem. Eng.* **2013**, *2*, 168–177.

(29) Guo, Q.; Hillhouse, H. W.; Agrawal, R. Synthesis of Cu_2ZnSnS_4 Nanocrystal Ink and Its Use for Solar Cells. *J. Am. Chem. Soc.* **2009**, *131*, 11672–11673.

(30) Hillhouse, H. W.; Beard, M. C. Solar Cells from Colloidal Nanocrystals: Fundamentals, Materials, Devices, and Economics. *Curr. Opin. Colloid Interface Sci.* **2009**, *14*, 245–259.

(31) Guo, Q.; Ford, G. M.; Yang, W. C.; Walker, B. C.; Stach, E. a; Hillhouse, H. W.; Agrawal, R. Fabrication of 7.2% Efficient CZTSSe Solar Cells Using CZTS Nanocrystals. *J. Am. Chem. Soc.* **2010**, *132*, 17384–17386.

(32) Mitzi, D. B.; Gunawan, O.; Todorov, T. K.; Wang, K.; Guha, S. The Path towards a High-Performance Solution-Processed Kesterite Solar Cell. *Sol. Energy Mater. Sol. Cells* **2011**, *95*, 1421–1436.

(33) Talapin, D. V.; Lee, J.-S.; Kovalenko, M. V.; Shevchenko, E. V. Prospects of Colloidal Nanocsrystals for Electronic and Optoelectronic Applications. *Chem. Rev.* **2010**, *110*, 389–458.

(34) Polizzotti, A.; Repins, I. L.; Noufi, R.; Wei, S.-H.; Mitzi, D. B. The State and Future Prospects of Kesterite Photovoltaics. *Energy Environ. Sci.* **2013**, *6*, 3171–3182.

(35) Zhou, H.; Hsu, W.-C.; Duan, H.-S.; Bob, B.; Yang, W.; Song, T.-B.; Hsu, C.-J.; Yang, Y. CZTS Nanocrystals: A Promising Approach for next Generation Thin Film Photovoltaics. *Energy Environ. Sci.* **2013**, *6*, 2822–2838.

(36) Qijie Guoa, Grayson M. Ford, Wei-Chang Yang, Charles J. Hages, Hugh W. Hillhouse, R. A. Enhancing the Performance of CZTSSe Solar Cells with Ge Alloying. *Sol. Energy Mater. Sol. Cells* **2012**, *105*, 132–136.

(37) Wei, H.; Ye, Z.; Li, M.; Su, Y.; Yang, Z.; Zhang, Y. Tunable Band Gap $Cu_2ZnSnS_{4x}Se_{4(1-x)}$ Nanocrystals: Experimental and First-Principles Calculations. *CrystEngComm* **2011**, *13*, 2222–2226.

(38) Ford, G. M.; Guo, Q.; Agrawal, R.; Hillhouse, H. W. Earth Abundant Element Cu2Zn(Sn1-xGex)S4 Nanocrystals for Tunable Band Gap Solar Cells: 6.8% Efficient Device Fabrication. *Chem. Mater.* **2011**, *23*, 8.

(39) Joo, J.; Na, H.; Yu, T.; Yu, J.; Kim, Y. Generalized and Facile Synthesis of Semiconducting Metal Sulfide Nanocrystals. *J. Am. Chem. Soc.* **2003**, *125*, 11100–11105.

(40) Mourdikoudis, S.; Liz-Marzán, L. M. Oleylamine in Nanoparticle Synthesis. *Chem. Mater.* **2013**, *25*, 1465–1476.

(41) Thomson, J. W.; Nagashima, K.; MacDonald, P. M.; Ozin, G. A. From Sulfur-Amine Solutions to Metal Sulfide Nanocrystals: Peering into the Oleylamine-Sulfur Black Box. *J. Am. Chem. Soc.* **2011**, *133*, 5036–5041.

(42) Tao, A. R.; Habas, S.; Yang, P. Shape Control of Colloidal Metal Nanocrystals. *Small* **2008**, *4*, 310–325.

(43) Yin, Y.; Alivisatos, A. P. Colloidal Nanocrystal Synthesis and the Organic-Inorganic Interface. *Nature* **2005**, *437*, 664–670.

(44) Huang, F.; Zhang, H.; Banfield, J. F. Two-Stage Crystal-Growth Kinetics Observed during Hydrothermal Coarsening of Nanocrystalline ZnS. *Nano Lett.* **2003**, *3*, 373–378.

(45) Dushkin, C. .; Saita, S.; Yoshie, K.; Yamaguchi, Y. The Kinetics of Growth of Semiconductor Nanocrystals in a Hot Amphiphile Matrix. *Adv. Colloid Interface Sci.* **2000**, *88*, 37–78.

(46) Van Embden, J.; Chesman, A. S. R.; Jasieniak, J. J. The Heat-Up Synthesis of Colloidal Nanocrystals. *Chem. Mater.* **2015**, *27*, 2246–2285.

(47) Martin, T. R.; Katahara, J. K.; Bucherl, C. N.; Krueger, B. W.; Hillhouse, H. W.; Luscombe, C. K. Nanoparticle Ligands and Pyrolized Graphitic Carbon in CZTSSe Photovoltaic Devices. *Chem. Mater.* **2016**, *28*, 135–145.

(48) Rosen, E. L.; Buonsanti, R.; Llordes, A.; Sawvel, A. M.; Milliron, D. J.; Helms, B. A. Exceptionally Mild Reactive Stripping of Native Ligands from Nanocrystal Surfaces by Using Meerwein's Salt. *Angew. Chemie Int. Ed.* **2012**, *51*, 684–689.

(49) Anderson, N. C.; Hendricks, M. P.; Choi, J. J.; Owen, J. S. Ligand Exchange and the Stoichiometry of Metal Chalcogenide Nanocrystals: Spectroscopic Observation of Facile Metal-Carboxylate Displacement and Binding. *J. Am. Chem. Soc.* **2013**, *135*, 18536–18548.

(50) Owen, J. S.; Park, J.; Trudeau, P. E.; Alivisatos, A. P. Reaction Chemistry and Ligand Exchange at Cadmium-Selenide Nanocrystal Surfaces. *J. Am. Chem. Soc.* **2008**, *130*, 12279–12281.

(51) Lokteva, I.; Radychev, N.; Witt, F.; Borchert, H.; Parisi, J.; Kolny-Olesiak, J. Surface Treatment of CdSe Nanoparticles for Application in Hybrid Solar Cells: The Effect of Multiple Ligand Exchange with Pyridine. *J. Phys. Chem. C* **2010**, *114*, 12784–12791.

(52) Tosun, B. S.; Chernomordik, B. D.; Gunawan, A. a; Williams, B.; Mkhoyan, K. A.; Francis, L. F.; Aydil, E. S. Cu_2ZnSnS_4 Nanocrystal Dispersions in Polar Liquids. *Chem. Commun. (Camb).* **2013**, *49*, 3549–3551.

(53) Cossairt, B. M.; Juhas, P.; Billinge, S.; Owen, J. S. Tuning the Surface Structure and Optical Properties of CdSe Clusters Using Coordination Chemistry. *J. Phys. Chem. Lett.* **2011**, *2*, 3075–3080.

(54) Zhou, H.; Song, T.-B.; Hsu, W.-C.; Luo, S.; Ye, S.; Duan, H.-S.; Hsu, C.-J.; Yang, W.; Yang, Y. Rational Defect Passivation of Cu2ZnSn(S,Se)4 Photovoltaics with Solution-Processed Cu2ZnSnS4:Na Nanocrystals. *J. Am. Chem. Soc.* **2013**, *135*, 15998–16001.

(55) Guo, Q.; Ford, G. M.; Agrawal, R.; Hillhouse, H. W. Ink Formulation and Low-Temperature Incorporation of Sodium to Yield 12% Efficient Cu(In,Ga)(S,Se)$_2$ Solar Cells from Sulfide Nanocrystal Inks. *Prog. Photovoltaics Res. Appl.* **2013**, *21*, 64–72.

(56) Collord, A. D.; Xin, H.; Hillhouse, H. W. Combinatorial Exploration of the Effects of Intrinsic and Extrinsic Defects in Cu$_2$ZnSn(S,Se)$_4$. *Photovoltaics, IEEE J.* **2015**, *5*, 288–298.

(57) Jang, J.; Dolzhnikov, D. S.; Liu, W.; Nam, S.; Shim, M.; Talapin, D. V. Solution-Processed Transistors Using Colloidal Nanocrystals with Composition-Matched Molecular "Solders": Approaching Single Crystal Mobility. *Nano Lett.* **2015**, *15*, 6309–6317.

(58) Dolzhnikov, D. S.; Zhang, H.; Jang, J.; Son, J. S.; Panthani, M. G.; Shibata, T.; Chattopadhyay, S.; Talapin, D. V. Composition-Matched Molecular "Solders" for Semiconductors. *Science* **2015**, *347*, 425–428.

(59) Nag, A.; Kovalenko, M. V; Lee, J.-S.; Liu, W.; Spokoyny, B.; Talapin, D. V. Metal-Free Inorganic Ligands for Colloidal Nanocrystals: S2–, HS–, Se2–, HSe–, Te2–, HTe–, TeS32–, OH–, and NH2– as Surface Ligands. *J. Am. Chem. Soc.* **2011**, *133*, 10612–10620.

(60) Lee, E.; Park, S. J.; Cho, J. W.; Gwak, J.; Oh, M.-K.; Min, B. K. Nearly Carbon-Free Printable CIGS Thin Films for Solar Cell Applications. *Sol. Energy Mater. Sol. Cells* **2011**, *95*, 2928–2932.

(61) Cai, Y.; Ho, J. C. W.; Batabyal, S. K.; Liu, W.; Sun, Y.; Mhaisalkar, S. G.; Wong, L. H. Nanoparticle-Induced Grain Growth of Carbon-Free Solution-Processed CuIn(S,Se)$_2$ Solar Cell with 6% Efficiency. *ACS Appl. Mater. Inter.* **2013**, *5*, 1533–1537.

(62) Suehiro, S.; Horita, K.; Kumamoto, K.; Yuasa, M.; Tanaka, T.; Fujita, K.; Shimanoe, K.; Kida, T. Solution-Processed Cu$_2$ZnSnS$_4$ Nanocrystal Solar Cells: Efficient Stripping of Surface Insulating Layers Using Alkylating Agents. *J. Phys. Chem. C* **2013**, *118*, 804–810.

(63) Graeser, B. K.; Hages, C. J.; Yang, W. C.; Carter, N. J.; Miskin, C. K.; Stach, E. A.; Agrawal, R. Synthesis of (CuInS2)$_{0.5}$(ZnS)$_{0.5}$ Alloy Nanocrystals and Their Use for the Fabrication of Solar Cells via Selenization. *Chem. Mater.* **2014**, *26*, 4060–4063.

(64) Wu, W.; Cao, Y.; Caspar, J. V.; Guo, Q.; Johnson, L. K.; Malajovich, I.; Rosenfeld, H. D.; Choudhury, K. R. Studies of the Fine-Grain Sub-Layer in the Printed CZTSSe Photovoltaic Devices. *J. Mater. Chem. C* **2014**, *2*, 3777–3781.

(65) Kim, E. T.; Chung, W. J.; Lim, J.; Johe, P.; Glass, R. S.; Pyun, J.; Char, K. One-Pot Synthesis of PbS NP/sulfur-Oleylamine Copolymer Nanocomposites via the Copolymerization of Elemental Sulfur with Oleylamine. *Polym. Chem.* **2014**, *5*, 3617–3623.

(66) Katahara, J. K.; Hillhouse, H. W. Quasi-Fermi Level Splitting and Sub-Bandgap Absorptivity from Semiconductor Photoluminescence. *J. Appl. Phys.* **2014**, *116*, 173504.

(67) Xin, H.; Katahara, J. K.; Braly, I. L.; Hillhouse, H. W. 8% Efficient $Cu_2ZnSn(S,Se)_4$ Solar Cells from Redox Equilibrated Simple Precursors in DMSO. *Adv. Energy Mater.* **2014**, *4*, 1301823.

(68) He, J.; Sun, L.; Chen, S.; Chen, Y.; Yang, P.; Chu, J. Composition Dependence of Structure and Optical Properties of $Cu_2ZnSn(S,Se)_4$ Solid Solutions: An Experimental Study. *J. Alloys Compd.* **2012**, *511*, 129–132.

(69) Chen, S. Y.; Walsh, A.; Yang, J. H.; Gong, X. G.; Sun, L.; Yang, P. X.; Chu, J. H.; Wei, S. H. Compositional Dependence of Structural and Electronic Properties of $Cu_2ZnSn(S,Se)_4$ Alloys for Thin Film Solar Cells. *Phys. Rev. B* **2011**, *83*, 125201.

(70) Rey, G.; Redinger, a.; Sendler, J.; Weiss, T. P.; Thevenin, M.; Guennou, M.; El Adib, B.; Siebentritt, S. The Band Gap of Cu2ZnSnSe4: Effect of Order-Disorder. *Appl. Phys. Lett.* **2014**, *105*, 112106.

(71) Scragg, J. J. S.; Choubrac, L.; Lafond, A.; Ericson, T.; Platzer-Björkman, C. A Low-Temperature Order-Disorder Transition in Cu2ZnSnS4 Thin Films. *Appl. Phys. Lett.* **2014**, *104*, 041911.

(72) Cheng, a.-J.; Manno, M.; Khare, A.; Leighton, C.; Campbell, S. a.; Aydil, E. S. Imaging and Phase Identification of Cu_2ZnSnS_4 Thin Films Using Confocal Raman Spectroscopy. *J. Vac. Sci. Technol. A Vacuum, Surfaces, Film.* **2011**, *29*, 051203.

(73) Dimitrievska, M.; Fairbrother, A.; Fontané, X.; Jawhari, T.; Izquierdo-Roca, V.; Saucedo, E.; Pérez-Rodríguez, A. Multiwavelength Excitation Raman Scattering Study of Polycrystalline Kesterite Cu_2ZnSnS_4 Thin Films. *Appl. Phys. Lett.* **2014**, *104*, 021901.

(74) Khare, A.; Himmetoglu, B.; Johnson, M.; Norris, D. J.; Cococcioni, M.; Aydil, E. S. Calculation of the Lattice Dynamics and Raman Spectra of Copper Zinc Tin Chalcogenides and Comparison to Experiments. *J. Appl. Phys.* **2012**, *111*, 083707.

(75) Schwan, J.; Ulrich, S.; Batori, V.; Ehrhardt, H.; Silva, S. R. P. Raman Spectroscopy on Amorphous Carbon Films. *J. Appl. Phys.* **1996**, *80*, 440–447.

(76) Reich, S.; Thomsen, C. Raman Spectroscopy of Graphite. *Philos. Trans. R. Soc. A* **2004**, *362*, 2271–2288.

(77) Park, J.; Jang, Y. J.; Kim, Y. J.; Song, M.; Yoon, S.; Kim, D. H.; Kim, S.-J. Sulfur-Doped Graphene as a Potential Alternative Metal-Free Electrocatalyst and Pt-Catalyst Supporting Material for Oxygen Reduction Reaction. *Phys. Chem. Chem. Phys.* **2014**, *16*, 103–109.

(78) Ferrari, a.; Robertson, J. Interpretation of Raman Spectra of Disordered and Amorphous Carbon. *Phys. Rev. B* **2000**, *61*, 14095–14107.

(79) Chu, P. K.; Li, L. Characterization of Amorphous and Nanocrystalline Carbon Films. *Mater. Chem. Phys.* **2006**, *96*, 253–277.

(80) Collord, A. D.; Hillhouse, H. W. The Effect of Nanocrystal Reaction Time on $Cu_2ZnSn(S,Se)_4$ Solar Cells from Nanocrystal Inks. *Sol. Energy Mater. Sol. Cells* **2015**, *141*, 383–390.

(81) Collord, A. D.; Hillhouse, H. W. Composition Control and Formation Pathway of CZTS and CZTGS Nanocrystal Inks for Kesterite Solar Cells. *Chem. Mater.* **2015**, *27*, 1855–1862.

(82) Yang, W.; Miskin, C. K.; Carter, N. J.; Agrawal, R.; Stach, E. A. Compositional Inhomogeneity of Multinary Semiconductor Nanoparticles: A Case Study of Cu_2ZnSn_4. *Chem. Mater.* **2014**, *26*, 6955–6962.

(83) Hsu, W.; Zhou, H.; Luo, S.; Song, T.; Hsieh, Y.; Duan, H.; Ye, S.; Yang, W.; Hsu, C.; Jiang, C.; Bob, B.; Yang, Y. Spatial Element Distribution Control in a Fully Solution-Processed Nanocrystals-Based 8.6% $Cu_2ZnSn(S,Se)_4$ Device. *ACS Nano* **2014**, *8*, 9164–9172.

(84) Smith, J. S.; Bedrov, D.; Smith, G. D. A Molecular Dynamics Simulation Study of Nanoparticle Interactions in a Model Polymer-Nanoparticle Composite. *Compos. Sci. Technol.* **2003**, *63*, 1599–1605.

(85) Balazs, A. C.; Emrick, T.; Russell, T. P. Nanoparticle Polymer Composites: Where Two Small Worlds Meet. *Science* **2006**, *314*, 1107–1110.

(86) Gold, S.; Meli, L.; Green, P. F. Aggregation and Coarsening of Ligand- Poly(methyl Methacrylate) Thin Films. *ACS Nano* **2008**, *2*, 1305–1312.

(87) Shenhar, R.; Norsten, T. B.; Rotello, V. M. Polymer-Mediated Nanoparticle Assembly: Structural Control and Applications. *Adv. Mater.* **2005**, *17*, 657–669.

(88) Lin, Y.; Boker, A.; He, J. B.; Sill, K.; Xiang, H. Q.; Abetz, C.; Li, X. F.; Wang, J.; Emrick, T.; Long, S.; Wang, Q.; Balazs, A.; Russell, T. P. Self-Directed Self-Assembly of Nanoparticle/copolymer Mixtures. *Nature* **2005**, *434*, 55–59.

(89) Ingham, B.; Lim, T. H.; Dotzler, C. J.; Henning, A.; Toney, M. F.; Tilley, R. D. How Nanoparticles Coalesce: An in Situ Study of Au Nanoparticle Aggregation and Grain Growth. *Chem. Mater.* **2011**, *23*, 3312–3317.

(90) Simmonds, A. G.; Griebel, J. J.; Park, J.; Kim, K. R.; Chung, W. J.; Oleshko, V. P.; Kim, J.; Kim, E. T.; Glass, R. S.; Soles, C. L.; Sung, Y.-E.; Char, K.; Pyun, J. Inverse Vulcanization of Elemental Sulfur to Prepare Polymeric Electrode Materials for Li–S Batteries. *ACS Macro Lett.* **2014**, *3*, 229–232.

(91) Park, J.; Somogyi, A.; Theato, P.; Mackay, M. The Use of Elemental Sulfur as an Alternative Feedstock for Polymeric Materials. *Nat. Chem.* **2013**, *5*, 518–524.

(92) Rappold, T. a.; Lackner, K. S. Large Scale Disposal of Waste Sulfur: From Sulfide Fuels to Sulfate Sequestration. *Energy* **2010**, *35*, 1368–1380.

(93) Komarnisky, L.; Christopherson, R.; Basu, T. Sulfur: Its Clinical and Toxicologic Aspects. *Nutrition* **2003**, *9007*, 54–61.

(94) Chung, W. J.; Griebel, J. J.; Kim, E. T.; Yoon, H.; Simmonds, A. G.; Ji, H. J.; Dirlam, P. T.; Glass, R. S.; Wie, J. J.; Nguyen, N. A.; Guralnick, B. W.; Park, J.; Somogyi, Á.; Theato, P.; Mackay, M. E.; Sung, Y.-E.; Char, K.; Pyun, J. The Use of Elemental Sulfur as an Alternative Feedstock for Polymeric Materials. *Nat. Chem.* **2013**, *5*, 518–524.

(95) Chung, W. J.; Simmonds, A. G.; Griebel, J. J.; Kim, E. T.; Suh, H. S.; Shim, I.-B.; Glass, R. S.; Loy, D. a; Theato, P.; Sung, Y.-E.; Char, K.; Pyun, J. Elemental Sulfur as a Reactive Medium for Gold Nanoparticles and Nanocomposite Materials. *Angew. Chem. Int. Ed. Engl.* **2011**, *50*, 11409–11412.

(96) Griebel, J. J.; Namnabat, S.; Kim, E. T.; Himmelhuber, R.; Moronta, D. H.; Chung, W. J.; Simmonds, A. G.; Kim, K.-J.; van der Laan, J.; Nguyen, N. A.; Dereniak, E. L.; Mackay, M. E.; Char, K.; Glass, R. S.; Norwood, R. A.; Pyun, J. New Infrared Transmitting Material via Inverse Vulcanization of Elemental Sulfur to Prepare High Refractive Index Polymers. *Adv. Mater.* **2014**, *26*, 3014–3018.

(97) Zhuo, S.; Huang, Y.; Liu, C.; Wang, H.; Zhang, B. Sulfur Copolymer Nanowires with Enhanced Visible-Light Photoresponse. *Chem. Comm.* **2014**, *50*, 11208.

(98) Dirlam, P. T.; Simmonds, A. G.; Kleine, T. S.; Nguyen, N. a.; Anderson, L. E.; Klever, A. O.; Florian, A.; Costanzo, P. J.; Theato, P.; Mackay, M. E.; Glass, R. S.; Char, K.; Pyun, J. Inverse Vulcanization of Elemental Sulfur with 1,4-Diphenylbutadiyne for Cathode Materials in Li–S Batteries. *RSC Adv.* **2015**, *5*, 24718–24722.

(99) Dirlam, P. T.; Simmonds, A. G.; Shallcross, R. C.; Arrington, K. J.; Chung, W. J.; Griebel, J. J.; Hill, L. J.; Glass, R. S.; Char, K.; Pyun, J. Improving the Charge Conductance of Elemental Sulfur via Tandem Inverse Vulcanization and Electropolymerization. *ACS Macro Lett.* **2015**, *4*, 111–114.

(100) Martin, T. R.; Mazzio, K. A.; Hillhouse, H. W.; Luscombe, C. K. Sulfur Copolymer for the Direct Synthesis of Ligand-Free CdS Nanoparticles. *Chem. Comm.* **2015**, *51*, 11244–11247.

(101) Peng, Z. A.; Peng, X. Nearly Monodisperse and Shape-Controlled CdSe Nanocrystals via Alternative Routes: Nucleation and Growth. *J. Am. Chem. Soc.* **2002**, *124*, 3343–3353.

(102) Xiao, Q.; Xiao, C. Surface-Defect-States Photoluminescence in CdS Nanocrystals Prepared by One-Step Aqueous Synthesis Method. *Appl. Surf. Sci.* **2009**, *255*, 7111–7114.

(103) Zhang, J. Z. Interfacial Charge Carrier Dynamics of Colloidal Semiconductor Nanoparticles. *J. Phys. Chem. B* **2000**, *104*, 7239–7253.

(104) Joswig, J.-O.; Springborg, M.; Seifert, G. Structural and Electronic Properties of Cadmium Sulfide Clusters. *J. Phys. Chem. B* **2000**, *104*, 2617–2622.

(105) Alivisatos, A. P. Semiconductor Clusters, Nanocrystals, and Quantum Dots. *Science* **1996**, *271*, 933–937.

(106) Unni, C.; Philip, D.; Gopchandran, K. G. Studies on Optical Absorption and Photoluminescence of Thioglycerol-Stabilized CdS Quantum Dots. *Spectrochim. Acta. A. Mol. Biomol. Spectrosc.* **2008**, *71*, 1402–1407.

(107) Rincón, C.; Márquez, R. Defect Physics of the CuInSe2 Chalcopyrite Semiconductor. *J. Phys. Chem. Solids* **1999**, *60*, 1865–1873.

(108) Castro, S. L.; Bailey, S. G.; Raffaelle, R. P.; Banger, K. K.; Hepp, A. F. Synthesis and Characterization of Colloidal $CuInS_2$ Nanoparticles from a Molecular Single-Source Precursor. *J. Phys. Chem. A* **2007**, *108*, 12429–12435.

(109) Kim, Y.-K.; Ahn, S.-H.; Chung, K.; Cho, Y.-S.; Choi, C.-J. The Photoluminescence of CuInS2 Nanocrystals: Effect of Non-Stoichiometry and Surface Modification. *J. Mater. Chem.* **2012**, *22*, 1516.

(110) Guo, Q.; Kim, S. J.; Kar, M.; Shafarman, W. N.; Birkmire, R. W.; Stach, E. a.; Agrawal, R.; Hillhouse, H. W. Development of CuInSe 2 Nanocrystal and Nanoring Inks for Low-Cost Solar Cells. *Nano Lett.* **2008**, *8*, 2982–2987.

(111) Kar, M.; Agrawal, R.; Hillhouse, H. W. Formation Pathway of CuInSe2 Nanocrystals for Solar Cells. *J. Am. Chem. Soc.* **2011**, *133*, 17239–17247.

(112) Oikkonen, L. E.; Ganchenkova, M. G.; Seitsonen, a. P.; Nieminen, R. M. Effect of Sodium Incorporation into CuInSe2 from First Principles. *J. Appl. Phys.* **2013**, *114*, 1–6.

(113) Oikkonen, L. E.; Ganchenkova, M. G.; Seitsonen, a. P.; Nieminen, R. M. Mass Transport in CuInSe2 from First Principles. *J. Appl. Phys.* **2013**, *113*, 0–5.

(114) Alvarez-Garcia, J.; Barcones, B.; Perez-Rodriguez, A.; Romano-Rodriguez, A.; Morante, J. R.; Janotti, A.; Wei, S. H.; Scheer, R. Vibrational and Crystalline Properties of Polymorphic CuInC 2 (C=Se,S) Chalcogenides. *Phys. Rev. B - Condens. Matter Mater. Phys.* **2005**, *71*, 1–9.

(115) Rincon, C.; Ramirez, F. J. Lattice Vibrations of CuInSe2 and CuGaSe2 by Raman Microspectrometry. *J. Appl. Phys.* **1992**, *72*, 4321–4324.

(116) Minceva-Sukarova, B.; Najdoski, M.; Grozdanov, I.; Chunnilall, C. J. Raman Spectra of Thin Solid Films of Some Metal Sulfides. *J. Mol. Struct.* **1997**, *410-411*, 267–270.

(117) Tanaka, T.; Sueishi, T.; Saito, K.; Guo, Q.; Nishio, M.; Yu, K. M.; Walukiewicz, W. Existence and Removal of Cu2Se Second Phase in Coevaporated Cu2ZnSnSe4 Thin Films. *J. Appl. Phys.* **2012**, *111*, 53522–53524.

(118) Weszka, J.; Daniel, P.; Burian, a.; Burian, a. M.; Nguyen, a. T. Raman Scattering in In2Se3 and InSe2 Amorphous Films. *J. Non. Cryst. Solids* **2000**, *265*, 98–104.

(119) Izadneshan, H.; Gremenok, V. F. Micro Structural Analysis of In2S3 Thin Films by Raman Spectroscopy. *J. Appl. Spectrosc.* **2014**, *81*, 765–770.

(120) Thomson, J. W.; Wang, X.; Hoch, L.; Faulkner, D.; Petrov, S.; Ozin, G. a. Discovery and Evaluation of a Single Source Selenium Sulfide Precursor for the Synthesis of Alloy PbSxSe1−x Nanocrystals. *J. Mater. Chem.* **2012**, *22*, 5984.

(121) Patakfalvi, R.; Papp, S.; Dékány, I. The Kinetics of Homogeneous Nucleation of Silver Nanoparticles Stabilized by Polymers. *J. Nanoparticle Res.* **2007**, *9*, 353–364.

(122) Di Luccio, T.; Laera, A. M.; Tapfer, L.; Kempter, S.; Kraus, R.; Nickel, B. Controlled Nucleation and Growth of CdS Nanoparticles in a Polymer Matrix. *J. Phys. Chem. B* **2006**, *110*, 12603–12609.

(123) Antolini, F.; Pentimalli, M.; Di Luccio, T.; Terzi, R.; Schioppa, M.; Re, M.; Mirenghi, L.; Tapfer, L. Structural Characterization of CdS Nanoparticles Grown in Polystyrene Matrix by Thermolytic Synthesis. *Mater. Lett.* **2005**, *59*, 3181–3187.

(124) Uhl, A. R.; Katahara, J. K.; Hillhouse, H. W. Molecular-Ink Route to 13.0% Efficient Low-Bandgap CuIn(S,Se) 2 and 14.7% Efficient Cu(In,Ga)(S,Se) 2 Solar Cells. *Energy Environ. Sci.* **2016**, *9*, 130–134.

(125) Collord, a. D.; Hillhouse, H. W. Germanium Alloyed Kesterite Solar Cells with Low Voltage Deficits. *Chem. Mater.* **2016**, *28*, 2067–2073.

(126) Chen, S.; Walsh, A.; Gong, X. G.; Wei, S. H. Classification of Lattice Defects in the Kesterite Cu2ZnSnS4 and Cu2ZnSnSe4 Earth-Abundant Solar Cell Absorbers. *Adv. Mater.* **2013**, *25*, 1522–1539.

(127) Nguyen, T. B.; Ermolenko, L.; Al-Mourabit, A. Efficient and Selective Multicomponent Oxidative Coupling of Two Different Aliphatic Primary Amines into Thioamides by Elemental Sulfur. *Org. Lett.* **2012**, *14*, 4274–4277.

(128) Hohl, D.; Jones, R. O. First-Prinsibles Molecular-Dynamics Simulation of Liquid and Amorphous Selenium. *Phys. Rev. B* **1991**, *43*, 3856.

(129) Miyamoto, Y. Structure and Phase Transformation of Rhombohedral Selenium Composed of Se 6 Molecules. *Jpn. J. Appl. Phys.* **1980**, *19*, 1813–1819.

(130) Nelson, J.; Emmott, C. J. M.; A, P. T. R. S.; Nelson, J.; Emmott, C. J. M. Can Solar Power Deliver? *Philos. Trans. R. Soc. A* **2013**, *371*.

(131) Lee, M. M.; Teuscher, J.; Miyasaka, T.; Murakami, T. N.; Snaith, H. J. Efficient Hybrid Solar Cells Based on Meso-Superstructured Organometal Halide Perovskites. *Science* **2012**, *338*, 643–647.

(132) Han, Y.; Meyer, S.; Dkhissi, Y.; Weber, K.; Pringle, J. M.; Bach, U.; Spiccia, L.; Cheng, Y.-B. Degradation Observations of Encapsulated Planar CH3NH3PbI3 Perovskite Solar Cells at High Temperatures and Humidity. *J. Mater. Chem. A* **2015**, *3*, 8139–8147.

(133) Mazzio, K. a.; Luscombe, C. K. The Future of Organic Photovoltaics. *Chem. Soc. Rev.* **2014**, *44*, 78–90.

(134) Hibberd, C. J.; Chassaing, E.; Liu, W.; Mitzi, D. B.; Lincot, D.; Tiwari, A. N. Non-Vacuum Methods for Formation of Cu(In, Ga)(Se, S)2 Thin Film Photovoltaic Absorbers. *Prog. Photovoltaics Res. Appl.* **2010**, *18*, 434–452.

(135) Ford, G. M.; Guo, Q.; Agrawal, R.; Hillhouse, H. W. CuIn(S,Se)2thin Film Solar Cells from Nanocrystal Inks: Effect of Nanocrystal Precursors. *Thin Solid Films* **2011**, *520*, 523–528.

(136) Connor, S. T.; Hsu, C.; Weil, B. D.; Aloni, S. Phase Transformation of Biphasic Cu 2 S - CuInS 2 to Monophasic CuInS 2 Nanorods. **2009**, *131*, 4962–4966.

(137) Search, H.; Journals, C.; Contact, A.; Iopscience, M.; Address, I. P.; Venables, J. a; Spiller, G. D. T.; Hanbucken, M. Nucleation and Growth of Thin Films. *Reports Prog. Phys.* **1984**, *47*, 399–459.

(138) Kolny-Olesiak, J.; Weller, H. Synthesis and Application of Colloidal CuInS2 Semiconductor Nanocrystals. *ACS Appl. Mater. Inter.* **2013**, *5*, 12221–12237.

(139) Li, L.; Pandey, A.; Werder, D. J.; Khanal, B. P.; Pietryga, J. M.; Klimov, V. I. Efficient Synthesis of Highly Luminescent Copper Indium Sulfide-Based Core/shell Nanocrystals with Surprisingly Long-Lived Emission. *J. Am. Chem. Soc.* **2011**, *133*, 1176–1179.

(140) Zhang, Y.; Griebel, J. J.; Dirlam, P. T.; Nguyen, N. a.; Glass, R. S.; Mackay, M. E.; Char, K.; Pyun, J. Inverse Vulcanization of Elemental Sulfur and Styrene for Polymeric Cathodes in Li-S Batteries. *J. Polym. Sci. Part A Polym. Chem.* **2017**, *55*, 107–116.

(141) Martin, T. R.; Mazzio, K. A.; Hillhouse, H. W.; Luscombe, C. K. Synthesis of Ligand-Free CdS Nanoparticles within a Sulfur Copolymer Matrix. *J. Vis. Exp.* **2016**, *111*, e54047.

(142) Rühle, S. Tabulated Values of the Shockley-Queisser Limit for Single Junction Solar Cells. *Sol. Energy* **2016**, *130*, 139–147.

Appendix A: List of Publications

- Martin, T. R.; Hillhouse, H. W.; Luscombe, C. K. "Chalcogen Polymers for Low-Temperature CISSe Nanoparticle Formation” *in preparation*, 2017

- Martin, T. R.; Hillhouse, H. W.; Luscombe, C. K. "Selenium Polymer for Fully Printed Metal-Selenide Thin-Films” *in preparation*, 2017

- Clark, J. A.; Uhl, A. R.; Martin, T. R.; Hillhouse, H. W. “Extrinsic Impurity Transport in Solution-Processed Cu2ZnSn(S,Se)4” under review, *Chem. Mater.*, 2017

- Martin, T. R.; Katahara, J. K.; Bucherl, C. N.; Krueger, B. W.; Hillhouse, H. W.; Luscombe, C. K. "Nanoparticle ligands and pyrolized graphitic carbon in CZTSSe photovoltaic devices" *Chem. Mater.*, 2016, 28, 135.

- Martin, T. R.; Mazzio, K. A.; Hillhouse, H. W.; Luscombe, C. K. "Synthesis of ligand-free CdS nanoparticles within a sulfur copolymer matrix" *J. Vis. Exp.*, 2015. Invited paper.

- Martin, T. R.; Mazzio, K. A.; Hillhouse, H. W.; Luscombe, C. K. "Sulfur copolymer for the direct synthesis of ligand-free CdS nanoparticles" *Chem. Commun.*, 2015, 51, 11244.

- Yang, P.; Zeigler, D. F.; Bryant, K. C.; Martin, T. R. Gamelin, D. R.; Luscombe, C. K. "Identifying Effects of TiO2 Nanowires inside Bulk Heterojunction Organic Photovoltaics on Charge Diffusion and Recombination" *J. Mater. Chem. C.*, 2014, 2, 4922.

- Zeigler, D. F.; Candelaria, S. L.; Mazzio, K. A.; Martin, T. R.; Uchaker, E.; Suraru, S.-L.; Kang, L. J.; Cao, G.; Luscombe, C. K. "N-type hyperbranched polymers for supercapacitor cathodes with variable porosity and excellent electrochemical stability" *Macromolecules*, 2015, 48, 5196.

Appendix B: Intellectual Property

- International (PCT) Patent Application No. PCT/US2017/037062 filed 6/12/2017; Entitled: "CHALCOGEN COPOLYMERS"; Inventors: Hugh Hillhouse, Ian Braly, Christine Luscombe, Trevor Martin

- U.S. Provisional Patent Application No. 62/348,713 filed 6/10/2016 Entitled: "CHALCOGEN COPOLYMERS" Inventors: Hugh Hillhouse, Christine Luscombe, Trevor Martin, Ian Braly

- Provisional Patent Application No. 62/180,165 filed 6/16/2015; Entitled: "METHODS OF MAKING SUBSTANTIALLY LIGAND-FREE NANOPARTICLES AND RELATED NANOPARTICLES AND NANOPARTICLE DEVICES"; Inventors: Hugh Hillhouse, Christine Luscombe, and Trevor Martin

Appendix C: Copyright Permission

Chapter 2 is adapted with permission from (Martin, T. R.; Katahara, J. K.; Bucherl, C. N.; Krueger, B. W.; Hillhouse, H. W.; Luscombe, C. K. "Nanoparticle ligands and pyrolized graphitic carbon in CZTSSe photovoltaic devices" *Chem. Mater.*, 2016, 28, 135.) Copyright (2016) American Chemical Society

Chapter 3 is adapted with permission from (Martin, T. R.; Mazzio, K. A.; Hillhouse, H. W.; Luscombe, C. K. "Sulfur copolymer for the direct synthesis of ligand-free CdS nanoparticles" *Chem. Commun.*, 2015, 51, 11244.) Copyright (2015) The Royal Society of Chemistry